Beam Dynamics Investigations for the Second Injection Beamline of MESA

Dissertation submitted for the award of the title
"Doctor of Natural Sciences"

to the Faculty of Physics, Mathematics, and Computer Science
of the Johannes Gutenberg-University Mainz

Anatolii Kalamaiko
born in Svatovo, Ukraine

Mainz, February 12, 2026

JOHANNES GUTENBERG
UNIVERSITÄT MAINZ

Date of the doctoral examination: 21 January 2026

Abstract

The project MESA (Mainz Energy-Recovering Superconducting Accelerator) is an unique electron accelerator placed at the Johannes Gutenberg University in Mainz, Germany [5]. MESA will be a recirculating machine that achieves energy recovery in superconducting accelerating structures through multiple turns. The goal of the MESA project is to conduct experiments in many fields, such as particle physics, nuclear physics and other fundamental research [17].

The accelerator has two different laser-driven electron sources (polarized and unpolarized) operating at 100 kV. The main polarized source STEAM (Small Thermalized Electron-source at Mainz)[3] allows to produce spin-polarized electron beam and has been operating since the end of 2023. A second source MIST (MESA Injector Source Two) [4] is planned for construction in the future.

The peculiarity of the second source is that it was designed to produce electron beam with a high charge in the bunch. In future, this source and double Mott polarimeter will be arranged on the same height above the MESA main injector beamline. Therefore, a special parallel shifting beamline is required to transport a highly charged electron beam from the source MIST to the main MESA beamline.

This work is dedicated to the design of such a transport channel. Simulations shown that the designed channel allow to compress and transport electron beam to the first acceleration section of MESA with up to 10 mA of average current, which corresponds to charge of 7.7 pC in a bunch for an operating frequency 1.3 GHz.

Zusammenfassung

Das Projekt MESA (Mainz Energy-Recovering Superconducting Accelerator) ist ein einzigartiger Elektronenbeschleuniger, der an der Johannes Gutenberg-Universität in Mainz, Deutschland, errichtet wird [5]. MESA wird eine rezirkulierende Anlage sein, die durch mehrfache Umläufe in supraleitenden Beschleunigungsstrukturen eine Energierückgewinnung ermöglicht. Das Ziel des MESA-Projekts ist es, Experimente in Teilchenphysik, Kernphysik und anderer Grundlagenforschung durchzuführen [17].

Der Beschleuniger verfügt über zwei verschiedene lasergetriebene Elektronenquellen (polarisiert und unpolarisiert), die bei 100 kV betrieben werden. Die Hauptquelle für den spinpolarisierten Elektronenstrahl, STEAM (Spin-polarized Electron Accelerating Machine) [3], ermöglicht die Erzeugung eines spinpolarisierten Elektronenstrahls und ist seit Ende 2023 in Betrieb. Eine zweite Quelle, MIST (MESA Injector Source Two) [4], ist geplant.

Die Besonderheit der zweiten Quelle besteht darin, dass sie darauf ausgelegt ist, einen Elektronenstrahl mit einer sehr hohen Ladung pro Bunch zu erzeugen. Zukünftig werden diese Quelle und ein doppelter Mott-Polarimeter in derselben Höhe über der Hauptinjektorstrahlführung von MESA angeordnet. Daher wird eine spezielle, parallel verlaufende Strahlführung benötigt, um den Transport des hochgeladenen Strahls von der Quelle MIST zur Hauptinjektorstrahlführung von MESA zu erleichtern.

Contents

Chapter 1

Motivation

1.1 Introduction

The Standard Model provides a comprehensive framework for describing fundamental particles and their interactions via electromagnetic, weak, and strong forces. It has successfully explained a vast array of experimental observations, establishing itself as a cornerstone of modern particle physics. The model has led to groundbreaking discoveries, such as the Higgs boson, offering profound insights into the universe's structure. However, despite its successes, several fundamental questions remain unanswered, including the nature of dark matter and the unification of fundamental forces. These open challenges present exciting opportunities for discoveries beyond the current theoretical framework.

Beyond refining the Standard Model, particle accelerators are essential for probing unresolved mysteries in physics. One of the most significant challenges in contemporary science is understanding dark matter—an invisible and elusive form of matter thought to make up approximately 85% of the universe's total mass. Despite its assumed abundance, dark matter does not interact with electromagnetic forces, making it undetectable through conventional observational methods. Investigating the nature of dark matter remains one of the most compelling challenges in modern physics [20].

At the Institute for Nuclear Physics at Johannes Gutenberg University Mainz, a new multi-turn energy recovery linac called the Mainz Energy-recovering Superconducting Accelerator (MESA) is being built [2].

The concept of energy-recovering accelerators (ERLs) was introduced in 1965 [42]. ERL accelerators combine the advantages of storage rings and linear accelerators, which makes it possible to obtain low-emittance beams with a bunch length in the femtosecond range, while providing high beam power.

In a ring the long storage times lead to an equilibrium beam emittance which is much larger than that in a linear accelerator in which the emittance is dominated by the relatively low temperature of the source (See Equation (2.59)). The latter therefore offers far superior beam quality if the device is to be used as a light source. On the other hand, in operation as a high energy collider like the LHeC , the single passage of electrons allows much tighter focusing (and therefore higher luminosity) since a much larger beam/beam effect can be tolerated compared to a ring/ring collider [7] [47].

Figure 1.1 shows the general scheme of the MESA accelerator, illustrating its main components and experimental stations.

The accelerator MESA has two different laser-driven electron sources (polarized and unpolarized).

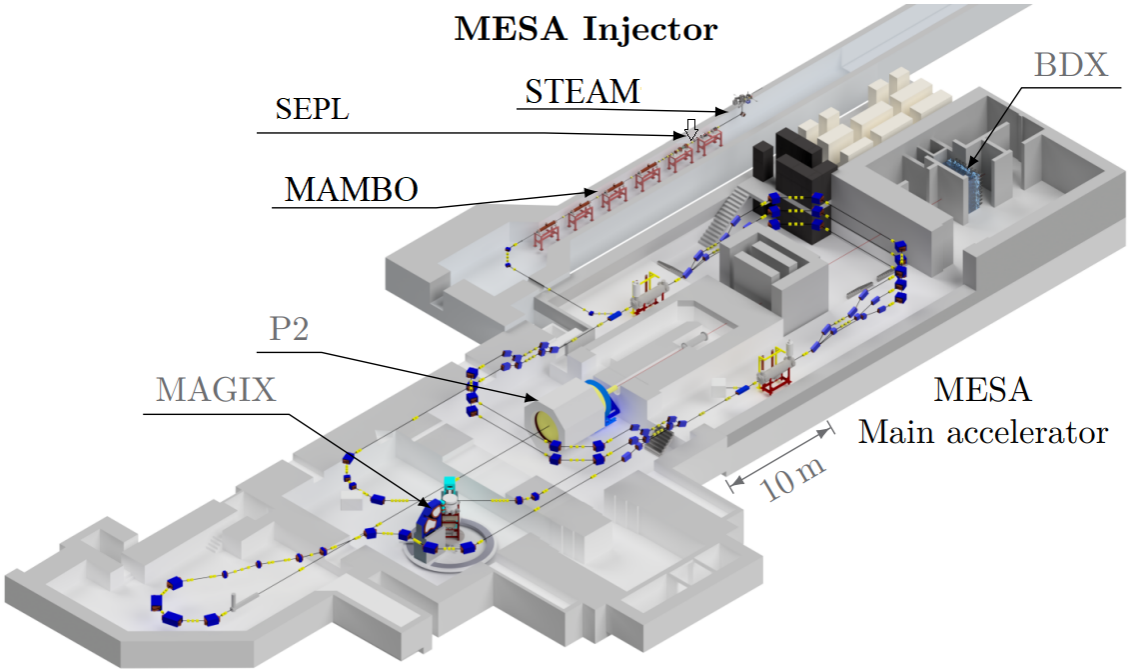

Figure 1.1: The general layout of the MESA project and the main components of the facility. P2 and MAGIX - two key experiments to explore fundamental questions in physics. In this figure, the electron beam travels from right to left.

The first important operation mode of MESA is using a spin-polarized electron beam produced by the existing source STEAM, which has been operating since the end of 2023. STEAM (Small Thermalized Electron-source At Mainz) is operated at a rather low potential of 100 kV in order to maximize operational safety due to very sensitive NEA-photocathodes used for the generation of a spin-polarized electron beam [3].

In the case of the second MESA source (see Figure 1.3), called MESA Injector Source Two (MIST), these restrictions do not apply. However, at the first stage the source will be operated with a 100 keV beam too. The second source MIST is planned for construction in the future. The feature of the second source is that it was designed to produce an electron beam with a very high charge per bunch. Source MIST will allow the generation of electron bunches with a repetition rate of 1.3 GHz and an average current of 1 mA at the first stage (0.77 pC per bunch), with plans to increase the current up to 10 mA at the second stage (7.7 pC per bunch) [9].

In the future, this source and a double Mott polarimeter will be arranged above the MESA main injector beamline. Therefore, a special parallel shifting beamline is required to transport the highly charged beam from the source MIST to the main MESA beamline.

P2 and MAGIX are two important experiments planned to be carried out at the MESA accelerator. Both experiments are aimed at studying fundamental questions in physics. The generation of high beam current is essential for these experiments.

A high beam current allows for a greater number of particle interactions per unit time, which significantly improves the statistical accuracy of the measurements. This is especially important for experiments aimed at measuring rare processes or small asymmetries, such as the P2 experiment, which focuses on measuring the weak charge of a proton. Therefore, it is very important to design an injection system that provides

maximum current in a single bunch.

It is also worth mentioning that if necessary, the operating potential of the MIST source can be increased to 200 kV or even 300 kV [8]. Such an upgrade will require replacing the initial accelerating sections of the Milliampere Booster (MAMBO) and updating some focusing elements in the injection channel.

MAMBO is the injector linac used to accelerate electron beam from electron sources STEAM and MIST from 100 keV to an energy of 5 MeV. The CAD model of the MAMBO structure is shown in Figure 1.2. MAMBO comprises four normal-conducting radiofrequency cavities, each approximately 2 meters in length. These cavities have a bi-periodic $\frac{\pi}{2}$ structure. The first cavity featuring a graded beta profile and the subsequent three maintaining a constant beta.

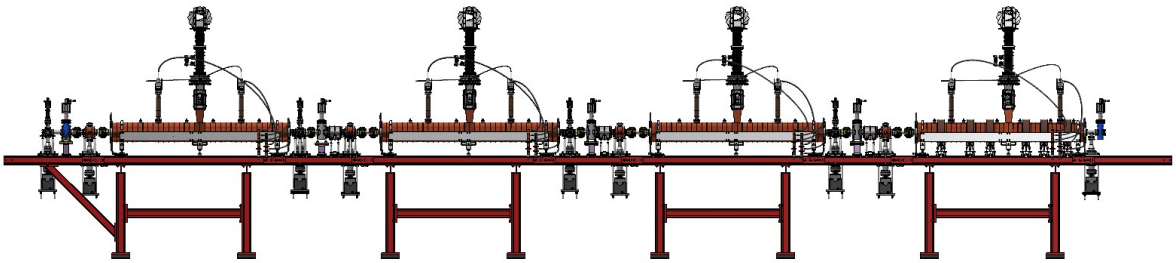

Figure 1.2: General layout of the Milliampere Booster (MAMBO) — the normal-conducting injector linac for the accelerator MESA.

However, such an upgrade will significantly increase the average beam current in the accelerator due to the much smaller influence of space charge effects on particles in the beam. It is worth noting that in the case of such an upgrade, it will be difficult to use the STEAM source due to the limitation of the maximum operating potential for such types of sources, as indicated above.

The aim of this work is to develop a special separation beamline that will provide transport and compression of electron bunches from the electron source MIST to the first accelerating section of MAMBO.

1.2 Motivation

As mentioned earlier, the goal of the MESA project is to conduct important experiments in particle and nuclear physics that require high accelerator current. This means that it is important for future experiments to choose the right lattice of the injection system that will be able to provide high charge in the bunch.

The electron source MIST is more suitable for producing highly charged bunches than the STEAM source because it does not need to generate spin-polarized beams; this eliminates the need for the bulky spin rotation system required for STEAM.

Moreover, compared to STEAM, the MIST source does not require a special chopper system, since the strict longitudinal acceptance limitation imposed by the chopper is only required for experiments with spin-polarized beams.

Thus, the goal of this work is the design of the additional injection system that will provide transport and compression of 100 keV electron bunches to the first accelerator section of MAMBO with a maximum bunch charge of up to 7.7 pC.

The general layout of the MEsa Low-energy Beam Apparatus (MELBA) beamline and the positions of both electron sources are shown in Figure 1.3.

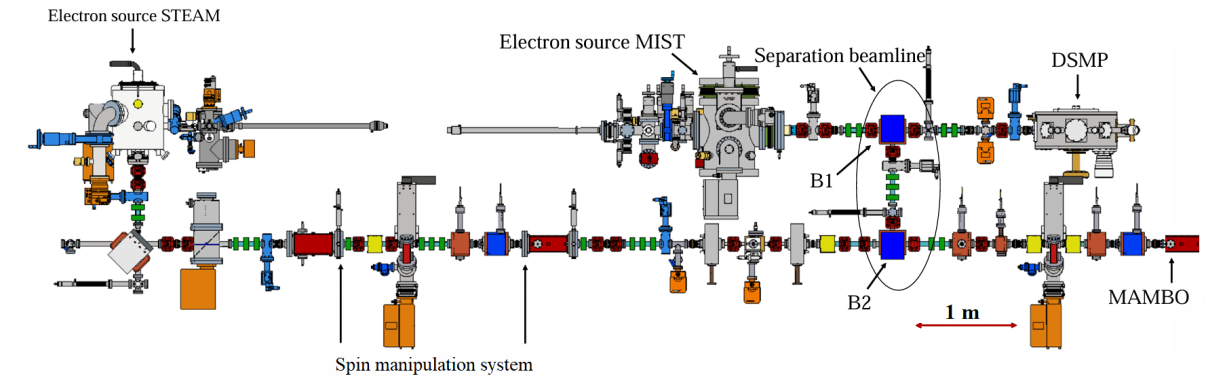

Figure 1.3: The general layout of the MELBA beamline and the positions of both electron sources. The electron beam propagates from left to right. B1 and B2 are bending magnets, while DSMP houses the Double Scattering Mott Polarimeter.

Moreover, this separation beamline must provide beam transportation in two different directions:

- Transport of the produced electron beam from the electron source STEAM to the Double Scattering Mott Polarimeter (DSMP)[48], [49]. This operation mode is required to measure the spin polarization of the electron beam using DSMP before conducting experiments with spin-polarized beams.
- Transport of the electron beam from the electron source MIST to the first acceleration section of MAMBO [51]. This operation mode allows transporting highly charged beams to the accelerator for conducting experiments requiring high-intensity beams.

1.3 MESA overview

The idea to build an ERL was first mentioned in [42] and allows one to bypass the RF amplifier power limit in c.w. operation to reach high beam currents, respectively beam powers [51].

The beam power P can be determined by the following formula:

$$P = I \cdot E,$$

where I is the beam current in amperes (A), and E is the kinetic energy per particle is given in electronvolts (eV), the conversion factor is:

$$1\,\mathrm{eV} = 1.602 \times 10^{-19}\,\mathrm{J}.$$

In a conventional linear accelerator, the entire beam energy is lost after passing the target region, resulting in high energy consumption. In contrast, an Energy Recovery Linac (ERL) significantly reduces the required input power by recovering most of the beam energy. Specifically, the power demand in an ERL is reduced approximately by the ratio of the injected beam energy E_{in} to the maximum beam energy E_{max}:

$$\text{Power reduction factor} = \frac{E_{\mathrm{in}}}{E_{\mathrm{max}}}$$

For the MESA accelerator, this ratio is approximately 1/20, meaning the energy consumption can be reduced by a factor of about 20 compared to a non-energy-recovering system.

The additional effort in building ERLs, of course, only pays off if the beam power is large enough — otherwise, a conventional linac like MAMI will suffice. This means that the beam power should exceed 100 kW. At MESA, this will become possible with the second electron source, MIST, delivering 7.7 pC per bunch, this corresponds to 1 MW at 100 MeV and 1.3 GHz.

An energy recovery linac (ERL) is a new type of electron accelerator used for generating an electron beam of high average current and small emittance. MESA is a recirculating machine that achieves energy recovery in superconducting accelerating structures through multiple turns. Electrons produced by a photo-source are accelerated with a radio frequency (RF) field in specially designed superconducting cavities, which are used to minimize ohmic power losses and provide the opportunity for operation in ERL mode. In this mode, the earlier accelerated beam is decelerated, transferring its energy back to the RF field in the superconducting chamber [31].

Cornell University's CBETA [52] and TU Darmstadt's S-DALINAC [52] have successfully demonstrated multi-turn Energy Recovery Linac (ERL) operations. CBETA achieved four accelerating and four decelerating passes using superconducting RF cavities and Fixed-Field Alternating Gradient (FFAG) magnets, marking it as the first multi-turn SRF ERL to recover energy in this manner. Similarly, S-DALINAC achieved high-transmission multi-turn energy recovery in August 2021, validating the feasibility of such operations in superconducting linear accelerators [47].

So far, TU Darmstadt has achieved the highest power in a multi-turn SRF ERL—with only a few hundred watts. However, with the second electron source MIST, it would be possible to achieve beam powers of up to approximately 1 MW for a 7.7 pC bunch charge.

This would represent the next step in the research and development of such machines. Figure 1.4 shows the electron energy and current for different ERLs [53].

The MESA project is poised to advance this technology further. Designed to operate with beam currents up to 10 mA at 105 MeV, MESA aims to achieve beam powers approaching 1 MW, significantly surpassing the capabilities of existing ERLs . This positions MESA as a critical stepping stone toward large-scale projects like the proposed Large Hadron Electron Collider (LHeC), where high-current, multi-turn ERLs are essential for achieving the desired luminosities .

In ERL mode, once electrons have been accelerated and utilized for experimental purposes, the same beam is directed back through the cavities to be decelerated [18],

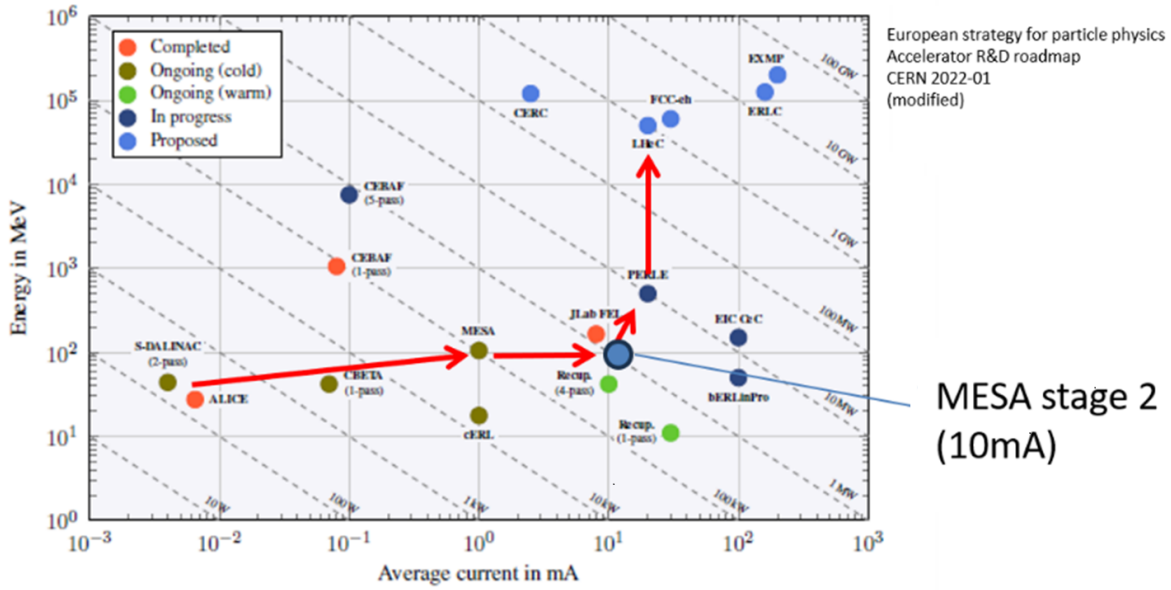

Figure 1.4: Electron energy E vs. electron source current I for classes of past, present, and possible future ERL facilities as introduced in the text. Dashed diagonal lines represent constant power, P [kW] = E [MeV] $\cdot$ I [mA].

[41]. During this process, the energy of the electron beam is transferred back into the RF field within the cavities. This approach not only conserves energy but also effectively bypasses the power limitations of RF amplifiers in continuous wave operation, allowing the accelerator to achieve higher beam currents and power levels.

The concept of an ERL, first proposed in early studies [18], provides an innovative solution to overcoming the inherent power constraints of traditional accelerators. By recovering and reusing energy from the beam, MESA can significantly increase the flux of projectiles available for scattering experiments, improving data quality without requiring substantial investments in additional RF power. This capability makes MESA particularly attractive for precision experiments that demand high statistics, as it can deliver a continuous and high-intensity beam.

MESA is initially designed to operate with a beam current of up to 1 mA, with a planned upgrade to handle beam currents up to 10 mA [8] at a nominal energy of 105 MeV in ERL mode. Such high beam currents are essential for enhancing the sensitivity and accuracy of experimental measurements, particularly in research fields reliant on detailed statistical analysis.

In this context, it is useful to introduce the term *luminosity*, defined as the product of the beam current (in electrons per second), the density of the target (in atoms/cm^3), and the target thickness (in cm):

$$\mathcal{L} = \frac{I}{e} \cdot n \cdot d \tag{1.1}$$

where $\mathcal{L}$ is the luminosity, I is the beam current, e is elementary charge, n is the target density, and d is the target thickness. A higher beam current allows reducing either the density or thickness of the target while maintaining the same luminosity. Further details can be found in Section 1.4.

The energy of the emitted electrons is relatively low, typically around 0.2 eV, as emitted from the CsKSb cathode of the electron source MIST. This is characteristic of

electrons generated directly from a photocathode and subsequently accelerated by an accelerating voltage of up to 100 keV [54].

After their generation, electrons are injected into the MESA system through the injector system (see Figure 1.4). At this stage, the MAMBO section provides the first significant acceleration within normal conducting cavities, increasing the electron beam energy from 100 keV to approximately 5 MeV.

The final energy of the electrons in the MESA project can reach a nominal value of 105 MeV or 155 MeV, depending on the number of turns. Each turn increases the electron beam energy by approximately 50 MeV.

After its initial use, the electron beam is recirculated and directed back into the acceleration cavities for deceleration. During deceleration, the kinetic energy of the electrons is transferred back into the RF field of the cavities, effectively recovering and reusing energy.

1.4 Physics challenges

Particle accelerators allow one to research a wide range of scientific problems, such as the search for dark matter or tests of the Standard Model. The activities of the Institute of Nuclear Physics at Johannes Gutenberg University are focused on these topics.

The Institute of Nuclear Physics at Johannes Gutenberg University is at the forefront of addressing some of the most fundamental and complex questions in modern physics. Its primary research efforts focus on the search for dark matter and high-precision testing of the Standard Model. Both areas require sophisticated experimental setups, particularly those involving low momentum transfer, where even minor deviations from theoretical predictions could indicate new physics.

Research on dark matter remains another priority for the institute [55]. Although dark matter is believed to account for the majority of the universe's mass, it has yet to be directly detected. Scientists employ state-of-the-art techniques to identify and analyze weak interaction signals that may suggest the presence of dark matter particles. These investigations rely on advanced detection systems and intricate data analysis, with low momentum transfer experiments playing a crucial role in detecting rare or weak interactions that may provide insights into the properties of dark matter.

The institute is also strongly committed to high-precision testing of the Standard Model, which, despite its successes, still contains unresolved gaps. Researchers conduct rigorous experiments to test the model's predictions, particularly in the realm of fundamental interactions at low momentum transfer. This approach enables an in-depth study of the weak force and other interactions, potentially revealing deviations from expected outcomes. Any such deviations could indicate the presence of new particles or forces, leading to groundbreaking discoveries in physics [17].

The ERL-process not only conserves power but also allows MESA to achieve higher beam currents, making it a highly efficient system for conducting precision experiments. After reaching the final energy, electrons are directed towards the experimental stations, such as MAGIX and P2 [17, 20].

1.5 MAGIX

The MAGIX (MESA Gas Internal Target Experiment) is a key component of the MESA project, designed to perform precise and versatile measurements using a gas-jet target and high-intensity electron beams [17].

The experimental setup consists of two identical magnetic spectrometers that detect scattered or produced particles. These spectrometers can rotate around the target center, allowing for flexible measurement configurations [21].

Thanks to their well-understood magneto-optical properties, the spectrometers enable accurate reconstruction of interaction points based on detected impact positions and angles in the focal plane, while high-resolution gas detectors ensure precise particle tracking and measurement [5].

The MESA accelerator operates in energy-recovery linac (ERL) mode, where decelerated beams transfer their kinetic energy back to the RF system. This approach enables experiments at peak energy using thin targets, achieving high luminosities [22]. Moreover, Dr. Ben LeDroit, in his PhD work, has shown that Coulomb scattering at MAGIX is very strong. His simulations indicate that the expected beam losses will limit the achievable luminosity to approximately 10^{35} $\mathrm{cm}^{-2}\,\mathrm{s}^{-1}$ [56], this is, however, still by far sufficient to conduct hitherto impossible experiments.

Thus, the MAGIX experiment, together with the advanced technologies of the MESA accelerator, offers unique opportunities for high-precision research in nuclear and particle physics (see Fig. 1.5).

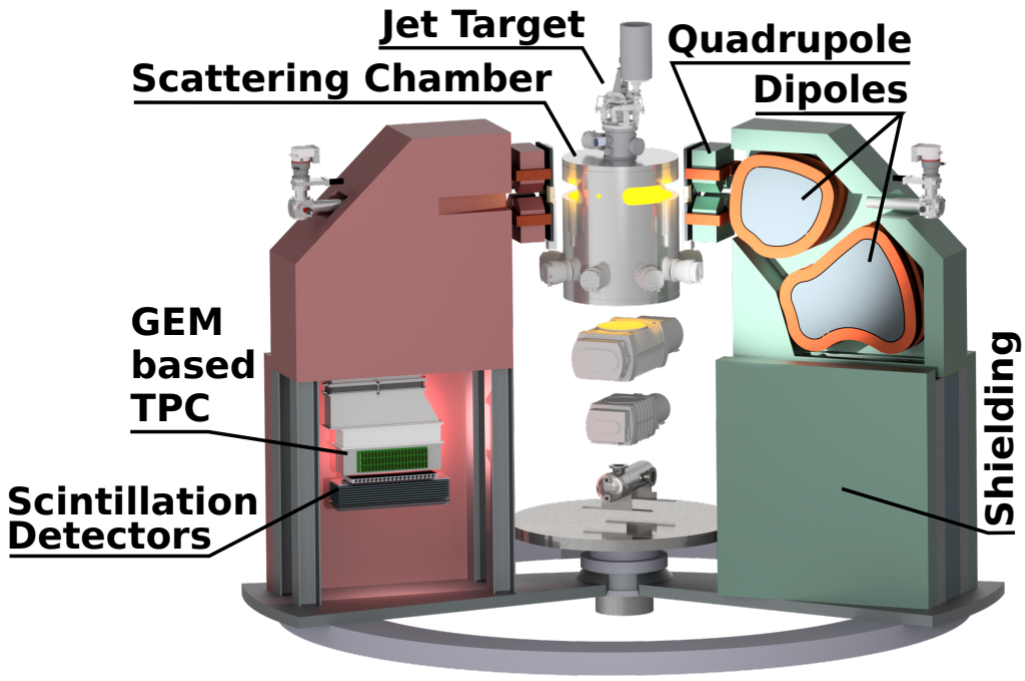

Figure 1.5: Scheme of the MAGIX spectrometer [17].

The electron beam interacts with the MAGIX gas-jet target inside the scattering chamber, which is directly connected to the beam pipe without any windows. The MAGIX setup is designed to operate with various gases—such as hydrogen, helium, oxy-

gen, argon, and xenon—for fundamental physics experiments. This configuration enables a broad range of high-precision studies at MESA energy levels, including:

- Measurement of the proton radius using a hydrogen target to address the proton radius puzzle [66].
- Few-body physics experiments with a helium target.
- Determination of the astrophysical S-factor in inverse solar fusion reactions, crucial for astrophysical studies.
- Searches for dark photons through interactions with heavy nuclear targets like argon and xenon.

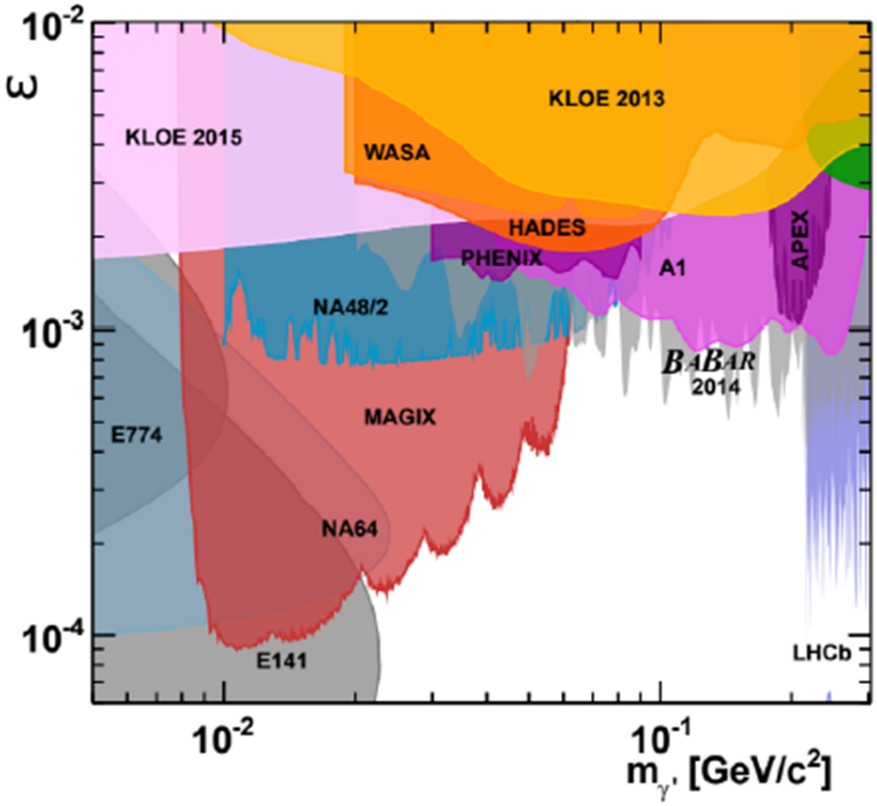

Figure 1.6: The MAGIX sensitivity range for the visibly decaying dark photon using MESA beam energies up to 105 MeV. [17].

A high beam current is important for some experiments the MAGIX project because it increases the luminosity—the rate of interactions between the electron beam and the target (see Equation (1.1)). This enabling the observation of more scattering events and yielding more reliable data.

To achieve this, it is important to develop a beamline that allows to transport the high charged beam from the MIST electron source to the first acceleration section of MAMBO. Thus, the separation beamline developed within this work is an import ingredient for the realization of beam currents in excess of 1 mA at MAGIX.

1.6 P2 experiment

The P2 experiment is a high-precision study designed to measure the weak charge of the proton, a fundamental parameter of the Standard Model of particle physics. Conducted at the MESA facility, the experiment aims to achieve one of the most precise determinations of the weak mixing angle at low momentum transfer. This measurement is vital for understanding the electroweak interaction, one of nature's four fundamental forces [24].

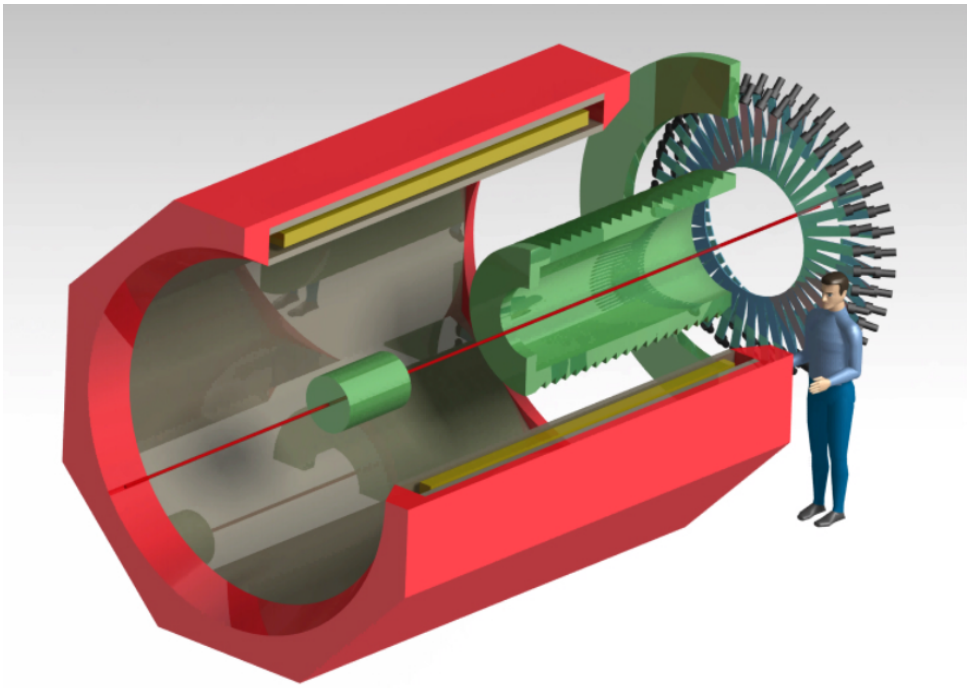

Figure 1.7: CAD design of the integrating spectrometer [17].

The primary objective of the P2 experiment is to determine the weak mixing angle, $\sin^2 \Theta_w$, by measuring the parity-violating (PV) asymmetry in elastic electron-proton scattering, with accuracy comparable to that of current collider experiments (see Fig. 1.8) [24].

The main objective of the P2 experiment is the measurement of parity-violating asymmetry in the scattering of polarized electrons off a liquid hydrogen target.

By analyzing the scattering patterns, the weak charge of the proton can be determined with exceptional precision. This measurement serves as a rigorous test of the Standard Model's predictions and could reveal new physics beyond the current framework.

The P2 experiment requires the spin rotation system and the Chopper for accurate elimination of longitudinal beam halo which may be avoided in MAGIX experiment. This leads to the requirement of a separate electron source with a dedicated shorter beamline for the other experiments happening at MAGIX which so far do not need spin-polarized beam.

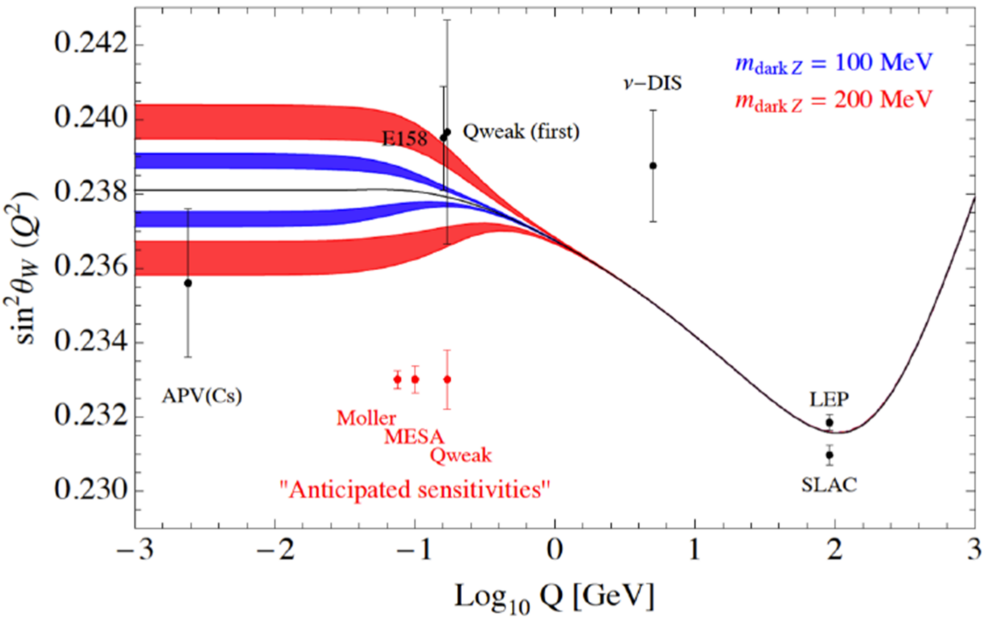

Figure 1.8: Scale dependence of $\sin^2\theta_W$, shown together with completed (black error bars) and planned (red error bars) experimental measurements. The running of the effective weak mixing angle is modified if a dark Z-boson (Z_d) exists [17].

Chapter 2

Basic beam dynamics

This chapter introduces the fundamental concepts of electron beam optics essential for understanding the subsequent sections of this work. Additionally, it provides an overview of the core principles of accelerator physics, which contribute to a deeper understanding of the context of this work. This chapter compiles information from textbook sources [**?**], [**?**].

Moreover, the chapter discusses the so-called "classical" lattices of bending arcs, commonly used in the design of magneto-optical systems for transport channels. It also includes initial evaluations of different lattice configurations for transport channels under linear approximation.

2.1 Introduction

The motion of a particle with charge e in an electric field E and an applied magnetic field with B is described by the equation:

$$\frac{d}{dt}(mv) = e\left(E + [v \times B]\right), \tag{2.1}$$

where the right-hand side represents the Lorentz force. Here, m is the mass, and $v = \dot{r}$ is the velocity of the particle. In the case where a relativistic particle propagates with $v \approx c$, it follows from Equation (2.1) that a transverse magnetic field of 1 T is equivalent to a transverse electric field of approximately 300 MV/m.

Since the real maximum achievable electric field strength at present is approximately 15 MV/m, electric fields are completely ineffective for deflecting high-energy particles in most problems of accelerator physics. Therefore, generally, only magnetic fields are used to control beams of high-energy particles.

In the case of low-energy particles, when they are still non-relativistic, such as heavy ions with energies much below their rest mass energy, it is also reasonable to use electric quadrupoles or solenoids for beam focusing.

To characterize the velocity and energy of accelerated particle are commonly used the Lorentz factor γ and the relativistic velocity β.

The relativistic velocity $\beta_L = \frac{v}{c_{\text{vac}}}$ and the Lorentz factor γ_L are given by:

$$\gamma_L = 1 + \frac{E_{\text{kin}}}{E_0} = \left(\sqrt{1 - \left(\frac{v}{c_{\text{vac}}}\right)^2}\right)^{-1} \tag{2.2}$$

Here, v is the particle velocity, c_{vac} is the speed of light, β_L is the velocity ratio, γ_L is the Lorentz factor, E_{kin} is the kinetic energy of the particle, and $E_0 = mc^2$ is its rest energy.

The Lorentz factor γ_L quantifies how relativistic effects such as time dilation, length contraction, and effective mass increase affect particles moving at velocities close to the speed of light. As v approaches c_{vac}, γ_L increases rapidly. This relation also connects kinetic energy to the total relativistic energy of the particle.

In the case of a 100 keV electron beam, it cannot be completely considered relativistic, its velocity corresponds to 0.554 of the speed of light, and the Lorentz factor is $\gamma \approx 1.2$.

From Equation (2.1), we derive the differential equations describing the trajectory of a particle moving in a magnetic field in Cartesian coordinates. Suppose a stationary Cartesian coordinate system $\{z, x, s\}$ is given in Fig.(2.1).

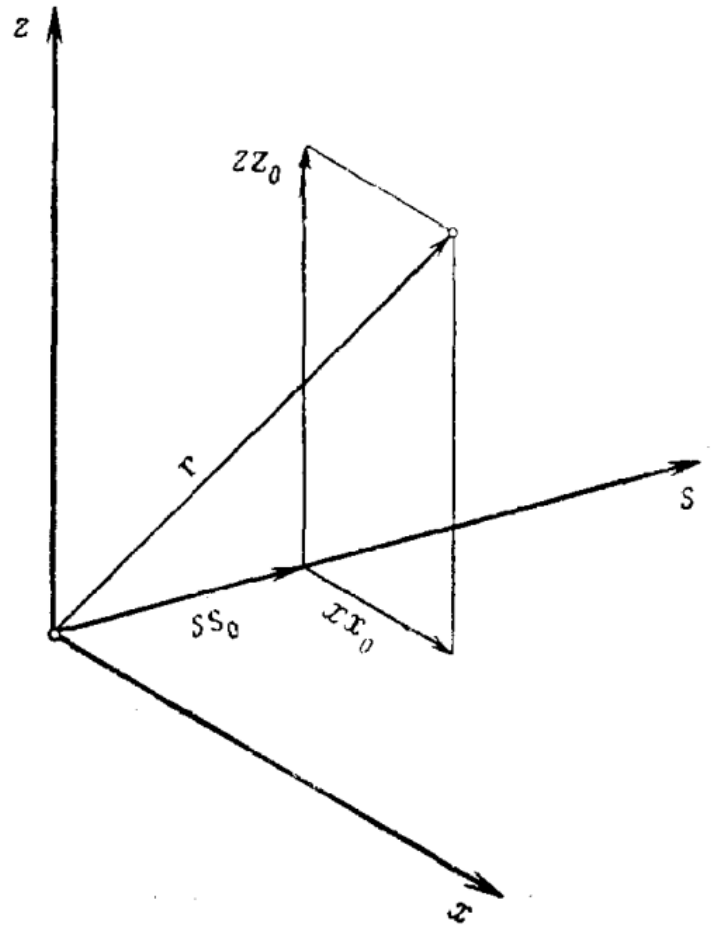

Figure 2.1: Fixed Cartesian coordinate system $\{z, x, s\}$.

In the framework of linear beam dynamics, the beam manipulation is restricted to a few fundamental beam optics elements such as drift space, dipole magnet, quadrupole magnet, and solenoid. These elements are sufficient to guide the beam through an accelerator and to maintain the desired bunch dimensions.

Since charged particles in accelerator move in complex electromagnetic fields, selecting an appropriate reference frame, such as a co-moving coordinate system, simplifies the analysis of their dynamics.

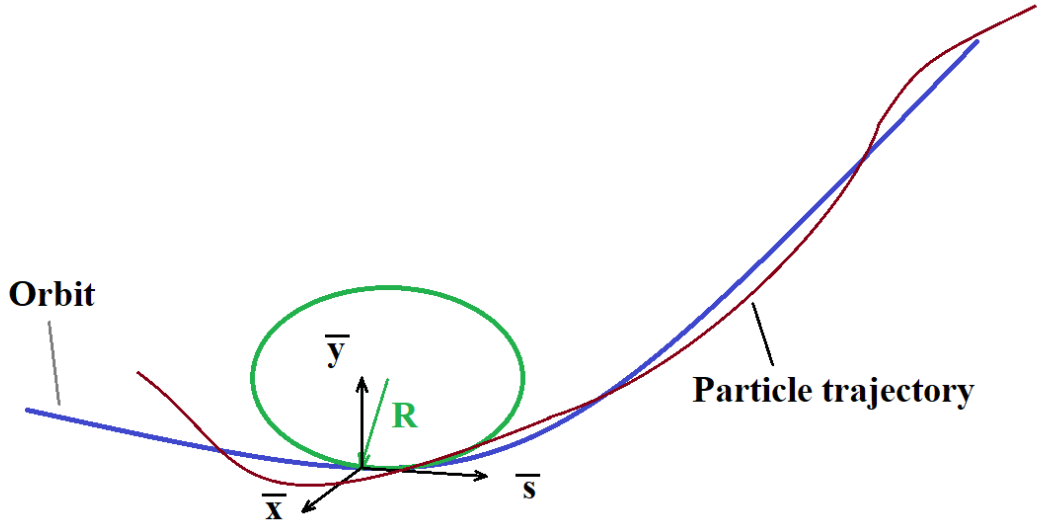

Figure 2.2: Co-moving coordinate system.

A magnetic field or transverse electric field can deflect the beam and we use magnets as guiding and focusing elements for particle beam dynamics. A charged particle in a magnetic field follows a path defined by the equilibrium between centrifugal and Lorentz force.

Beam deflection in a magnetic field is derived from the equilibrium of the centrifugal force and the Lorentz force:

$$\frac{\gamma m v^2}{\rho} = \frac{e}{c} v |\mathbf{B}| \tag{2.3}$$

where we assume that the direction of the particle velocity $\mathbf{v}$ is orthogonal to the magnetic field: $\mathbf{v} \perp \mathbf{B}$. A pure dipole field deflects a charged particle beam onto a circular path with a bending radius ρ. The bending radius ρ is defined as

$$\rho = \frac{p}{q} \cdot \frac{1}{|\mathbf{B}_0|}, \tag{2.4}$$

here, $\beta = v/c$ represents the particle's normalized velocity. The particle momentum is given by p, while B_0 stands for the uniform magnetic flux density.

In this work, the bending radius of the dipole magnet is on the order of 10 cm, whereas the beam radius is on the order of millimeters.

At the beginning, it is necessary to define a coordinate system for the particles. It is common to declare a co-moving coordinate system Fig.(2.2) to reduce the mathematical effort, as the beam dimensions are very small compared with the size of the accelerator.

This coordinate system moves along the orbit determined by the magnetic structure of the accelerator. Thus, the orbit describes the ideal particle trajectory.

The coordinate system is spanned by the axes x, y, and z, allowing the description of all particle coordinates with respect to the orbit [14].

Typically, in particle accelerators, a high number of particles are grouped in an ensemble, called bunch. For example, an electron bunch with the charge of 7.7 pC corresponds to approximately 4.8×10^7 particles.

Each particle within an ensemble does not necessarily share the same properties as the nominal particle such as a slightly different momentum, a small shift in transverse or longitudinal position, or a slightly different kinetic energy compared to the nominal particle. This results in each charged particle within the bunch following a slightly different trajectory. For changing the direction of such charged beams, bending magnets are used.

Quadrupole magnets provide focusing through a field gradient defined as

$$g = \frac{\partial B_y}{\partial x} = \frac{\partial B_x}{\partial y}.$$

The corresponding focusing strength, k, is expressed as in [15]:

$$k = \frac{qg}{p}. \tag{2.5}$$

A short quadrupole magnet with focusing strength k and length l has a approximately focal length $f = (k \cdot l)^{-1}$. The motion of a particle in linear approximation can be described by Hill's equation [15]:

$$x''(s) + \left(\frac{1}{\rho^2(s)} - k(s)\right) x(s) = \frac{1}{\rho(s)} \cdot \frac{\Delta p}{p_0}, \tag{2.6}$$

$$y''(s) + k(s)y(s) = 0. \tag{2.7}$$

In this context, x and y denote the particle's transverse coordinates, while $\rho(s)$ represents the bending radius at a given longitudinal position s. The term $\Delta p = p - p_0$ describes the deviation of the particle's momentum from that of the reference particle.

A particle's location within the accelerator is defined by its coordinates in the configuration space. The components of the vector $\vec{X}(s)$ are expressed relative to the nominal particle's position [16, 25].

$$\vec{X}(s) = \begin{pmatrix} x \\ x' \\ y \\ y' \\ z \\ z' \end{pmatrix} = \begin{pmatrix} x \\ \frac{p_x}{p_0} \\ y \\ \frac{p_y}{p_0} \\ \delta l \\ \frac{\Delta p}{p_0} \end{pmatrix} = \begin{pmatrix} \text{horizontal displacement} \\ \text{horizontal divergence} \\ \text{vertical displacement} \\ \text{vertical divergence} \\ \text{longitudinal displacement} \\ \text{relative momentum deviation} \end{pmatrix}. \tag{2.8}$$

The motion of particles in a sector bending magnet is described by the Hill's equation as shown in Equation (2.9). This is the matrix of a sector bending magnet in which the reference trajectory enters and exits perpendicular to the field lines.

Solving these equations for the body of a dipole magnet we obtain the transfer matrix, with $\varphi = l/\rho$, where l is the arc length of the orbit. The transfer matrix of dipole magnet is given by M_{dipole}.

The motion of a charged particle traveling through a structured arrangement of magnets, known as a lattice, can be described using the transfer matrix formalism. This method involves determining a transfer matrix for each individual lattice element. The matrix itself is a 6×6 representation, accounting for all three spatial coordinates: x, y, and z. For the sector dipole magnet the transport matrix will be the following:

$$M_{\text{dipole}} = \begin{pmatrix} \cos(\varphi) & \rho\sin(\varphi) & 0 & 0 & 0 & \frac{\rho}{\beta_0}(1-\cos(\varphi)) \\ -\frac{1}{\rho}\sin(\varphi) & \cos(\varphi) & 0 & 0 & 0 & \frac{1}{\beta_0}\sin(\varphi) \\ 0 & 0 & 1 & s & 0 & 0 \\ 0 & 0 & 0 & 1 & 0 & 0 \\ -\frac{1}{\beta_0}\sin(\varphi) & -\frac{\rho}{\beta_0}(1-\cos(\varphi)) & 0 & 0 & 0 & \frac{1}{\gamma_0^2\beta_0^2} + \rho\sin(\varphi) - l \\ 0 & 0 & 0 & 0 & 1 & 0 \end{pmatrix}. \tag{2.9}$$

Looking at a particle on the reference trajectory but with a momentum deviation, we can define from M_{dipole}

$$\Delta x_D = D(s)\frac{\Delta p}{p_0} \tag{2.10}$$

$$\Delta x'_D = D'(s)\frac{\Delta p}{p_0} \tag{2.11}$$

Here, the matrix element M_{16} is commonly referred to as the horizontal dispersion function $D(s)$. The dispersion function is a particular solution to the inhomogeneous Hill's equation. This function describes the displacement of a particle's trajectory due to a deviation in its momentum from the reference value. It appears in the expression:

$$x(s) = x_\beta(s) + D(s) \cdot \delta, \tag{2.12}$$

where $x(s)$ is the total horizontal position, $x_\beta(s)$ is the betatron (oscillatory) component, $D(s)$ is the dispersion function, and $\delta = \Delta p/p$ is the relative momentum deviation.

$$x_n = M_{11} \cdot x + M_{12} \cdot x' + M_{16} \cdot \frac{\Delta p}{p} \tag{2.13}$$

$$y_n = M_{33} \cdot y + M_{34} \cdot y' + M_{36} \cdot \frac{\Delta p}{p} \tag{2.14}$$

$$z_n = M_{51} \cdot x + M_{52} \cdot x' + M_{53} \cdot y + M_{54} \cdot y' + M_{55} \cdot z + M_{56} \cdot \frac{\Delta p}{p} \tag{2.15}$$

In the case of a sector bending magnet with a bending radius of $\rho = 0.1$ m and a bending angle of $\varphi = \frac{\pi}{2}$ and $\beta_0 \approx 0.554$ the horizontal dispersion function at the exit is given by the matrix element M_{16}:

$$D = \frac{\rho}{\beta_0}(1 - \cos\varphi)$$

The dispersion becomes:

$$D = \frac{1}{0.554}(1 - \cos\frac{\pi}{2}) = 0.18 \text{ m}$$

Thus, the horizontal dispersion at the exit of the dipole is $D = 0.18$ m.

2.2 Matrix representation of quadrupole and transfer matrix

The motion of a charged particle in linear approximation (We assume that $1/\rho^2 = 0$, i.e., no dipole component) can be described by the Hill's equation (2.16) and (2.17).

$$x''(s) - k(s) \cdot x(s) = 0 \tag{2.16}$$

$$y''(s) + k(s) \cdot y(s) = 0 \tag{2.17}$$

Each optical element influences the trajectory of particles in the beam through its respective transfer matrix. By solving Hill's equations (2.16) and (2.17), the mathematical formulation for each matrix component can be obtained.

From equations (2.16) and (2.17), it follows that if $k < 0$, the quadrupole acts as a defocusing element in the horizontal transverse plane and as a focusing element in the vertical plane. Conversely, if $k > 0$, the quadrupole focuses in the horizontal transverse plane and defocuses in the vertical plane.

Solving these equations leads to the evolution of the transfer matrices for quadrupoles, where $\psi = \sqrt{|k|} \cdot l$, $\gamma_0 = 1/\sqrt{1-(v/c)^2} = E_0/(m_0c^2)$, and $\beta_0 = v/c$.

$$M_{FQ} = \begin{pmatrix} \cos(\psi) & \frac{1}{\sqrt{|k|}}\sin(\psi) & 0 & 0 & 0 & 0 \\ -\sqrt{|k|}\sin(\psi) & \cos(\psi) & 0 & 0 & 0 & 0 \\ 0 & 0 & \cosh(\psi) & \frac{1}{\sqrt{|k|}}\sinh(\psi) & 0 & 0 \\ 0 & 0 & \sqrt{|k|}\sinh(\psi) & \cosh(\psi) & 0 & 0 \\ 0 & 0 & 0 & 0 & 1 & \frac{l}{\gamma_0^2\beta_0^2} \\ 0 & 0 & 0 & 0 & 0 & 1 \end{pmatrix} \tag{2.18}$$

$$M_{DQ} = \begin{pmatrix} \cosh(\psi) & \frac{1}{\sqrt{|k|}}\sinh(\psi) & 0 & 0 & 0 & 0 \\ \sqrt{|k|}\sinh(\psi) & \cosh(\psi) & 0 & 0 & 0 & 0 \\ 0 & 0 & \cos(\psi) & \frac{1}{\sqrt{|k|}}\sin(\psi) & 0 & 0 \\ 0 & 0 & -\sqrt{|k|}\sin(\psi) & \cos(\psi) & 0 & 0 \\ 0 & 0 & 0 & 0 & 1 & \frac{l}{\gamma_0^2\beta_0^2} \\ 0 & 0 & 0 & 0 & 0 & 1 \end{pmatrix} \tag{2.19}$$

Sections of the beamline where charged particles travel freely during length l without the influence of external magnetic or electric fields are called drifts, are described as:

$$M_{drift} = \begin{pmatrix} 1 & l & 0 & 0 & 0 & 0 \\ 0 & 1 & 0 & 0 & 0 & 0 \\ 0 & 0 & 1 & l & 0 & 0 \\ 0 & 0 & 0 & 1 & 0 & 0 \\ 0 & 0 & 0 & 0 & 1 & \frac{l}{\gamma_0^2\beta_0^2} \\ 0 & 0 & 0 & 0 & 0 & 1 \end{pmatrix} \tag{2.20}$$

Solenoids are used to focus beams of charged particles, especially at low energies where traditional quadrupole magnets are less effective.

Solenoid creates an axially symmetric magnetic field, inducing spiral motion of particles and reducing beam divergence. The solenoid introduces the maximum amplitude is $\sqrt{\beta(s)\,\varepsilon}$.

The transfer matrix for a solenoid is given by hard–edge model geometric length L and on–axis field B_s could be defined

$$M_{\mathrm{SOL}}^{(\mathrm{lab})} = \begin{pmatrix} C^2 & \frac{SC}{\kappa} & SC & \frac{S^2}{\kappa} & 0 & 0 \\ -\kappa SC & C^2 & -\kappa S^2 & SC & 0 & 0 \\ -SC & -\frac{S^2}{\kappa} & C^2 & \frac{SC}{\kappa} & 0 & 0 \\ \kappa S^2 & -SC & -\kappa SC & C^2 & 0 & 0 \\ 0 & 0 & 0 & 0 & 1 & \frac{l}{\gamma_0^2\beta_0^2} \\ 0 & 0 & 0 & 0 & 0 & 1 \end{pmatrix} \tag{2.21}$$

where:

$$\kappa = \frac{B_s}{2(B\rho)_0}, \qquad \phi = \kappa\, l, \qquad C = \cos\phi, \quad S = \sin\phi.$$

The phase–space vector is ordered as $(x,\, x',\, y,\, y',\, z,\, \delta)$ with $\delta = \Delta p/p_0$. The longitudinal coordinate z is measured with respect to the reference particle; with this convention the longitudinal block is drift–like and yields $R_{56} = l/(\gamma_0^2\beta_0^2)$.

In case in we need to calculate the particle trajectory in set of optical elements, we need use the total transport matrix M_{total}. Such matrix describes the transformation of a particle's trajectory through an optical system. The general form of coordinates transformation in the optical system is:

$$\begin{pmatrix} x_2 \\ x_2' \\ y_2 \\ y_2' \\ z_2 \\ z_2' \end{pmatrix} = M_{total} \begin{pmatrix} x_1 \\ x_1' \\ y_1 \\ y_1' \\ z_1 \\ z_1' \end{pmatrix} \tag{2.22}$$

where M is the transfer matrix that governs the evolution of beam coordinates. For a sequence of optical elements, the total transfer matrix is obtained by multiplying individual matrices of all optical elements in the optical system:

$$M_{\mathrm{total}} = M_n M_{n-1} \ldots M_2 M_1. \tag{2.23}$$

2.3 Twiss parameters

The equilibrium orbit in a circular particle accelerator is determined by the configuration of the magnetic field, which is set by the arrangement of the magnets. Charged particles in such machine oscillate around the reference trajectory in both transverse planes. These oscillations are known as betatron oscillations. The location-dependent amplitude $\beta(s)$ of such an oscillation in a transverse plane is called the betatron function.

The betatron oscillation of a single particle along a lattice section can be expressed by:

$$x(s) = \sqrt{\varepsilon \cdot \beta(s)} \cos\left(\Psi(s) + \phi\right), \tag{2.24}$$

where ε is the transverse emittance and ϕ the initial phase. $\Psi(s)$ phase advance of the betatron oscillation, defined as:

$$\Psi(s) = \int_0^s \frac{d\tilde{s}}{\beta(\tilde{s})}. \tag{2.25}$$

Thus, if the betatron function is known along a lattice section, the phase function $\Psi(s)$ can be calculated.

Additionally, two more parameters are required to describe the particle dynamics - $\alpha(s)$ and $\gamma(s)$, this parameters called the Twiss parameters. They describe the impact of the linear lattice on the particle ensemble in an accelerator.

They are defined as:

$$\alpha(s) = -\frac{\beta'(s)}{2}, \qquad \gamma(s) = \frac{1 + \alpha^2(s)}{\beta(s)}. \tag{2.26}$$

In accelerator physics, the characterization of transverse beam dynamics and stability commonly employs the Courant–Snyder, or Twiss, parameters. These parameters—α, β, and γ—provide a complete description of the transverse phase-space ellipse defined by particle trajectories in position (x) and angle ($x' = dx/ds$, where s is the longitudinal coordinate along the accelerator beamline). The general form of the Courant–Snyder ellipse equation in transverse phase space is given by

$$\gamma x^2 + 2\alpha x x' + \beta x'^2 = \varepsilon,$$

where ε is the transverse emittance, representing the area occupied by the beam in phase space, thus reflecting the intrinsic beam quality.

Among these parameters, the β-function called the amplitude or betatron function—is particularly crucial, as it determines the local transverse beam size and how particle trajectories evolve along the accelerator.

The physical significance of the β-function is expressed through its direct relationship to the root mean square (RMS) beam size σ_x via the beam emittance ε as follows:

$$\sigma_x(s) = \sqrt{\varepsilon\beta(s)}.$$

2.4 Phase space and emittance

The motion of charged particles in an accelerator can be described using phase space coordinates. There are two transverse phase spaces, (x, x') and (y, y'), and one longitudinal phase space: (z, z') as it is the case in the majority of the literature, (s, dE) or $(d\phi_{\mathrm{RF}}, dE)$. Here ϕ_{RF} - the accelerator phase. In the longitudinal phase space (s, dE), the parameter dE describes the energy spread of the beam. An example of such ellipse is shown in Fig.(2.2).

The parameters x, y, s define a three-dimensional coordinate system, where $x' = dx/dz$ and $y' = dy/dz$ correspond to the associated angles. The distribution of particles in phase space is typically approximated by an ellipse. If linear forces act on an ellipse, it remains an ellipse, simplifying beam optics calculations.

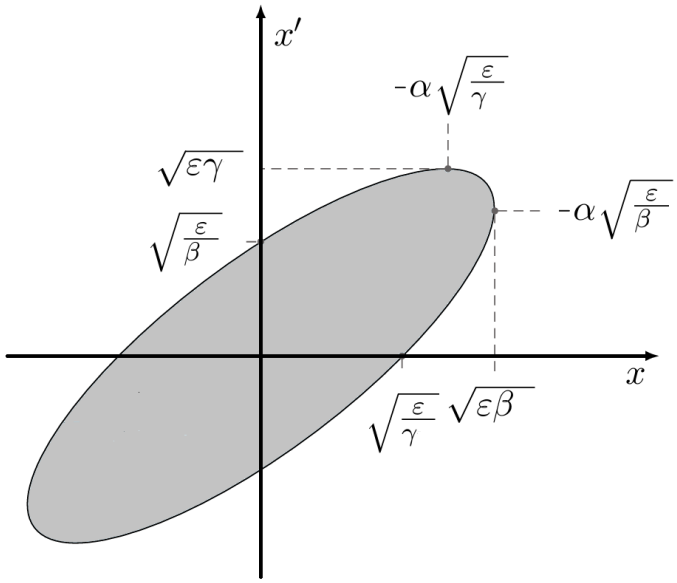

Figure 2.3: Example of a two-dimensional transversal phase space with the relations of the Twiss parameters.

The Twiss parameters, also known as Courant-Snyder parameters [10], describe the envelope and focusing properties of a charged particle beam in an accelerator. These parameters characterize the shape and evolution of the beam in phase space and are essential for beam transport and optics calculations.

The Twiss parameters satisfy the following condition:

$$\gamma_T \beta_T - \alpha_T^2 = 1. \tag{2.27}$$

The emittance ϵ defines the phase space volume occupied by the beam and relates to the area A_e of the ellipse as:

$$\epsilon = \frac{A_e}{\pi}. \tag{2.28}$$

Since the beam lacks a well-defined boundary, practical definitions involve statistical measures like the RMS emittance, computed from the second moments of the distribution. The RMS beam size and divergence are related to the ellipse parameters:

$$\langle x^2 \rangle = \beta_T \epsilon_x = m_{11}, \tag{2.29}$$

$$\langle x'^2 \rangle = \gamma_T \epsilon_x = m_{22}, \tag{2.30}$$

with α_T given by:

$$\alpha_T = -\frac{\langle x x' \rangle}{\epsilon_x}. \tag{2.31}$$

The same relations apply to the y axis. These parameters can be grouped into the beta matrix M_β [25].

$$M_\beta = \begin{pmatrix} m_{11} & m_{12} \\ m_{12} & m_{22} \end{pmatrix} = \epsilon_x \begin{pmatrix} \beta_T & -\alpha_T \\ -\alpha_T & \gamma_T \end{pmatrix}. \tag{2.32}$$

The RMS emittance is expressed as:

$$\epsilon_x = \sqrt{\det(M_\beta)} \tag{2.33}$$

RMS emittance describes the area that a beam of charged particles occupies in the position–angle (or position–momentum) phase space and allows for evaluating the quality of the beam (its focus, divergence). Statistically, it is defined as

$$\varepsilon_{\mathrm{x}} = \sqrt{\langle x^2 \rangle \langle x'^2 \rangle - \langle x\, x' \rangle^2}$$

The parameters $\langle x^2 \rangle$ is the variance of the position coordinate x, $\langle x'^2 \rangle$ is the variance of the angular coordinate x', and $\langle x\, x' \rangle$ captures the correlation between position and angle.

It is important to mention Liouville's theorem, which states that in the absence of dissipative forces, the phase space volume occupied by a beam remains constant over time [25]. However, as considered in this work, in nonlinear beam dynamics with strong space-charge effect the Liouville emittance remains conserved, whereas the RMS emittance can increase due to the distortion of the phase-space distribution.

2.5 Field in Taylor series

We will consider the movement of charged particles in vacuum chambers of accelerators, where there are no electric currents creating a magnetic field. In classical electrodynamics

$$\nabla \times \mathbf{B} = \mu_0 \mathbf{j}, \tag{2.34}$$

$$\nabla \cdot \mathbf{B} = 0, \tag{2.35}$$

where $\mathbf{j}$ is the current density.

In the absence of currents, Equation (2.34) takes the next form

$$\nabla \times \mathbf{B} = 0. \tag{2.36}$$

A magnetic field with zero curl is called a potential field and can be expressed in terms of a scalar magnetic potential

$$\mathbf{B} = -\nabla V. \tag{2.37}$$

Substituting Equation. (2.37) into Equation. (2.35) gives Laplace's equation for the scalar potential

$$\Delta V = 0. \tag{2.38}$$

The magnetic field is expressed through the vector potential $\mathbf{A}$ as

$$\mathbf{B} = \nabla \times \mathbf{A}. \tag{2.39}$$

The length of the elements is, as a rule, much greater than their aperture, and therefore, to a good approximation, we can consider the fields to be purely transverse. hence, to a good approximation, the fields can be treated as purely transverse. Taking this into account, we assume that the vector potential has only a longitudinal component,

$$\mathbf{A} = A_s(x, y)\, \mathbf{s_0},$$

and varies weakly along s (i.e., $\partial/\partial s \approx 0$). Combining Equations. (2.37) and (2.39) we get

$$B_x = -\frac{\partial V}{\partial x} = \frac{\partial A_s}{\partial y}, \qquad B_y = -\frac{\partial V}{\partial y} = -\frac{\partial A_s}{\partial x}. \tag{2.40}$$

From the vector analysis it is known that this formula defines a vector $\overline{A}$ such as

$$\mathbf{B} = -\nabla \times \mathbf{A} = \left(\frac{\partial A_s}{\partial y} - \frac{\partial A_y}{\partial s}\right)\mathbf{x_0} + \left(\frac{\partial A_x}{\partial s} - \frac{\partial A_s}{\partial x}\right)\mathbf{y_0} + \left(\frac{\partial A_y}{\partial x} - \frac{\partial A_x}{\partial y}\right)\mathbf{s_0} \tag{2.41}$$

Vector $\mathbf{A}$ is called the vector potential of field $\mathbf{B}$. let us make one significant assumption about the magnetic field inside the magnetic elements of the accelerator. The length of the elements is, as a rule, much greater than their aperture, and therefore, to a good approximation, we can consider the fields to be purely transverse.

Taking into account this remark, we come to the conclusion that the vector potential has only a longitudinal component. Combining 2.37 and 2.41 we get

$$B_x = -\frac{\partial V}{\partial x} = \frac{\partial A_s}{\partial y}, B_y = -\frac{\partial V}{\partial y} = \frac{\partial A_s}{\partial x} \tag{2.42}$$

On the complex plane $z = x + iy$ we define a complex potential function

$$\tilde{A}(z) = A_s(x, y) + iV(x, y) \tag{2.43}$$

Equations (2.42) define the Cauchy-Riemann conditions for the real and imaginary parts of the analytical function. Thus, the complex potential (2.43) is an analytical function and can be expanded into the series

$$\tilde{A}(z) = \sum_{n=0}^{\infty} k_n z^n, k_n = \lambda_n + i\mu_n \tag{2.44}$$

Where λ, μ are real numbers. The radius of convergence of this series is determined by the region of the absence of current density.

Outside the circle with this condition radius The Cauchy-Riemann equations (2.42) begin to break down and the potential ceases to be an analytical function. This occurs near the poles and coils of magnetic elements.

If we write down series (2.44) in cylindrical coordinates r, ϕ, z, we get

$$x = r\cos\varphi, y = r\sin\varphi, z^n = r^n e^{in\varphi} = r^n(\cos n\varphi + i\sin n\varphi) \tag{2.45}$$

Using the definition of complex potential (2.43) and collecting terms for the real and imaginary parts, we obtain

$$V(r, \varphi) = \sum_{n=0}^{\infty} r^n(\mu_n \cos n\varphi + \lambda_n sinn\varphi) \tag{2.46}$$

$$A_s(r, \varphi) = \sum_{n=0}^{\infty} r^n(\lambda_n \cos n\varphi - \mu_n sinn\varphi) \tag{2.47}$$

In these equations, n - is the harmonic (multipole number) of the potential, λ_n, μ_n - are the amplitudes of the harmonics, and the n-th harmonic is created by a system with

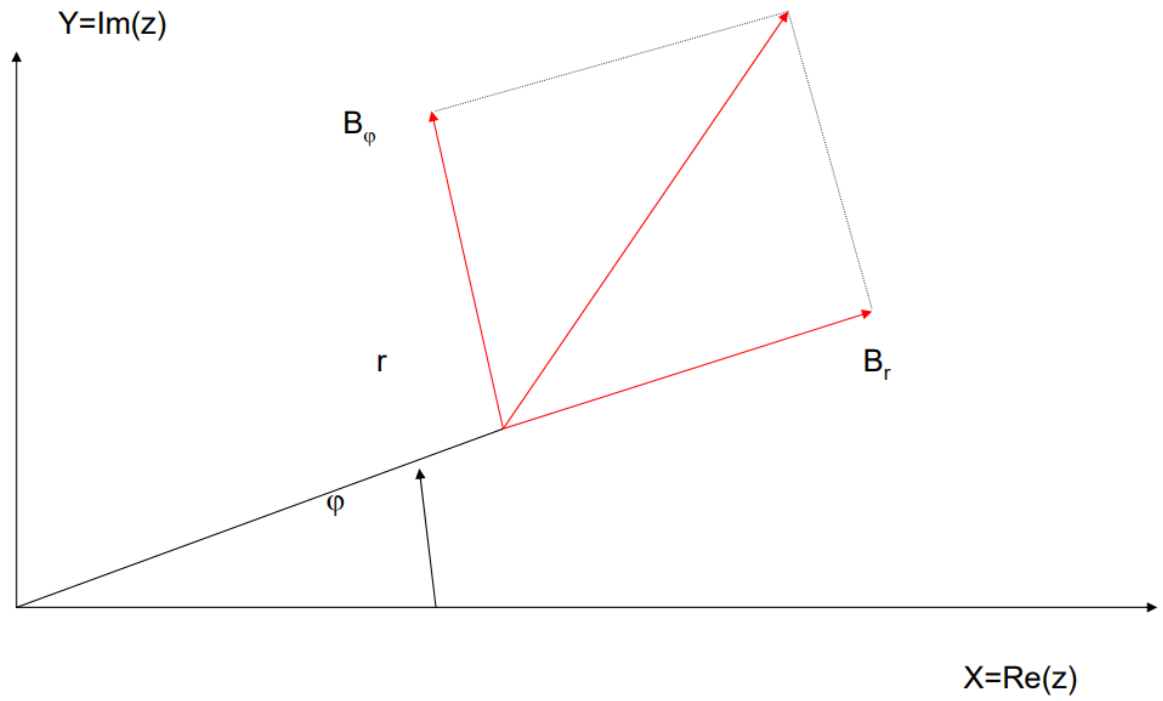

Figure 2.4: Vector $\overline{B}$ in Cylindrical coordinates.

the number of pole pairs equal to n (n = 1 corresponds to a dipole, the potential reaches extrema at $\varphi = \pm\pi/2$; n = 2 - quadrupole, 3 - sextupole etc.).

In accordance with the accepted terminology, terms with $\sin n\varphi$ (terms with λ_n) are called normal components of the potential, and terms with $\cos n\varphi$ (terms with μ_n) are called rotated.

Therefore, normal multipoles cannot have a pole on the X axis, since $\sin n\varphi = 0$ for $\varphi = 0$. In order to obtain a rotated multipole from a normal one, it needs to be rotated by an angle $\phi = 2\pi/n$

If we express the gradient in cylindrical coordinates from $V(r, \varphi)$, we obtain expressions for the B_r and B_φ components of the magnetic field.

Terms with n = 0 in potentials do not contribute to the magnetic field, so we can replace the summation from n = 0 to summation from n = 1.

$$B_\varphi = -\frac{1}{r}\frac{\partial V}{\partial \varphi} = -\sum_{n=0}^{\infty} n(\lambda_n \cos n\varphi - \mu_n sinn\varphi) r^{n-1} \tag{2.48}$$

$$B_r = -\frac{\partial V}{\partial r} = -\sum_{n=0}^{\infty} n(\mu_n \cos n\varphi + \lambda_n sinn\varphi) r^{n-1} \tag{2.49}$$

From the last expressions it is easy to obtain that the amplitude of the n-th harmonic of the magnetic field does not depend on the angle φ and is determined only by the radius r. So, the field amplitude is constant on a circle of radius r.

$$|B| = \sqrt{B_\varphi^2 + B_r^2} \tag{2.50}$$

Let us write the series for the potential 2.44 in Cartesian coordinates and, collecting real and imaginary terms and taking the gradient from $-V(x,y)$, we obtain the expressions for the field components given in Table 2.1

Table 2.1: Field components in Cartesian coordinate system

Multipole	**Normal component**	**Skew component**
Dipole ($n=1$)	$B_y = -\lambda_1, \quad B_x = 0$	$B_x = -\mu_1, \quad B_y = 0$
Quadrupole ($n=2$)	$B_y = -2\lambda_2 x, \quad B_x = -2\lambda_2 y$	$B_y = \mu_2 y, \quad B_x = -\mu_2 x$
Sextupole ($n=3$)	$B_y = -3\lambda_3(x^2-y^2), \quad B_x = -6\lambda_3 xy$	$B_y = 6\mu_3 xy, \quad B_x = -3\mu_3(x^2-y^2)$

Let us expand the field in the median plane (at y = 0) into a Taylor series

$$\begin{aligned} B_y(x) &= B_0 + \frac{1}{1!}\frac{\partial B_y}{\partial x}x + \frac{1}{2!}\frac{\partial^2 B_y}{\partial x^2}x^2 + \cdots + \frac{1}{n!}\frac{\partial^n B_y}{\partial x^n}x^n \\ &= B_0\rho\left(\frac{1}{\rho} + \frac{1}{1!}\frac{G^1}{B_0\rho}x + \frac{G^2}{2!B_0\rho}x^2 + \frac{G^3}{3!B_0\rho}x^3 + \cdots + \frac{G^n}{n!B_0\rho}x^n\right) \\ &= B_0\rho\left(K_0 + \frac{1}{1!}K_1 x + \frac{1}{2!}K_2 x^2 + \cdots + \frac{1}{n!}K_n x^n\right) \end{aligned} \tag{2.51}$$

In these expressions, $B_o\rho$ is the so-called magnetic rigidity system, equal to the product of the field on an ideal equilibrium (reference) orbit at the radius of this orbit in dipoles. For a relativistic particle, the magnetic rigidity can be determined from the expression

$$E[GeV] = 0.29979 B_0[T]\rho[m] \tag{2.52}$$

The value K_n

$$K_n = \frac{1}{B\rho}\frac{\partial B_y^n}{\partial x^n} = \frac{G^n}{B_0\rho} \tag{2.53}$$

Is called an $n-th$ order multipole force. Comparing the expansion 2.51 and the fields in the Table. 2.1, we can find that

$$\lambda_n = \frac{\partial B_y^{n-1}}{\partial x^{n-1}}/(n-1)! = -\frac{G^{n-1}}{(n-1)!} \tag{2.54}$$

In this expression, $\frac{\partial B_y}{\partial x} = G_1$ represents the quadrupole gradient, and $\frac{\partial^2 B_y}{\partial x^2} = G_2$ represents the sextupole gradient, and so on. In the general case, the normal components of the field of an nth-order multipole are determined by the following expressions:

$$B_y^{(n)}(x,y) = B_0\rho\frac{K_n}{n!}(\frac{\partial}{\partial y}Im(x+iy)^{n+1}) \tag{2.55}$$

$$B_x^{(n)}(x,y) = B_0\rho\frac{K_n}{n!}(\frac{\partial}{\partial x}Im(x+iy)^{n+1}) \tag{2.56}$$

2.6 Buncher

The bunching system at the MESA accelerator allows shaping the longitudinal structure of the electron beam prior to its injection into the first acceleration section of MAMBO. It is part of the low-energy beam transport line MELBA.

The bunching system consists of two sequential RF cavities.

The first buncher operates at 1.3 GHz, which corresponds to the main RF frequency of the accelerator. The second buncher operates at the doubled frequency of 2.6 GHz.

This two-stage structure enables progressive longitudinal focusing of the beam: the first cavity introduces an initial energy modulation along the bunch, and the second enhances it, resulting in more effective bunch compression and correction of the longitudinal phase space distribution.

Such a configuration enables efficient velocity modulation of electrons, compressing the bunch to the desired length before injection into the MESA accelerating structures [65].

In this work, beam bunching was achieved using only one buncher operating at a frequency of 1.3 GHz.

The appearance of the buncher is shown in fig. 2.5.

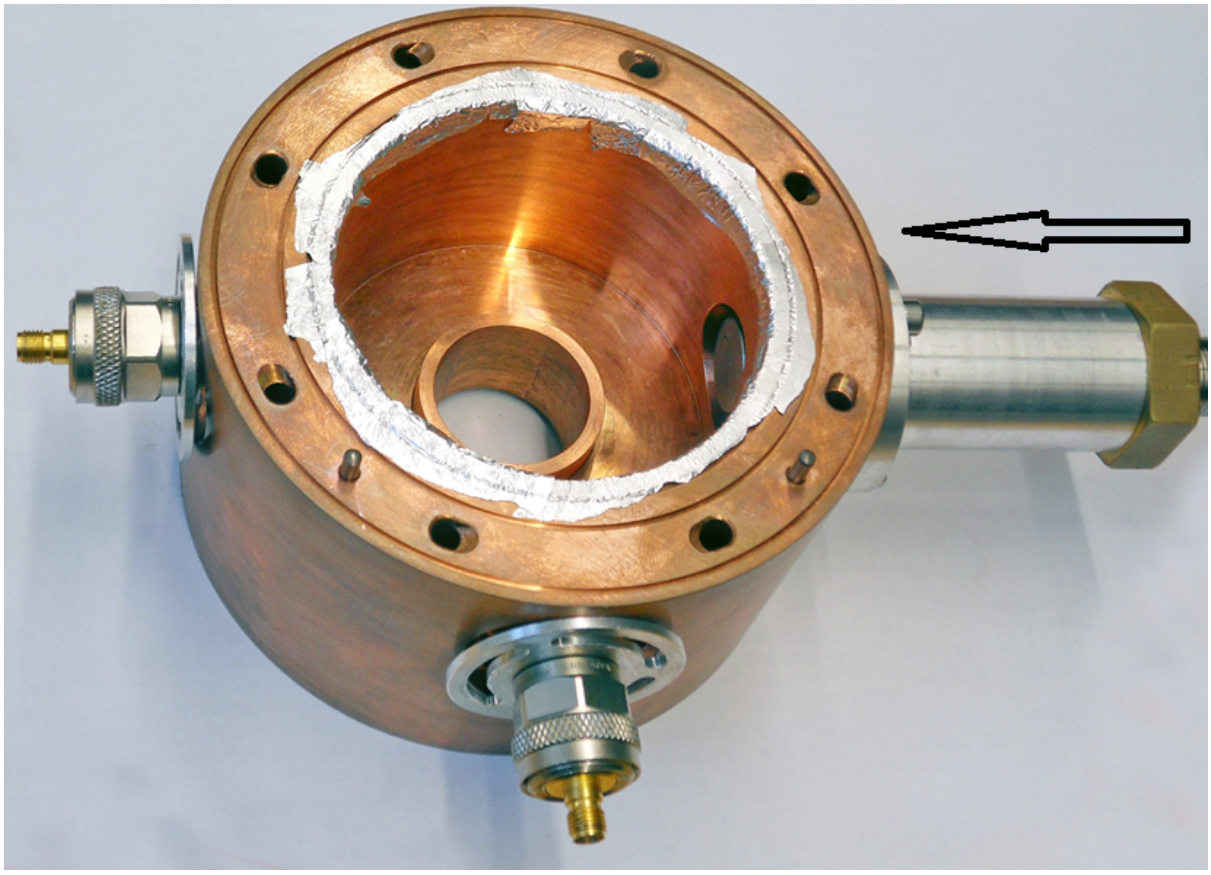

Figure 2.5: The appearance of the 1.3 GHz buncher cavity. The tuning cylinder (arrow) is on the right; the power coupler and tuning antenna are at the bottom and on the left, respectively.

A pillbox buncher is a type of RF cavity used in accelerators to modulate the velocity of charged particle bunches. It operates at a resonant frequency, generating an electric

field that interacts with the particles, compressing their longitudinal phase space. The pillbox design is characterized by a cylindrical cavity with a simple TM_{010} mode, providing efficient energy modulation for beam bunching before injection into the main acceleration section [46].

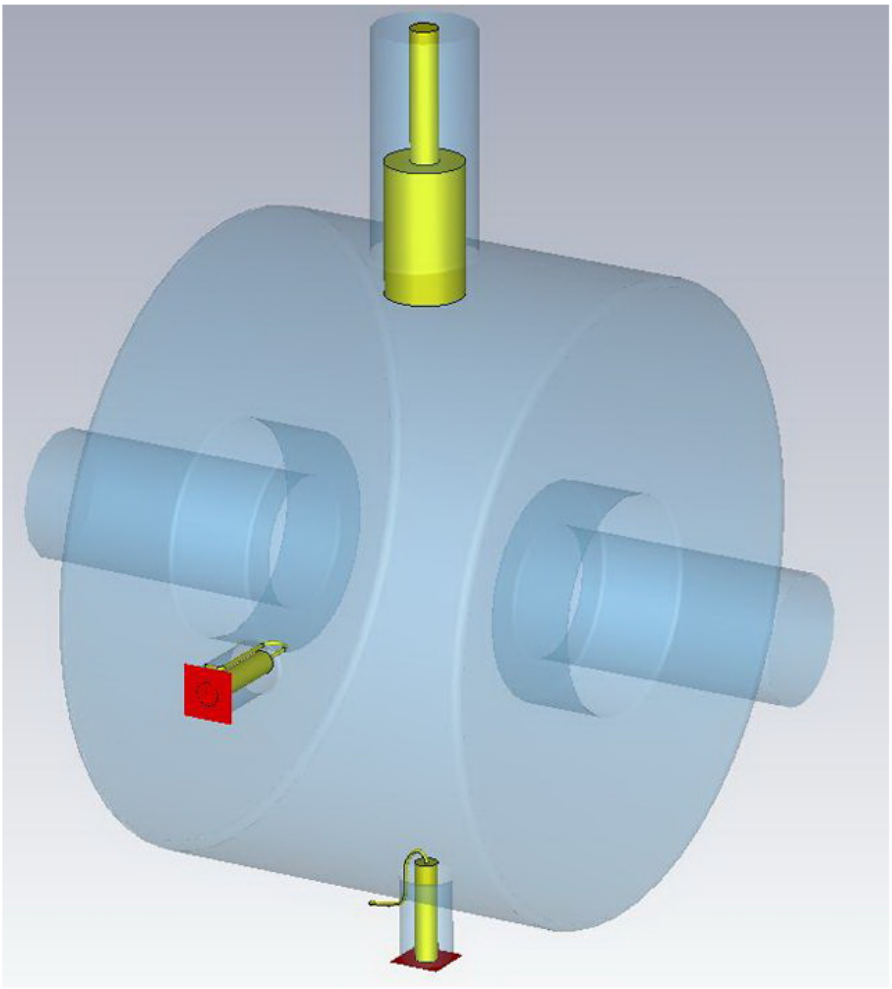

Figure 2.6: CST model of the buncher cavity for 1.3 GHz. The yellow components is the RF power couplers and diagnostic ports attached to this cavity.

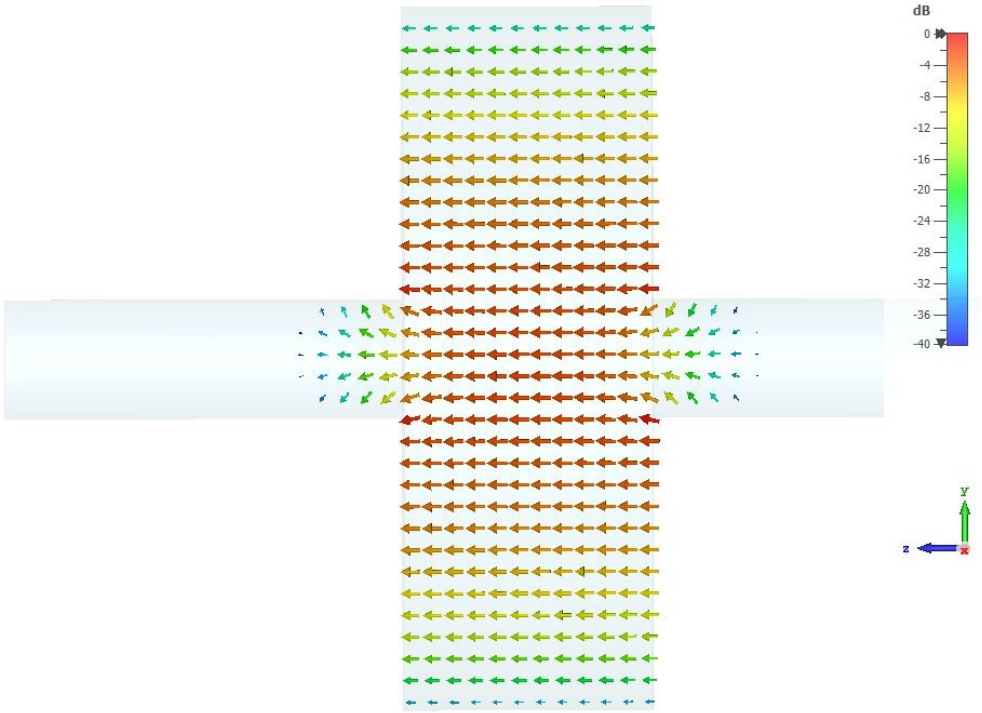

Figure 2.7: Electric field inside the buncher.

Figure 2.6 shows the CST model of the buncher used, while Figure 2.7 presents the electric field inside it and the main parameters of the buncher are shown in the Table 2.2.

Parameter	Value
L_0	61.76 mm
y	10 mm
x	20 mm
R	73 mm
R_b	15 mm
R_e	0 mm
a	10 mm
R_s/Q_0	407

Table 2.2: Main parameters of the 1.3 GHz buncher cavity. [46]

2.7 Debye length

In the case of beam dynamics simulation with high space charge in accelerator, the Debye length plays an important role in determining the interactions between electric fields within the charged beam [31].

A shorter Debye length corresponds to stronger electrostatic screening, meaning that the fields generated by individual electrons are rapidly screened by surrounding charges, reducing the range of Coulomb interactions [32].

On the contrary, a longer Debye length indicates weaker screening, allowing electrostatic fields to extend over larger distances. Thereby affecting beam dynamics, stability,

and space charge effects. Understanding and calculating the Debye length is important for accurate simulation space charge effects and optimizing beam quality [33].

The Debye length is defined as [34]

$$\lambda_D = \sqrt{\frac{\varepsilon_0 k_B T}{q_e^2 n}}. \tag{2.57}$$

k_B is the Boltzmann constant, n - the charge density, and is defined as

$$n = \frac{q_\mathrm{b}}{q_e \beta c \tau_\mathrm{b} \sigma_\mathrm{x} \sigma_\mathrm{y}}, \tag{2.58}$$

where, q_b - the bunch charge, τ_b - the temporal bunch length, $\sigma_{\mathrm{x,y}}$ - both transverse RMS bunch sizes, q_e - the electron charge, β - the relativistic velocity, c - speed of light. The temperature T of the electron beam is related to the normalized emittance ε as [59]

$$k_B T = \frac{E_0 \varepsilon^2}{\sigma_L^2}, \tag{2.59}$$

Here, E_0 denotes the rest energy of an electron, while σ_L is RMS size of the laser spot.

If $\lambda_D \gg \sigma_\mathrm{b}$, Debye shielding is very weak, indicating an emittance-dominated regime in which the electrons within the bunch are primarily influenced by external forces.

Conversely, if $\lambda_D \ll \sigma_\mathrm{b}$, the system enters the space-charge-dominated regime, where the electrons within the bunch are more strongly affected by interactions with their neighbors than by external forces. This occurs because the collective electric fields of the electrons effectively shield them from external influences [31].

Let us estimate the Debye length of an electron bunch with a 7.7 pC charge at the entrance to the designed separation beamline using the following parameters:

- Beam energy (E): 100 keV = 100×10^3 eV
- Bunch charge (q_b): 7.7 pC = 7.7×10^{-12} C
- Normalized emittance (ε_n): 1 mm·mrad
- Transverse bunch size: $\sigma_x = 1$ mm, $\sigma_y = 1$ mm
- Bunch length (σ_z): 7 mm = 7×10^{-3} m

Debye length of such electron bunch

$$\lambda_D = \sqrt{\frac{\varepsilon_0 k_B T}{n q_e^2}} \tag{2.60}$$

$$\lambda_D \approx 0.05\,\mathrm{mm} \tag{2.61}$$

The Debye length of such an electron bunch is approximately 0.05 mm. Comparing this with the transverse RMS sizes of the electron bunch is approximately 1 mm, it is evident that $\lambda_D \ll \sigma_\mathrm{b}$, indicating a space charge-dominated regime. Space charge is a non-relativistic effect, it can be critical at low energies. Therefore, it is essential to account for space charge effects when simulating the transport of the beam from the MIST source to MAMBO.

The distribution of these particles and their associated electric fields can vary significantly, particularly in high-intensity beams, leading to nonlinear effects that are challenging to model with simple equations. Consequently, numerical simulations and computational models are typically required to accurately describe the dynamic behavior of the electron beam.

It is important to note that space charge effects cannot be accurately described using purely analytical methods, except in specific cases such as klystrons, due to the complex interactions between charged particles within a beam.

2.8 Hill's equations with space charge effects

A space charge is a non-relativistic effect that can become critical at low energies, making its consideration essential. Consequently, the traditional Hill's equations (see Eqs. (2.16), (2.17)) must be modified by introducing an additional term K_{sc}, which accounts for the influence of space charge forces. Based on the theoretical framework presented in [33], the Hill's equations for the x and y directions can be derived as follows:

$$\frac{d^2x}{ds^2} + \kappa_x(s)x - \frac{\varepsilon_x^2}{\sigma_x^3} - \frac{K_{\mathrm{sc}}}{2(\sigma_x + \sigma_y)} = 0 \tag{2.62}$$

$$\frac{d^2y}{ds^2} + \kappa_y(s)y - \frac{\varepsilon_y^2}{\sigma_y^3} - \frac{K_{\mathrm{sc}}}{2(\sigma_x + \sigma_y)} = 0 \tag{2.63}$$

Where $\frac{d^2x}{ds^2}$ and $\frac{d^2y}{ds^2}$ is second derivatives of the particle's transverse displacement, representing acceleration in the transverse plane, $\kappa_x(s)$ and $\kappa_y(s)$ is focusing functions, $\frac{\varepsilon_x^2}{\sigma_x^3}$ and $\frac{\varepsilon_y^2}{\sigma_y^3}$ - emittance terms, K_{sc} - the space charge parameter.

This space charge parameter defined as:

$$K_{\mathrm{sc}} = \frac{q_e I_{\mathrm{b}}}{2\pi\epsilon_0 E_0 c\gamma^3\beta^3} \tag{2.64}$$

Where, I_{b} - Average beam current, E_0 - rest mass energy of the particle, ϵ_0 - permittivity of free space, c - speed of light, γ - lorentz factor, β - normalized velocity, $\beta = \frac{v}{c}$, σ_x and σ_y - RMS beam sizes in the transverse x and y directions.

These modified Hill's equations illustrate how space charge effects can influence the motion of particles. By adding the space charge term, these equations account for the repulsive forces that arise due to the collective behavior of the charged particles, which can lead to beam expansion and emittance growth, especially at low energies or high beam densities.

These equations were derived for a dc beam, but they are also valid for a bunched beam in the low-energy beam transport section if the bunch length is in the same order of magnitude as the accelerating structure of the electron gun.

Chapter 3

Bending magnet design

The MIST source and the Mott polarimeter will be positioned at the same height above the main MESA injector beamline. Therefore, as previously mentioned, a parallel-shifting beamline was developed to transport the high-charged electron beam from the electron source MIST to the entrance of first acceleration section of MAMBO on the main beamline of MESA accelerator. The important part of lattice design of this beamline includes a so-called bending arc, such lattice generally consists of two bending magnets and focusing elements (for example quadrupole lenses) between them. This chapter covers the design of these two bending magnets and considers the results of their measurements.

3.1 Introduction

As mentioned above, the main aim ot the second injection beamline of MESA is transporting high charged electron bunches from the electron source MIST to the entrance of the first acceleration section. Because the electron beam has low energy ($E = 100$ keV, $\beta = 0.554$, $\gamma = 1.196$) the space charge effects are critical. Hence, it is very important to choose correct design for bending magnets. Moreover, these magnets (B1/B2) (See Figure3.2) should be operated in 3 different modes (see fig. 3.1).

- Transport the beam from STEAM to DSMP.
- Transport the MIST beam to the first MAMBO acceleration section and compress it using a buncher, which will be installed after the second dipole magnet.
- Transport of the STEAM beam to the first accelerating section of MAMBO.

For example, Fig. 3.2 illustrates the different operating modes of the second bending magnet (B2). Left: STEAM to MAMBO – standard operation for experiments with B2 turned off. Middle: STEAM to the polarimeter – used for spin polarization measurements. Right: MIST to the experiment – utilized for high beam currents or bunch charges. Red arrows indicate the electron beam's direction. It should be noted that the magnetic field direction is the same for the two deflections. So, in principle, it is possible to operate MIST for injection and simultaneously measure the spin polarization with STEAM and the DSMP. Such a systems offers expansion potential.

An important part of the design of such a beamline is the correct choice of bending magnets, which play a pivotal role in transporting the electron beams through the designed paths.

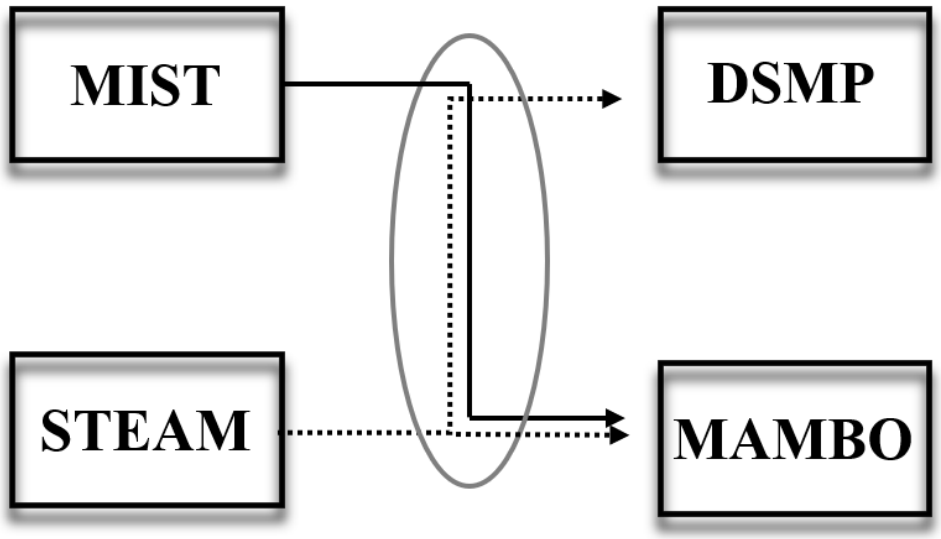

Figure 3.1: The diagram shows the layout of the MIST and STEAM electron sources, the Mott polarimeter, and the entrance to the first acceleration section of MAMBO. Arrows indicate both operating modes of the transport beamline.

C-type magnets provide easier access to the beam, making diagnostics and adjustments more convenient. Their compact structure is beneficial for setups with space constraints. However, C-type magnets generate a less homogeneous field and tend to produce stronger fringe fields near the edges. Moreover, this type of magnet could theoretically be made movable. Since the reproducibility of the magnetic field is extremely important when using the straight through passage of the beam ("third" operation mode) moving it away may become an interesting feature. (See section 3.6).

H-type magnets, on the other hand, offer better mechanical stability due to their closed design, ensuring more uniform magnetic fields. They also generate lower stray fields, reducing interference with surrounding equipment. However, their heavier and bulkier construction makes integration into compact beamlines more challenging, and their closed structure limits beam access, making diagnostics and adjustments more difficult and such a magnet cannot be made movable.

That's why, two types of dipole magnets were considered (see equation 2.16), so-called "C" and "H" type and with two different bending radius with 100 mm and 50 mm. The choice between C-type and H-type bending magnets depends on the specific requirements of the beamline, as each type has distinct advantages and limitations. In the case of a transport beamline, where the beam passes through only once, unlike in storage rings, a C-type magnet with sufficient field quality is suitable for effective beam steering. Therefore, the C-type magnet was selected.

A bending radius of 100 mm was identified as a good compromise between field quality and compactness, moreover, if necessary, such bending magnet will be easier to operate with an electron beam of 200 keV.

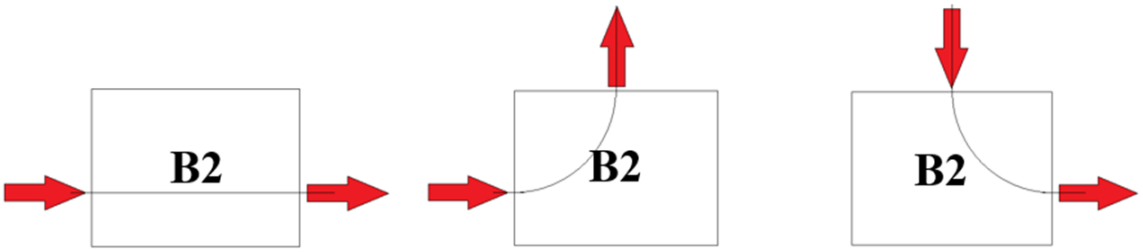

Figure 3.2: Different operation modes for the designed dipole magnet B2. Left: STEAM to MAMBO – normal operation for experiment with B2 switched off. Middle: STEAM to polarimeter – measurement of spin-polarization. Right: MIST to experiment with high beam currents or bunch charges. Red arrows show the direction of motion of the electron beam.

3.2 Bending magnets design

The magnetic rigidity is defined as [?]

$$B\rho[T * m] = \frac{p}{q} \tag{3.1}$$

where ρ is the bending radius, p is the momentum of the particles, q is the charge of the particles, and B is the magnetic field strength. For 100 keV ($\gamma = 1.2, \beta = 0.55$) electron beam $B\rho = 1.1173 * 10^{-3}(T * m)$.

Therefore, in order to bend such electron beam by 90° with bending radius $\rho = 100$ mm a magnetic field of about 12 mT is required, in case if $\rho = 50$ mm, the required magnetic field will be proportionally increased up to 24 mT.

For magnetostatic problems, the time derivative of magnetic field is zero, $\frac{\partial \mathbf{B}}{\partial t} = 0$, and Maxwell's equations have the following form:

$$\nabla \times \mathbf{H} = \mathbf{J}, \tag{3.2}$$

$$\nabla \cdot \mathbf{B} = 0, \tag{3.3}$$

$$\mathbf{B} = \mu(\mathbf{H})\mathbf{H} = \mu_0(\mathbf{H} + \mathbf{M}). \tag{3.4}$$

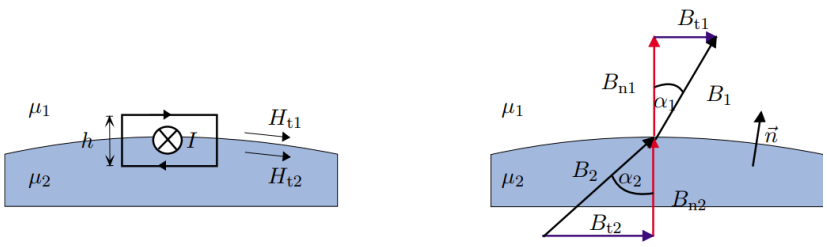

Figure 3.3: Geometry of the bend.

If we apply Ampere's law in the integral form:

$$\oint \mathbf{H} \cdot d\mathbf{s} = \int_A \mathbf{J} \cdot d\mathbf{A}, \tag{3.5}$$

to the loop displayed in Figure 3.3 (left), and let $h \to 0$, then the enclosed current is zero, as in an infinitesimal small rectangle there cannot be a current flow. Therefore:

$$H_{t1} = H_{t2}, \tag{3.6}$$

From the interface conditions for permeable media, we have:

$$\hat{n} \times (\mathbf{H}_1 - \mathbf{H}_2) = 0 \tag{3.7}$$

Since $\oint \mathbf{B} \cdot d\mathbf{A} = 0$ at the interface, we get:

$$B_{n1} = B_{n2}, \tag{3.8}$$

i.e.,

$$\hat{n} \cdot (\mathbf{B}_1 - \mathbf{B}_2) = 0. \tag{3.9}$$

Now, considering the angles α_1 and α_2:

$$\frac{\tan \alpha_1}{\tan \alpha_2} = \frac{\frac{B_{t1}}{B_{n1}}}{\frac{B_{t2}}{B_{n2}}} = \frac{\mu_1 H_{t1}}{\mu_2 H_{t2}} = \frac{\mu_1}{\mu_2}. \tag{3.10}$$

For $\mu_2 \gg \mu_1$, it follows that $\tan \alpha_1 \gg \tan \alpha_2$. Therefore, for all angles $\pi/2 > \alpha_2 > \alpha_2 > 0$, we get $\tan \alpha_1 \approx 0$. The field exits vertically from a highly permeable medium into a medium with low permeability.

Consider the magnetic (dipole) circuit shown in Figure 3.4. With Ampere's law in the integral form:

$$\oint \mathbf{H} \cdot d\mathbf{s} = \int_A \mathbf{J} \cdot d\mathbf{A}, \tag{3.11}$$

we can write:

$$H_{\text{iron}} s_{\text{iron}} + H_{\text{gap}} s_{\text{gap}} = NI, \tag{3.12}$$

$$\frac{1}{\mu_0 \mu_r} B_{\text{iron}} s_{\text{iron}} + \frac{1}{\mu_0} B_{\text{gap}} s_{\text{gap}} = NI, \tag{3.13}$$

With $\mu_r \gg 1$, we get the easy relation:

$$B_{\text{gap}} = \frac{\mu_0 NI}{s_{\text{gap}}}. \tag{3.14}$$

In bending magnets design, it is important to consider magnetic field strength and bending radius, magnet size, power consumption, and cooling requirements. The choice of magnet material will depend on factors such as the required magnetic field strength, stability, and cost. In our case we used pure iron ("Armco"), with lower remanence than conventional steel.

The magnet structure should be designed to provide a uniform magnetic field along the bending radius. This may involve shaping the magnet poles and optimizing the magnet geometry to achieve the desired field distribution.

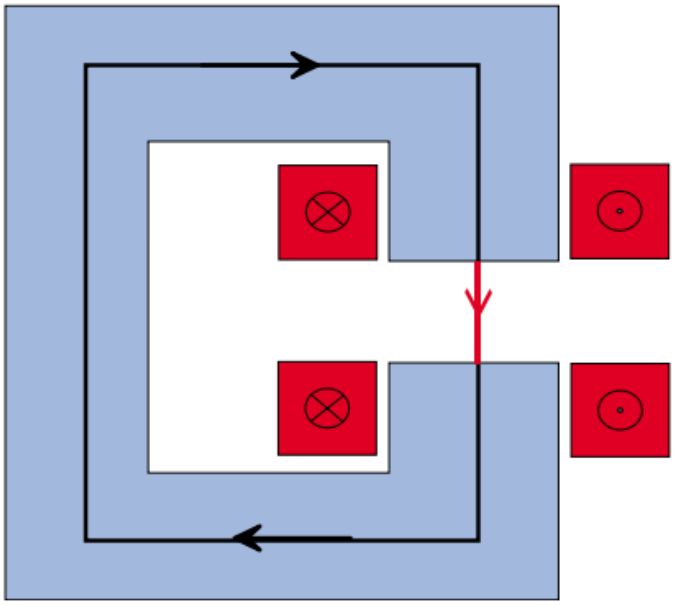

Figure 3.4: Circulation of magnetic field in the C-type bending magnet.

Let us estimate the magnetic field for a sector bending magnet with a bending radius of 100 mm and a bending angle of $\pi/2$, with 200 wires in a a both coils using the corresponding the Eq. 3.14 for the magnetic field in the gap of a dipole magnet:

$$B_{\text{gap}} = \frac{4\pi \times 10^{-7} \cdot 200 \cdot 2.07}{0.046} \approx \ 11.3 \text{ mT}.$$

where $\mu_0 = 4\pi \times 10^{-7}$ H/m is the permeability of free space, $N = 200$ is the number of wire turns, $I = 2.07$ A is the current, and $s_{\text{gap}} = 0.046$ m is the width of the magnetic gap. The magnetic field in the gap is approximately 11.3 mT.

The magnet was designed using high-purity ARMCO iron due to its minimal hysteresis losses. ARMCO iron is a commercially pure, low-carbon soft magnetic material with high magnetic permeability and minimal hysteresis. ARMCO iron has high purity (typically $> 99.85\%$ Fe) and a relative permeability typically in the range of $\mu_r \sim 4000$–5000.

If we use a more precise Eq. 3.13 with $s_{\text{iron}} = 0.404$ m, and $\mu_0 = 4\pi \times 10^{-7}$ H/m, we compute the magnetic field in the gap for two cases:

$$B_{\mu_r=5000} = \frac{NI}{\frac{s_{\text{iron}}}{\mu_0\mu_r} + \frac{s_{\text{gap}}}{\mu_0}} = \frac{414}{64.29 + 36606.59} \approx 11.29 \text{ mT},$$

$$B_{\mu_r\to\infty} = \frac{\mu_0 NI}{s_{\text{gap}}} = \frac{5.2025 \times 10^{-4}}{0.046} \approx 11.31 \text{ mT}.$$

The difference between the two results is negligible due to the dominant contribution of the air gap's magnetic reluctance.

By choosing the required magnetic field in the bending magnet, it is possible to accurately determine the necessary number of wire turns and the operating current in the magnet, while also considering the distance between the poles.

Given that the height of the vacuum chamber is 40 mm, the distance between the poles was set to 46 mm, with the magnetic field in the bending magnet configured at 12 mT. As a result, a current of 2.1 Amperes was chosen for the wire, and the coil was configured with 105 turns per pole.

The parameters of the bending magnet have been evaluated and are summarized in the Table 3.1.

Table 3.1: Specifications od designed bending magnet

Parameter	**Value**
Gap	46 mm
Bending radius (ρ_b)	92.5 mm
Bending angle (α_b)	90°
Number of wire turns	105
Wire diameter	1.25 mm
Coil size	13.5 x 14 mm
Magnetic field (B_b)	$\approx$ 12 mT
Current in coil (I_{wind})	$\approx$ 2.1 A
Current density in wire (j_{wind})	$\approx$ 1.77 A/mm^2
Resistance of winding (R_{wind})	$\approx$ 2.3 Ohm
Power (P_b)	$\approx$ 10.97 W
Voltage (U_b)	$\approx$ 5.05 V

3.3 CST model of bending magnets

CST Studio Suite [26] is a comprehensive simulation software tool used for designing and analyzing electromagnetic components and systems. It enables the simulation of a wide range of electromagnetic effects, including high-frequency and low-frequency behavior, thermal and mechanical analysis, and particle tracking.

CST Studio Suite includes several solvers, one of which is specifically designed for magnetostatic simulations. This magnetostatic solver allows for the accurate modeling and analysis of static magnetic fields, making it ideal for designing different types of magnets [26].

Using the parameters provided above in Table [3.1], two models of dipole magnets were considered for the separation beamline. One design is known as the C-shaped magnet, while the other is referred to as the H-shaped bending magnet (see Figure 3.5).

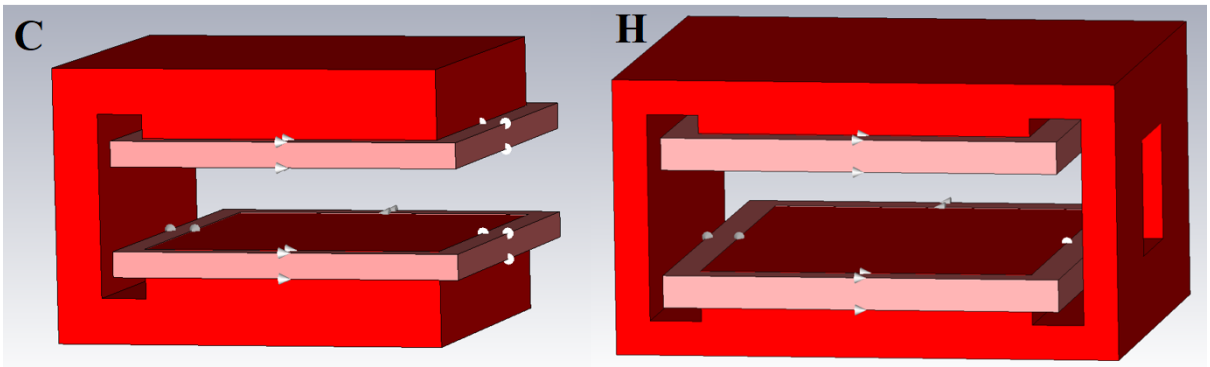

Figure 3.5: CST model of C-shape (left) and H-shape (right) bending magnets.

The key advantage of H-shaped bending magnets is their symmetrical, horizontal structure, which provides superior magnetic field uniformity and control. This makes them ideal for applications requiring precise beam steering. In contrast, C-shaped bending magnets have an open design that allows for easier access to the magnetic gap, simplifying installation and maintenance, but at the cost of slightly reduced field uniformity.

One of the most important parameters determining the quality of a bending magnet's magnetic field is the good field region. The good field region refers to the area within the magnetic field where the field strength and uniformity are maintained with high precision. This region is crucial for ensuring that charged particles experience consistent magnetic forces, allowing for a stable and predictable trajectory. We define the good field region as the area in which the relative deviation of the magnetic field satisfies $\delta B_z/B_{z0} < 10^{-3}$, where B_{z0} denotes the magnetic field on the equilibrium orbit and δB_z is its local deviation see fig 3.6. However, this parameter is particularly critical in circular accelerators, where the beam passes through the bending magnet multiple times. In linear accelerators, this requirement is less stringent.

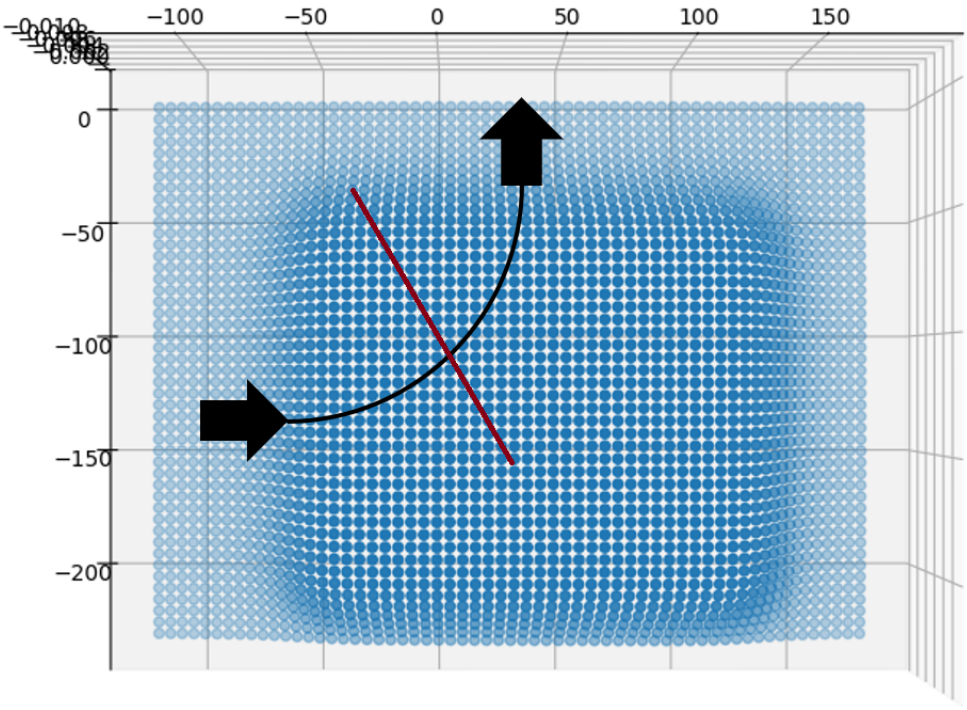

Figure 3.6: The measured magnetic field of the dipole magnet is shown. The red line indicates the path along which the magnetic field distribution is plotted to evaluate the good field region. The relative position $x = -120$ mm corresponds to the design equilibrium orbit of the beam in the bending magnet (i.e., the coordinates at which the red line intersects the orbit).

Figure 3.7 presents CST simulation results of the good field region at the center of the beam orbit in the dipole magnet, perpendicular to the beam path, for both types of bending magnets.

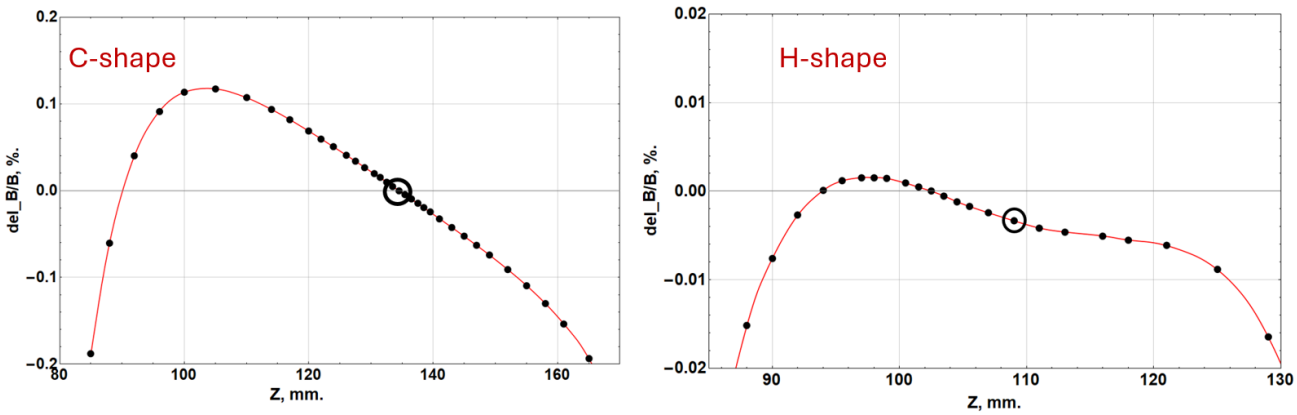

Figure 3.7: CST simulation results of the good field region for C-shape(left) and H-shape(right) bending magnets. Black circle - position of the beam.

Although CST simulation results indicate that the H-shaped dipole magnet provides a more uniform magnetic field, the C-shaped dipole offers sufficient field uniformity for practical applications. Moreover, due to the effect of remanence, turning the bending magnet on and off causes slight variations in the set magnetic field each time, making it impossible to immediately return to the exact operating conditions. To address this issue, a solution was proposed to make the lower dipole magnet (B2) movable on a vertical platform while keeping it continuously powered.

Since the H-shaped bending magnet cannot be made movable, the C-shaped magnet was chosen instead. Figure 3.8 shows the process of measuring the magnetic field in the manufactured C-shaped bending magnet.

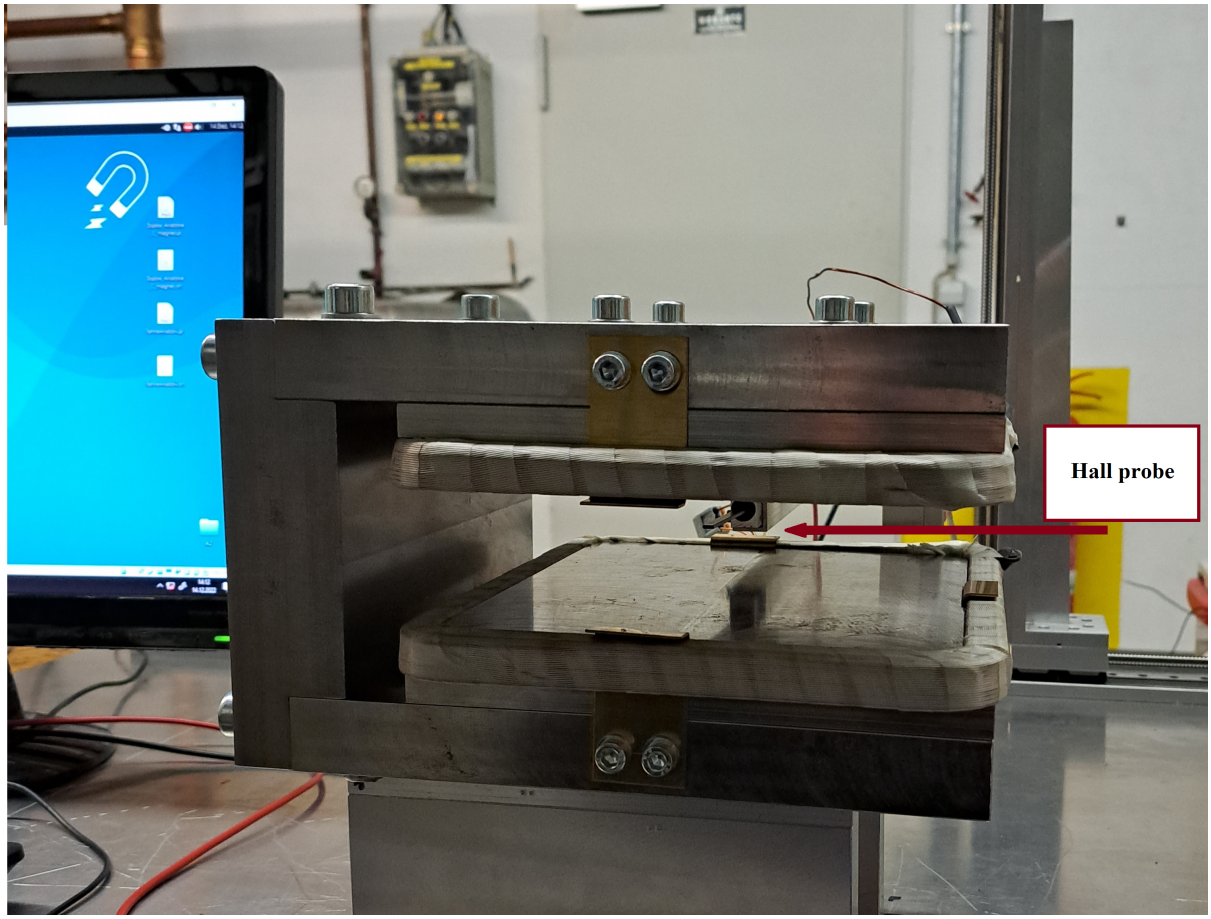

Figure 3.8: Process of measuring the magnetic field in the manufactured C-shape bending magnet.

3.4 Vacuum chamber for bending magnets

The designed bending magnet requires specialized vacuum chambers that facilitate the transport of the electron beam either from the STEAM source to the MAMBO acceleration section or by bending the beam at a 90° angle to direct it towards the double-scattering Mott polarimeter. Therefore, the vacuum chamber must allow the beam to pass through at least three different paths.

Furthermore, there is no beam position diagnostic system along the beamline between the MIST electron source and the main MESA beamline, which could make beam alignment more challenging. I have designed a more efficient use of space was proposed by integrating the diagnostic system directly into the vacuum chambers using movable scintillator screens and a CCTV system. Figure 3.9 shows the layout of such a vacuum chamber.

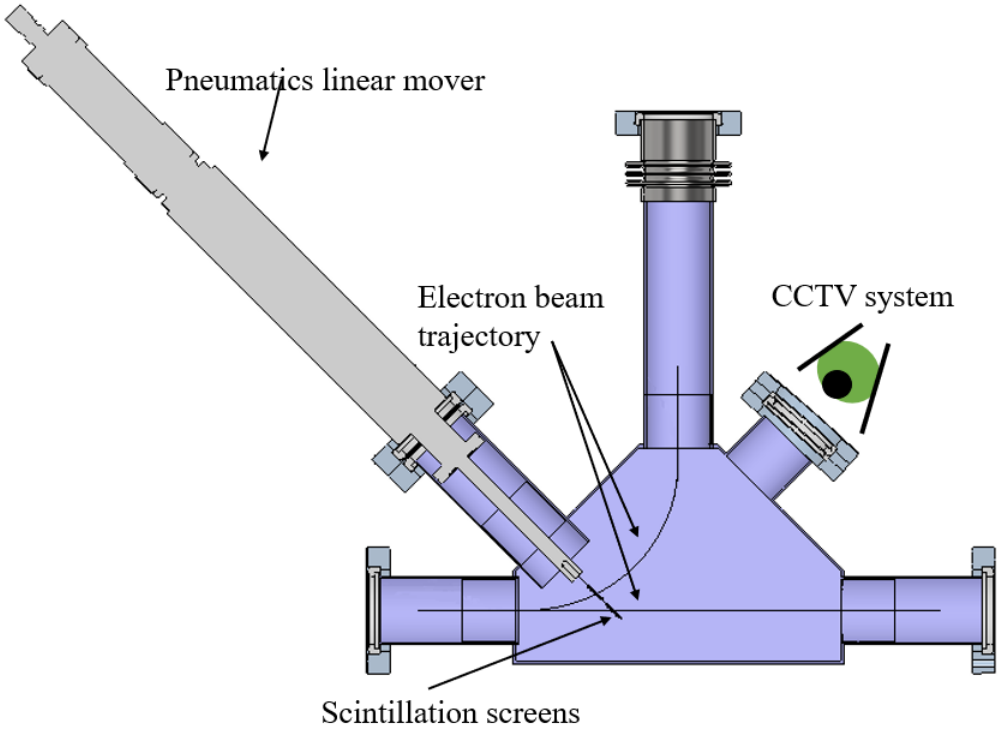

Figure 3.9: Model of vacuum chamber for dipole magnet with beam position diagnostic system. CAD design by Thorsten Feldmann. The scintillation screens are transparent, which offers to view of the beam position from the opposite side.

Polished YAG crystals were selected as scintillator screens due to their excellent optical properties and high efficiency in detecting electron beams. The crystals have a diameter of 15 mm and a thickness of 0.15 mm. Figure 3.10 shows the YAG:Ce scintillator crystals that have already been purchased.

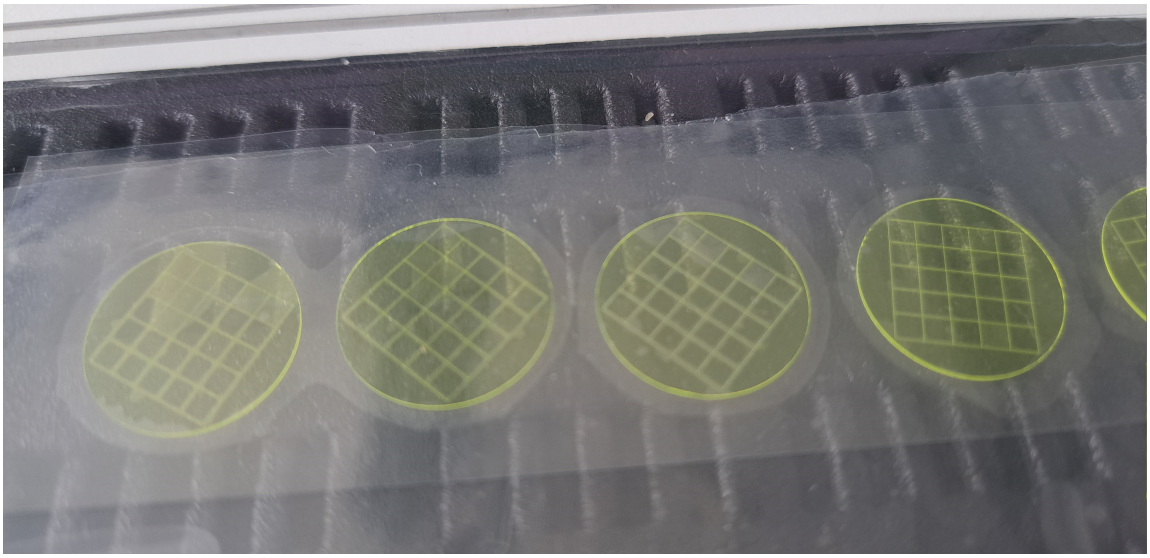

Figure 3.10: YAG:Ce scintillator crystals.

Cerium-doped Yttrium Aluminum Garnet (YAG:Ce) is a highly efficient scintilla-

tor known for its excellent mechanical strength, chemical stability, and non-hygroscopic nature [28]. It exhibits high light yield, fast decay time (70 ns), and good thermal conductivity, making it suitable for applications requiring durability and stable performance. The emission spectrum peaks at 550 nm, aligning well with the sensitivity range of common photo-detectors. The main parameters of the purchased YAG:Ce scintillator are listed in Table 3.2.

Table 3.2: Parameters of the YAG:Ce scintillation screen.

Parameter	**Value**
Scintillator material	YAG:Ce (Yttrium Aluminum Garnet doped with Cerium)
Screen diameter	15 mm
YAG:Ce thickness	150 nm
Aluminium coating thickness	20 nm
Peak emission wavelength	∼530 nm (green)
Decay time	∼70 ns
Optical transparency	High (allows beam spot imaging from both sides)
Photon yield	∼8,000 photons/MeV (∼8 photons/keV)

A linear feedthrough MLSi 40-50-S2 was selected as the driving system for moving the scintillator screen. It is equipped with a two-phase stepper motor from Oriental Motor (model PKP268MU20B-L) and has a stroke length of 100 mm [29]. Notably, similar linear movers have already been ordered by our department. See Figure 3.11.

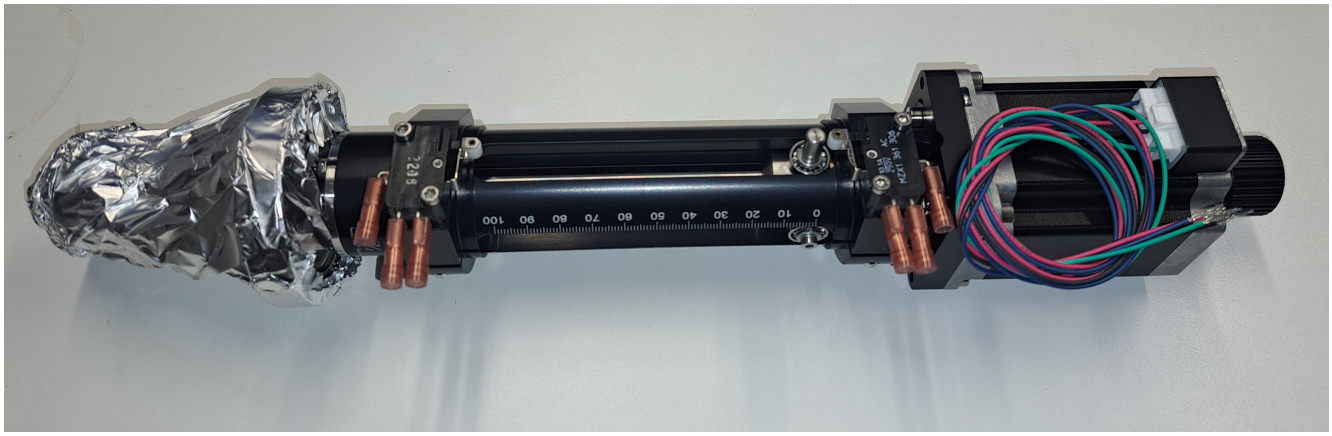

Figure 3.11: linear feedthrough MLSi 40-50-S2.

Figure 3.12 shows the vacuum chamber for the bending magnets, manufactured in the KPH workshop, with flanges already welded in place.

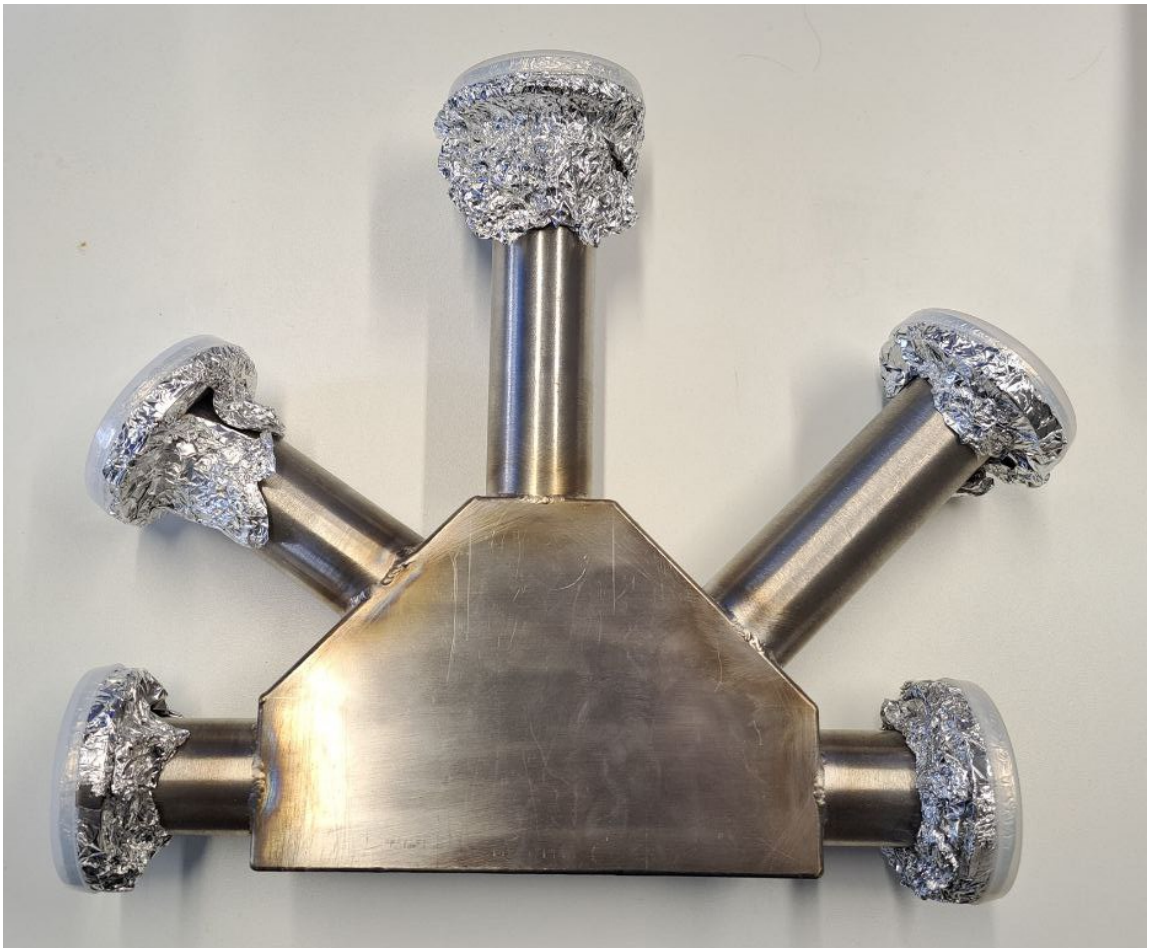

Figure 3.12: Appearance of the manufactured vacuum chamber for the C-shape bending magnets.

3.5 Magnetic field measurements

After the fabrication of the bending magnets, comprehensive magnetic field measurements were performed using two types of sensors: Hall probes and flux-gate magnetometers.

A Hall probe operates based on the Hall effect, utilizing a thin semiconductor through which a current flows. When exposed to a perpendicular magnetic field, the charge carriers experience a Lorentz force, leading to a measurable Hall voltage orthogonal to both the current and the magnetic field. This voltage is directly proportional to the magnetic field's strength.

In contrast, a flux-gate magnetometer employs a core of highly permeable material wrapped with two coils: a drive coil and a sense coil. An alternating current in the drive coil magnetically saturates the core in alternating directions. An external magnetic field influences the core's magnetization, inducing a signal in the sense coil proportional to the external field's strength and direction [30].

For the 3D mapping of the bending magnet's magnetic field, the Hall probe was utilized. The fluxgate sensor is used to detect the very small fields after the degaussing of the magnet(see below), in that case the sensitivity of the hall probe is not sufficient. Figure 3.13 illustrates the test stand during these measurements. These methodologies ensured precise characterization of the magnetic fields.

Figure 3.13: 3D magnetic field measurement with the Hall probe.

Figure 3.13 illustrates the magnetic field distribution in the horizontal plane at the median plane of the bending magnet. To construct a comprehensive three-dimensional map of the magnetic field, measurements were systematically conducted with a spatial resolution of 5 mm in the horizontal plane, encompassing an area of 300 mm by 230 mm, resulting in a total of 2,867 data points per plane. These measurements were performed at four distinct vertical positions relative to the magnet's central plane, with each vertical increment set at 4 mm.

Figure 3.14 illustrates the variation of the magnetic field within the bending magnet along a specified direction (see red line in Fig 3.14) at multiple vertical positions. This analysis provides insight into the magnetic field's spatial distribution and its dependence on vertical displacement within the magnet.

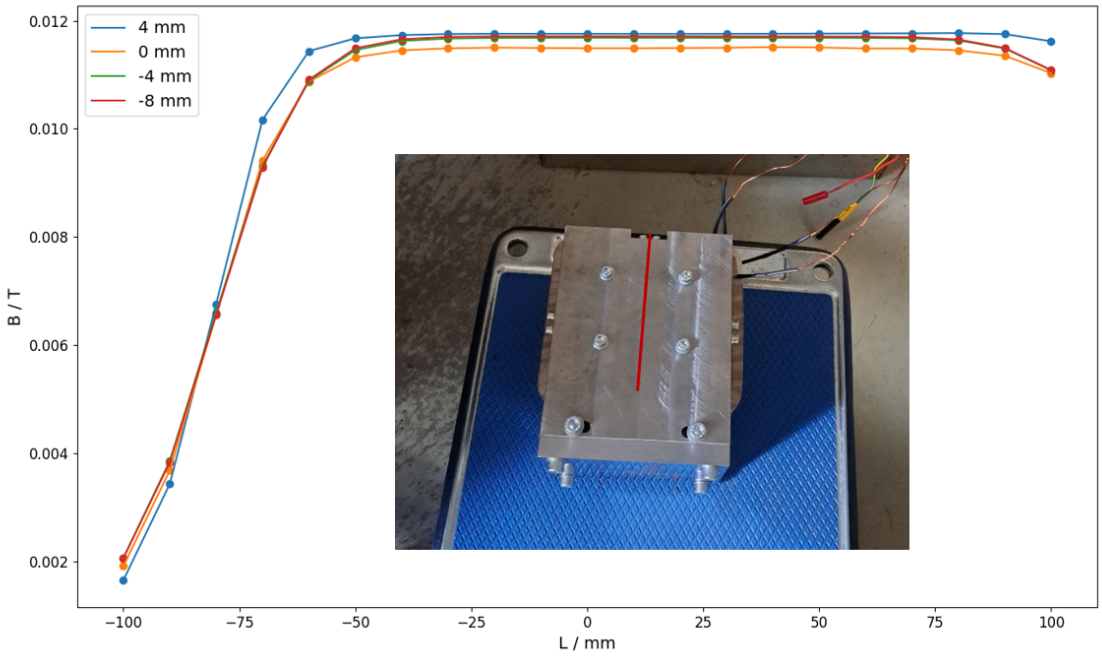

Figure 3.14: Magnetic 2D field distribution in the center of dipole magnet.

As previously discussed, the good field region is a critical parameter that characterizes the uniformity of the magnetic field within a bending magnet. The GFR is typically defined as the area where the magnetic field deviation remains within acceptable limits, ensuring optimal beam dynamics. In Figure 3.15, we present a comparative analysis of the GFR at the magnet's center, perpendicular to the beam trajectory, for both the empirically measured and CST Studio Suite-simulated magnetic fields. This measurements has been done along the same position and indicated in fig. 3.14 with red line.

The relatively small deviations could result from instance manufacturing/assembly process. One could expect that the magnet is mechanically not very stiff and that the gap therefore may change towards the outer part, which could lead to such a behavior.

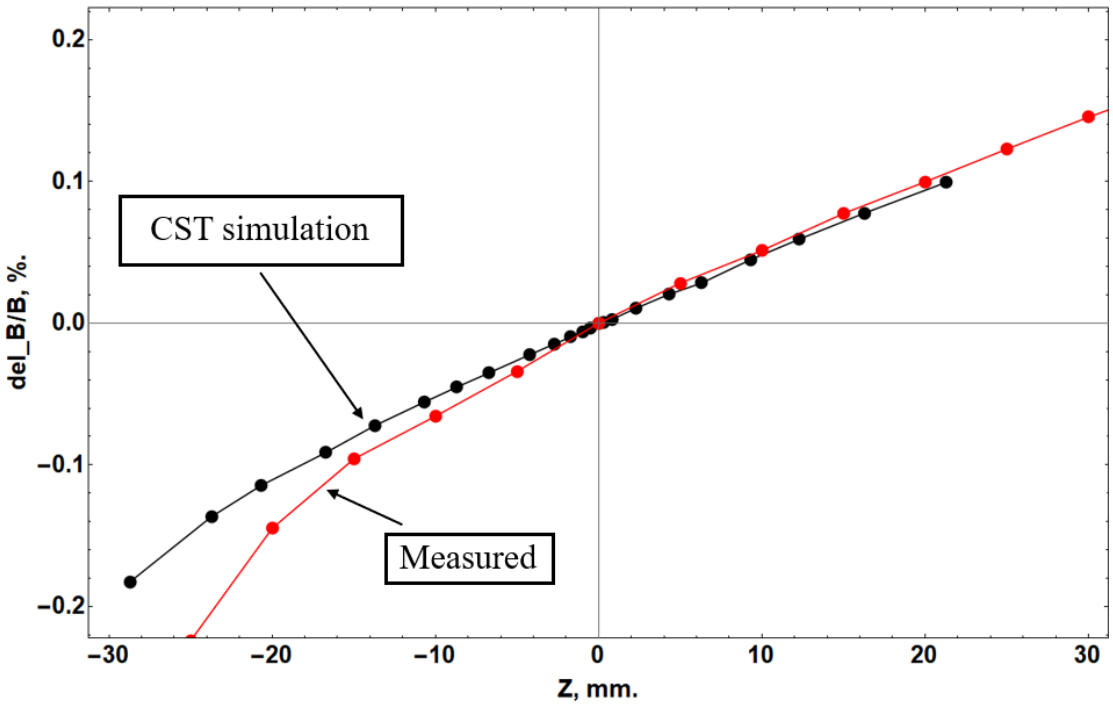

Figure 3.15: The good field region at the center of the magnet, perpendicular to the beam path.

Figure 3.16 illustrates the vertical variation of the magnetic field at the central axis of the bending magnet, comparing empirical measurements with computational simulations conducted using CST Studio Suite. This comparative analysis provides insights into the magnetic field's dependence on vertical position within the magnet and evaluates the accuracy of the simulation model in replicating the observed field variations.

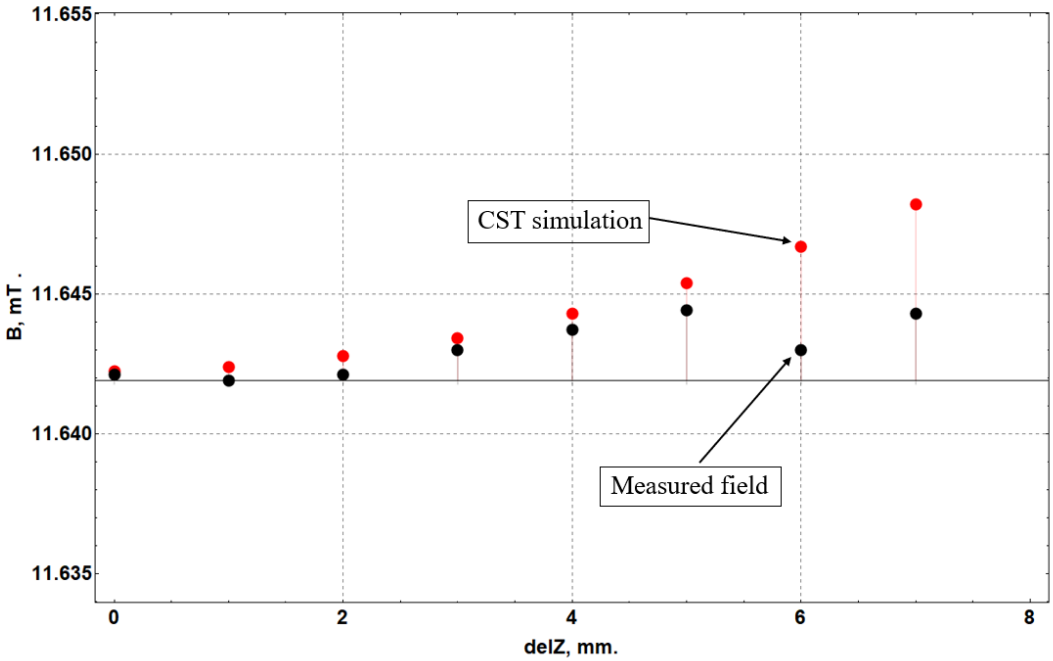

Figure 3.16: The good field region at the center of the magnet, perpendicular to the beam path.

As was shown in chapter and taking into account main parameters of electron beam $m_e c^2 = 0.511$ MeV and kinetic energy of electron beam $T = 100$ keV, then momentum is $p = 3.3496 \times 10^{-4}$ GeV/c, and the magnetic rigidity is $B\rho = 1.1173 \times 10^{-3}$ T $\cdot$ m. To find the one–dimensional fit in the mid–plane from this measured along the median plane ($y = 0$) the measured relative field deviation is represented by a quadratic expansion in the horizontal coordinate x (in mm):

$$\frac{\Delta B}{B_0}(x) = c_0 + c_1 x + c_2 x^2, \tag{3.15}$$

with fitted coefficients

$$c_0 = 8.966 \times 10^{-4}, \qquad c_1 = 7.564 \times 10^{-5}\ \text{mm}^{-1}, \qquad c_2 = -7.078 \times 10^{-7}\ \text{mm}^{-2}. \tag{3.16}$$

Assuming negligible skew terms, the normal (non–skew) two–dimensional field components consistent with the 1D fit are

$$\frac{B_y(x,y)}{B_0} \approx c_0 + c_1 x + c_2(x^2 - y^2), \tag{3.17}$$

$$\frac{B_x(x,y)}{B_0} \approx c_1 y + 2c_2 xy. \tag{3.18}$$

Here c_0 is an uniform dipole offset (0.08966% of B_0); the terms proportional to c_1 form the normal quadrupole;

The second order focusing term is proportional to c_2 the normal sextupole, which vanishes along $x = \pm y$ and changes sign across these diagonals. Moreover, the normal multipole term in the mid–plane expansion reads

$$B_y(x,0) = -\lambda_1 - 2\lambda_2 x - 3\lambda_3 x^2 - \cdots. \tag{3.19}$$

Identifying with the polynomial above gives

$$\frac{\lambda_1}{B_0} = -c_0, \qquad \frac{\lambda_2}{B_0} = -\frac{c_1}{2}, \tag{3.20}$$

$$\frac{\lambda_3}{B_0} = -\frac{c_2}{3}, \tag{3.21}$$

hence

$$\frac{\lambda_1}{B_0} = -8.966{\times}10^{-4}, \qquad \frac{\lambda_2}{B_0} = -3.782{\times}10^{-5}\,\mathrm{mm}^{-1} = -3.782{\times}10^{-2}\,\mathrm{m}^{-1}, \qquad \frac{\lambda_3}{B_0} = 2.359{\times}10^{-7}\,\mathrm{mm}^{-2} \tag{3.22}$$

If we try to found more higher (octupole) term, an octupole contribution is present, the normal components

$$\frac{B_y}{B_0} \supset c_3(x^3 - 3xy^2), \qquad \frac{B_x}{B_0} \supset c_3(3x^2y - y^3), \tag{3.23}$$

with the mapping

$$\frac{\lambda_4}{B_0} = -\frac{c_3}{4}. \tag{3.24}$$

Using the residual level of the quadratic fit over $|x| \leq 30$ mm as a conservative indicator gives the bounds

$$|c_3| \leq 1.44 \times 10^{-9}\ \mathrm{mm}^{-3} = 1.44\ \mathrm{m}^{-3}, \qquad \left|\frac{\lambda_4}{B_0}\right| \leq 0.36\ \mathrm{m}^{-3}. \tag{3.25}$$

if we try to calculate transport normalized strengths using $B\rho$ the normalized strengths are

$$k_1 = \frac{1}{B\rho}\left.\frac{\partial B_y}{\partial x}\right|_0 = \frac{B_0}{B\rho}\,c_1, \qquad k_2 = \frac{1}{2B\rho}\left.\frac{\partial^2 B_y}{\partial x^2}\right|_0 = \frac{B_0}{B\rho}\,c_2, \qquad k_3 = \frac{1}{6B\rho}\left.\frac{\partial^3 B_y}{\partial x^3}\right|_0 = \frac{B_0}{B\rho}\,c_3. \tag{3.26}$$

With $B\rho = 1.1173 \times 10^{-3}$ T $\cdot$ m (100 keV kinetic energy of electron beam) this yields

$$k_1 = \frac{0.07564}{1.1173 \times 10^{-3}}\,B_0 = 6.77{\times}10^{1}\,B_0\ [\mathrm{m}^{-1}], \qquad k_2 = \frac{-0.7078}{1.1173 \times 10^{-3}}\,B_0 = -6.33{\times}10^{2}\,B_0\ [\mathrm{m}^{-2}] \tag{3.27}$$

$$|k_3| \leq \frac{1.44}{1.1173 \times 10^{-3}}\,B_0 = 1.29 \times 10^{3}\,B_0\ [\mathrm{m}^{-3}], \tag{3.28}$$

where B_0 is in T.

Experiments have shown (see Chapter 6) dogleg provides very small emittance at low charges - an indication that the nonlinear contributions indeed do not matter.

3.6 Degaussing procedure

Remanence is the magnetization left behind in a ferromagnetic material after an external magnetic field is removed. This phenomenon occurs because the magnetic domains within the material, aligned by the external magnetic field, do not completely return to a random state even after the magnetizing factor is removed.

Residual magnetization is associated with energy barriers within the material that prevent complete demagnetization. It depends on the material's composition, crystal lattice structure, and domain boundary properties. Remanence is also determined by the magnitude and duration of the external magnetic field's application.

In bending magnets or alpha magnets a large residual magnetization is not desirable as it is an unwanted contamination, for example, a magnetization remaining in an bending magnet after the current in the coil is turned off. Where it is unwanted, it can be removed by degaussing.

When the accelerator is turned on, having repeatability of the magnetic field is very important in order to start operation without optimizing the focusing system. The main objective is to achieve the same magnetic field after switching on. In that case it may be valuable to indeed to degauss to have a well defined starting point for the magnetization. That's why, degaussing of bending magnets is an important process on such accelerator as MESA.

Figure 3.17 shows the results of measuring the remanence in the center of the produced C-shape bending magnet after it is turned off.

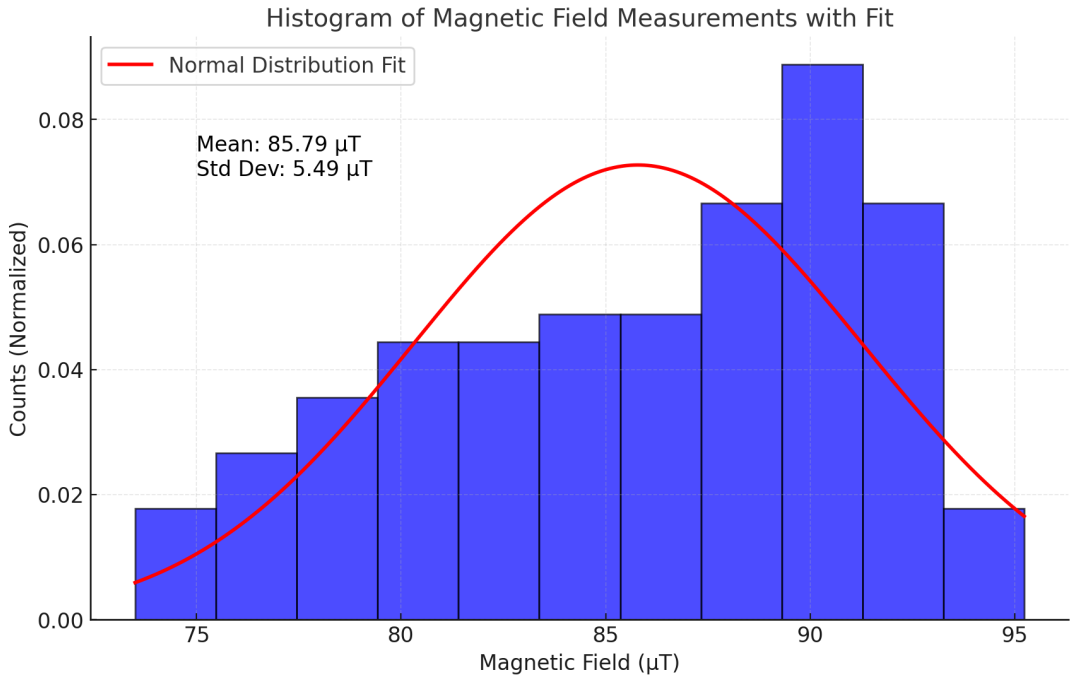

Figure 3.17: Measured magnetic field remanence in dipole magnet.

Figure 3.18 shows the scheme of setup used for the degaussing procedure. This setup consisted of the following elements:

1. Microcontroller Red Pitaya, to operate the current of the source (compact open-source measurement and control device based on a Zynq SoC)
2. DC power amplifier
3. Magnetic field sensor
4. Multimeter

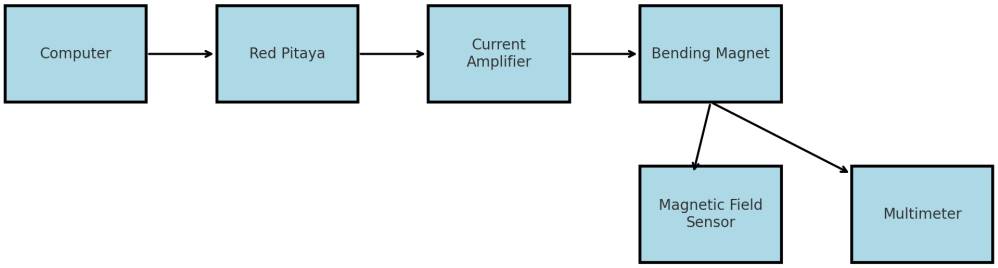

Figure 3.18: Schematic of the setup for the degaussing procedure.

Setup for measuring magnetic field remanence in a dipole magnet, including connections between the computer, Redpitya control unit, current amplifier, bending magnet, magnetic field sensor, and multimeter.

This connection system allows the use of a redpitaya (See Figure 3.19a) to set the desired current in the bending magnet and enables changing its polarity.

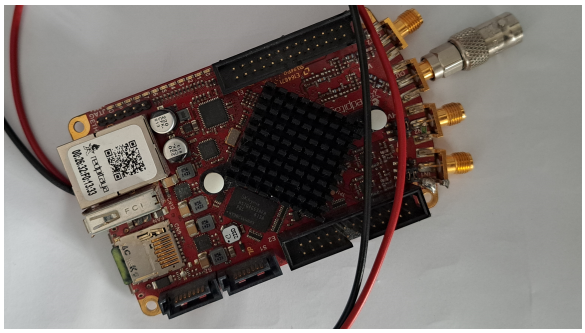

(a) Redpitaya used for signal processing and control degaussing procedure.

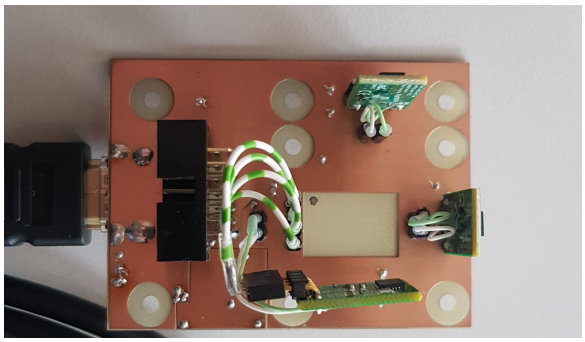

(b) Magnet sensor used for residual magnetic field measurement.

Figure 3.19: Measurement setup consisting of a Redpitaya for signal acquisition and a magnet sensor for residual magnetic field measurements.

For measurements of the residual magnetic field in the C-shaped bending magnet after the degaussing procedure, a specialized measuring device based on three flux-gate magnetic-field sensors DRV425 was used (see Figure 3.19b). The electronic board for this device was designed and produced at the KPH electronic workshop.

A special script was developed to execute the degaussing procedure. The script applied the operational current to the bending magnet for 5 seconds, then performed 30 iterations at one-second intervals, reducing the current by 15% per step while alternating the polarity. The degaussing algorithm is illustrated in Figure 3.20.

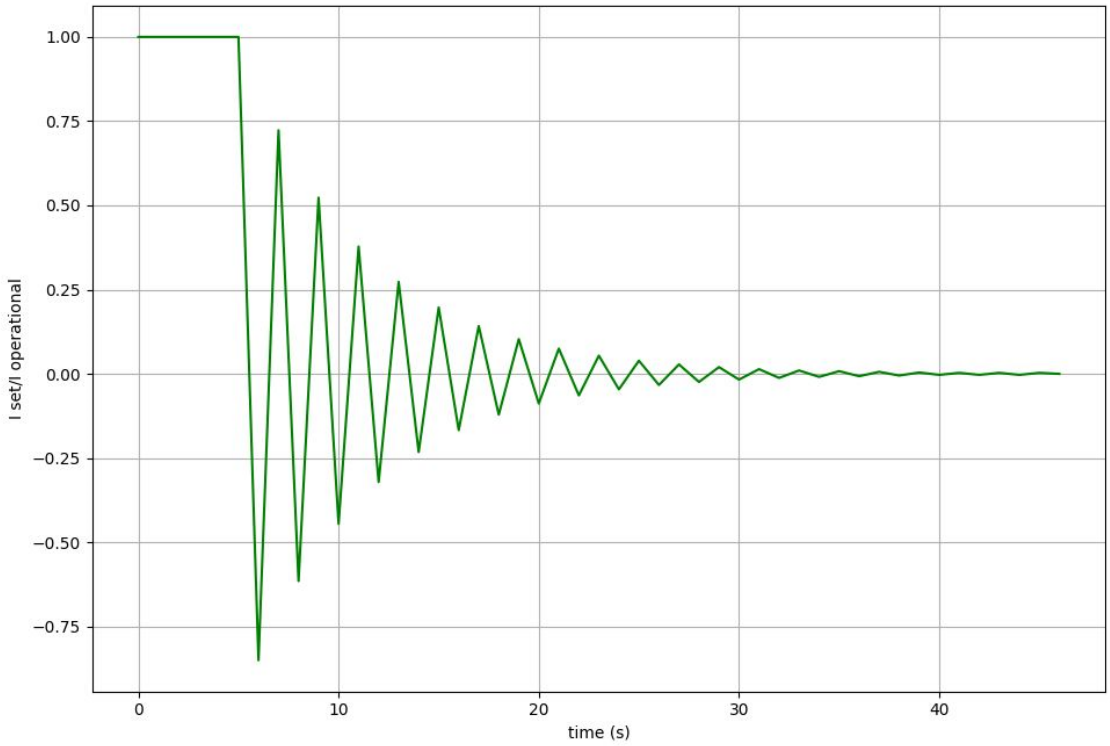

Figure 3.20: Degaussing algorithm.

Table 3.3: Magnetic field remanence after the degaussing procedure.

Projection	Mean [μT]	RMS [μT]
B_x	17.39	0.57
B_y	6.04	0.22
B_z	0.16	0.02

Table 3.3 presents the RMS values of the magnetic field measured at the center of the C-shaped bending magnet after the degaussing procedure. As seen from the table, one of the components always shows about 20 μT remaining after degaussing. This may be due to the Earth's magnetic field penetrating to the sensor's position. Since the magnet is not a closed box, its shielding effect may not be very strong, which could explain why the measured field is smaller, but not significantly smaller, than the Earth's field.

The magnetic-field deflection of 0.57 μ T will give about 0.1 $mrad$ of deflection. This is still considerable. Therefore, we may conclude that a solution with a moving magnet is perhaps more promising. Nevertheless, a scattering value of $0.1/mrad$ can be corrected easily (see Chapter 6).

Chapter 4

Linear model of the separation beamline

One of the main tasks of designing the transport channel is to select the optimal lattice for such beamline. Such a structure has to satisfy a number of requirements to ensure efficient electron beam transportation. This lattice must provide parallel shifting of the electron beam from electron source MIST to the main beamline of MESA. Moreover, the lattice of the channel should minimize quality loss and form the electron bunch for optimal injection into the first acceleration section of MAMBO.

In addition, the structure must allow to transport beam from the electron source STEAM to the polarimeter. This requires flexibility in adjusting the focusing elements.

Due to the limited free space in the tunnel, the design must be as compact as possible. This restriction limits the types of bending arc lattices that can be used.

Moreover, the dispersion function of the beamline outside the bending arc should be zero, provision that transverse displacement due to energy spread of the beam is eliminated, thus ensuring beam stability along the separation beamline.

Thus, when designing the optical structure of the separation beamline, it is necessary to balance the following requirements: ensuring parallel beam transfer, focusing flexibility, compactness of the design, absence of dispersion outside the bending arc, and symmetry. This will achieve high transportation efficiency and provide the required quality of the injected beam at the input to the main beamline.

4.1 Separation beamline specifications

As shown above, space charge strongly effect on beam dynamics of such a highly charged bunch (See Eq. 2.62 and Eq. 2.63). This requires to develop a beamline with consideration of space charge effects. Additionally, this beamline should allow to compress and transport the electron beam to the first acceleration section of MESA. Let's formulate the basic requirements for this transport channel:

1. Since the source is located above the main MESA beamline, transport channel should provide parallel shifting of electron beam. In other words, the lattice of the transport channel should include a bending arc.

The matter is that, as shown in the previous chapter, the transversal beam sizes are given by [**?**]:

$$\sigma_{x,y} = \sqrt{\beta_{x,y}\epsilon_{x,y} + (D_{x,y}\delta)^2},$$

where $\beta_{x,y}$ is the horizontal or vertical beta function, ϵ_x is the horizontal or vertical emittance, $D_{x,y}$ is the horizontal or vertical dispersion function, and δ is the RMS relative energy spread.

Thus, an increase in the dispersion function or energy spread will lead to a larger beam size. Moreover, elements such as a quadrupole, solenoid or buncher do not create dispersion function, but this elements can change he beam size itself. Therefore, if the dispersion function is not suppressed outside the bending arc, this can lead to an uncontrolled increase in it and, as a consequence, a significant increase in the beam size and significant losses at the vacuum chamber apertures.

Therefore, it is necessary to choose a suitable bending arc lattice with zero dispersion function outside the arc.

Such deflection system can be constructed using several standard schemes with two bending magnets (Dogleg, Double bend achromat). From the other side, it is also possible to use system of several alpha magnets, such magnets do not create dispersion. In case we choose to use a lattice with bending magnets, it is also necessary to design special bending magnets.

2. The beamline should support two distinct operation modes:

- Transport the beam from the STEAM source to the DSMP, to measure polarization of the electron bunch.
- Transport the MIST beam to the first acceleration section of MAMBO and compress the beam using a buncher installed after the second dipole magnet.

4.2 Bending arc schemes

That is why three types of bending magnets for the bending arc were considered.

- Double bend achromat
- 90° dogleg
- 4 alpha magnets

4.2.1 Dogleg

One of the main tasks of designing the transport channel is to select the optimal lattice of the bending arc. A lattice of a bending arc, usually referred to as a "dogleg" is a pair of equal and opposite strength dipole bends separated by a drift space with one or more quadrupoles in the center of arc. The term dogleg comes from the shape of the bending arcs remindful the leg of a dog with the bent knee.

The main function of dogleg is to move the beam to the side without changing the design trajectory direction of a beam.

Typically, dogleg lattice consists of two bending magnets and one or three quadrupole lenses placed at the center of the bending arc to form the beam and suppress the dispersion function in the deflection plane outside the arc. The layout of dogleg lattice is shown in Fig. 4.1.

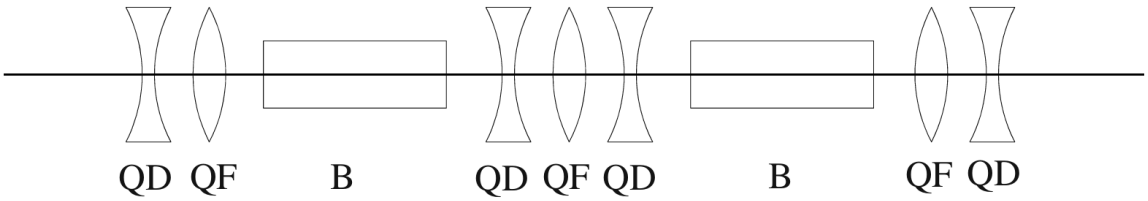

Figure 4.1: The layout of a dogleg lattice with a quadrupole triplet in the center of the arc. B - bending magnet, QD - horizontally defocusing quadrupole, QF - horizontally focusing quadrupole.

The full structure of this beamline includes a quadrupole doublet or triplet to provide the matching of the lattice functions into the first bending magnet. The central part of the lattice between the bending magnets could consist of one or more quadrupoles, and its function is to focus the dispersion function such that it is matched again to zero at the end of the second bending magnet. This bending arc lattice has the dispersion function, as shown in Figure 4.2.

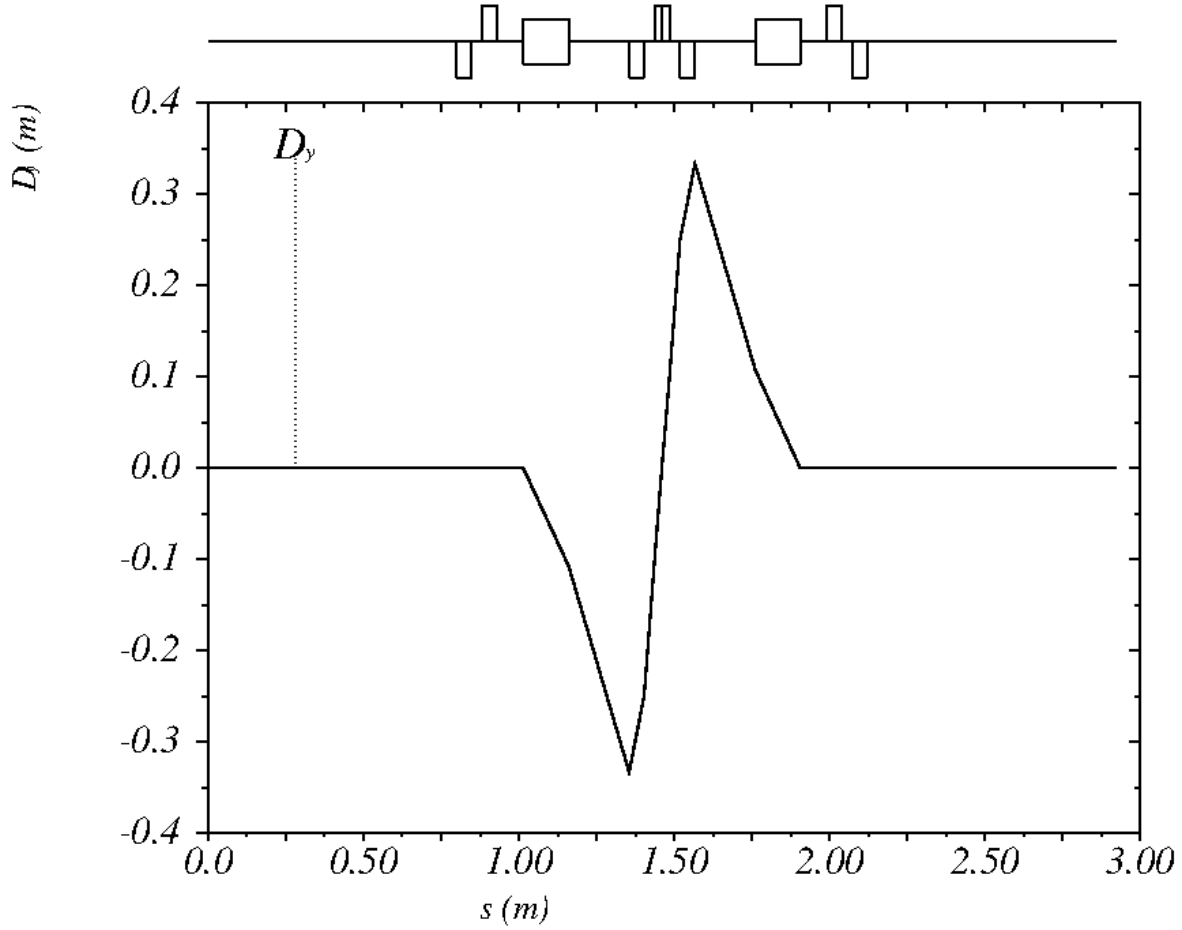

Figure 4.2: Dispersion function in the dogleg.

As can be seen, the Dispersion function is zero outside the arc. The bending magnets create the dispersion, but the quadrupole strengths are adjusted to compensate for it. As a result, the dispersion function returns to zero at the exit of the second bending magnet.

This a lattice can be implemented with one or three quadrupole lenses in the center of bending arc. The lattice with one quadrupole requires less space but offers limited flexibility. The lattice with quadrupole triplet, while requiring more space, provides significantly greater flexibility in beam focusing. This is especially important for high bunch charge, where space charge effects can critically impact the electron beam dynamics.

Using a dogleg lattice for the bending arc allows the implementation of the following beam trajectories (See Figure 4.3).

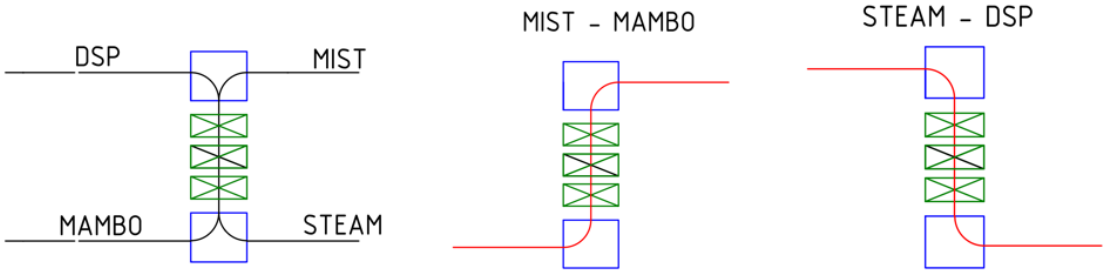

Figure 4.3: Trajectories of electron beam in dogleg [67].

4.2.2 Double bend achromat

A lattice of bending arcs, commonly referred as a Double Bend Achromat (DBA) is another version of the bending arcs [43]. The layout of DBA lattice is shown in Fig. 4.5. This lattice type was proposed by Panofsky [**?**].

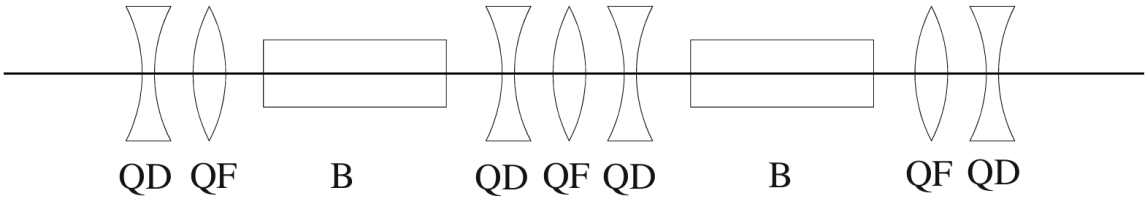

Figure 4.4: The layout of a DBA lattice with a quadrupole triplet in the center of the arc. B - bending magnet, QD - horizontally defocusing quadrupole, QF - horizontally focusing quadrupole.

This structure consists of two bending magnets and one or more quadrupoles symmetrically placed in the center of the arc to form the beam and suppress of dispersion function. The full structure of such a channel includes a quadrupoles doublet or triplet to provide the matching of the lattice functions into the first bending magnet. The central

part of the lattice between the bending magnets could consist of one or more quadrupoles, and its function is to focus the dispersion function such that it is matched again to zero at the end of the second bending magnet. Such bending arc allows to realize the follow beam trajectories (See Figure 4.3).

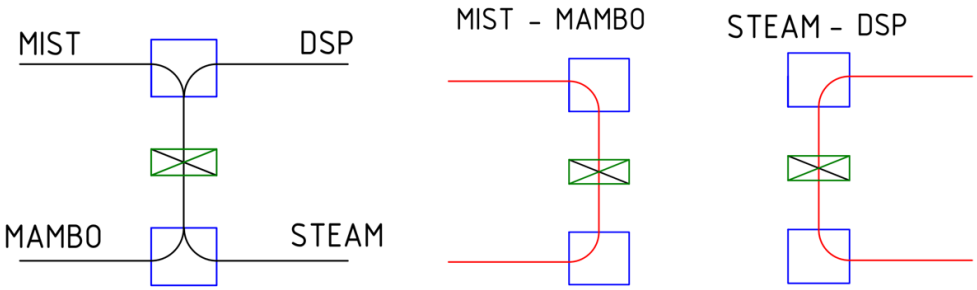

Figure 4.5: Trajectories of electron beam in the double bend achromat [67].

This bending arc lattice has the following dispersion function see Fig. 4.6. As can be seen, the dispersion function is zero outside the arc. The bending magnets create the dispersion, but the quadrupole strengths are adjusted to compensate for it. As a result, the dispersion function returns to zero at the entrance of the second bending magnet.

DBA lattice offers less flexibility (with one quadrupole), and the beam is rotated in a different direction than required. Therefore, to utilize this lattice, we would need to swap the positions of the MIST source and the DSMP. However, in this situation parts of the MIST source would collide with tuners from the first MAMBO section.

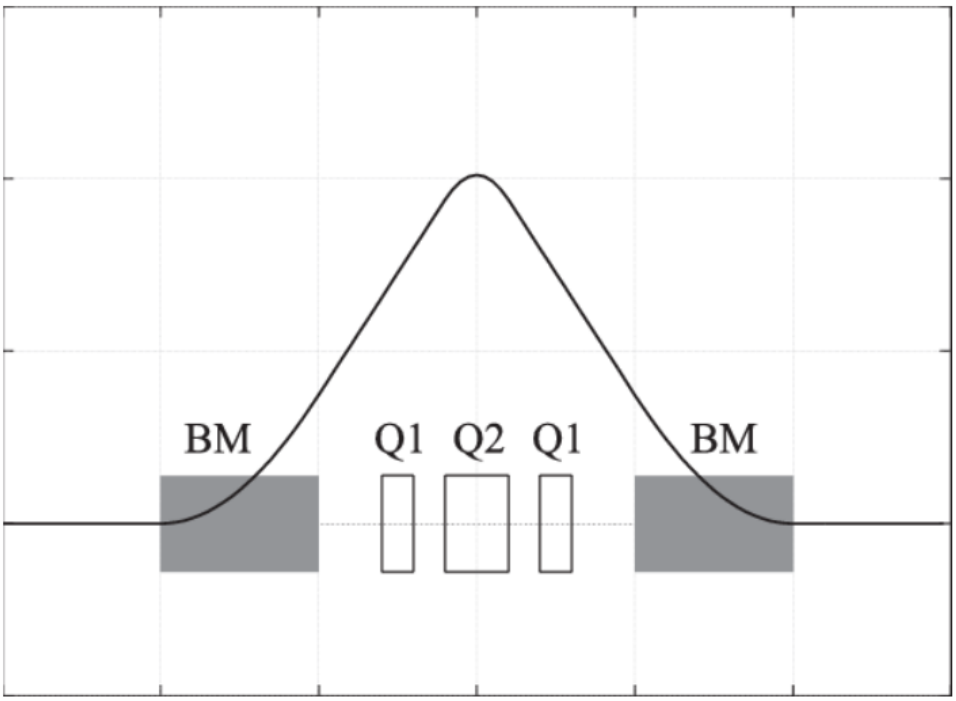

Figure 4.6: Dispersion function in the DBA.

4.2.3 4 alpha magnets

Another possible solution for beam transportation is to use a bending arc lattice with four alpha magnets. The matter is that, this magnet doesn't create dispersion and dispersion function will be zero along all channel. Such a bending arc lattice allows for the realization of the following beam trajectories (See Figure 4.7).

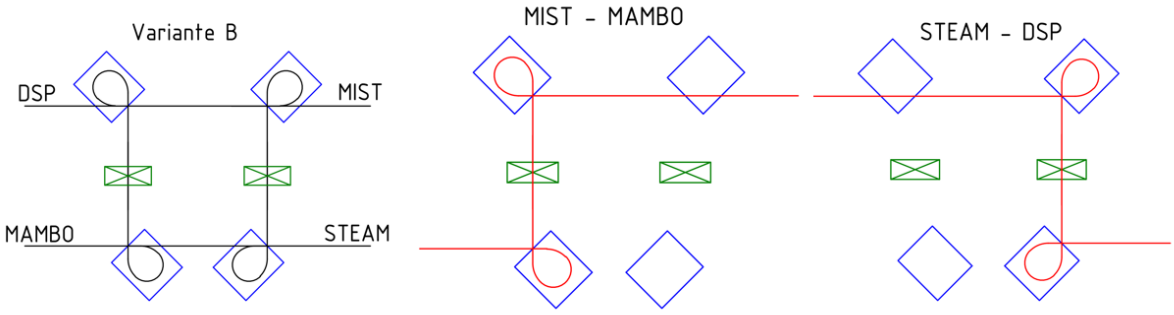

Figure 4.7: Trajectories of electron beam in bending arc from 4 alpha magnets [67].

The dispersion function remains zero along the entire arc, except within the alpha magnets [58]. The trick of the alpha magnet is the field strength increase to the pole face which makes it dispersion free.

The alpha magnet has a certain disadvantage compared to sector dipole magnets because the bending radius gets quite small at the turning point of the trajectory. The magnetic field at the maximum could reach about 40 mT, corresponding to only approximately 3 cm at 100 kV.

This structure can also be implemented using one or more quadrupoles positioned in the center of the arc. However, installing four alpha magnets requires significantly more space than is available in the MESA tunnel.

Therefore, the dogleg lattice for the bending arc was chosen for its flexibility and because it does not require additional modifications to the tunnel.

4.3 Linear optics of separation beamline

Choosing the appropriate bending arc is crucial for the design of a transport channel as it directly affects the beam's parameters and stability. A well-designed bending arc ensures precise beam guidance and focusing while minimizing dispersion function.

In our case, the dogleg with three quadrupoles in the center of the arc is the most suitable option of bending arc lattice. It effectively compensates for dispersion function and and allows for flexible beam focusing. This is especially important for the high-charge electron bunches, where strong space charge effects play a significant role in beam dynamics within the transport beamline.

The optical structure of the proposed beamline consists of two quadrupole doublets and the 90-degree dogleg. The structure of proposed lattice in shown in Figure 4.8.

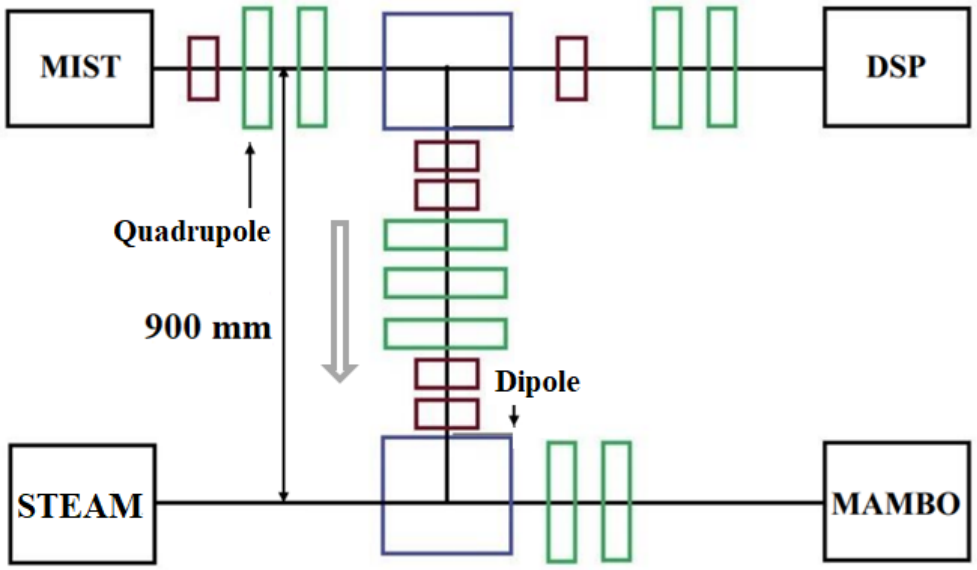

Figure 4.8: Layout of the designed separation beamline.

The initial lattice of this separation beamline is symmetrical. So, let's look in more detail at the motion of the electron beam from electron source MIST to the first acceleration section of MAMBO. Such a lattice is shown in fig. 4.9.

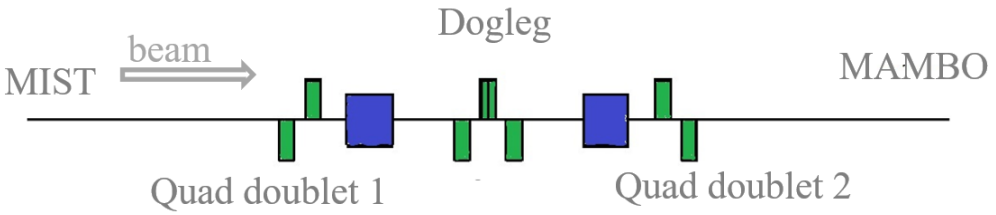

Figure 4.9: Lattice of the designed separation beamline from the source MIST to acceleration section of MAMBO.

The optical structure of the proposed beamline consists of Quad Doublet 1, which helps to form optimal parameters of the beam before it enters the bending arc. In the bending arc, a quadrupole triplet is used to manage the dispersion function. Finally, the second quad doublet shapes and focuses the electron beam for transport to the buncher.

4.4 Separation beamline linear model

Taking into account the analysis above and utilizing simulation codes such as Beamoptics and MAD-X [44], we obtained the beta functions (see Fig. 4.10) and dispersion functions (see Fig. 4.11) for this transport beamline.

The linear model of this separation beamline was simulated using the direct matrix method and the codes MAD-X [44], Beamoptics [45] and partly OPAL [11], [40]. These codes enable beam dynamics simulations based on both matrix and hard-edge models, without accounting for space charge effects or fringe fields.

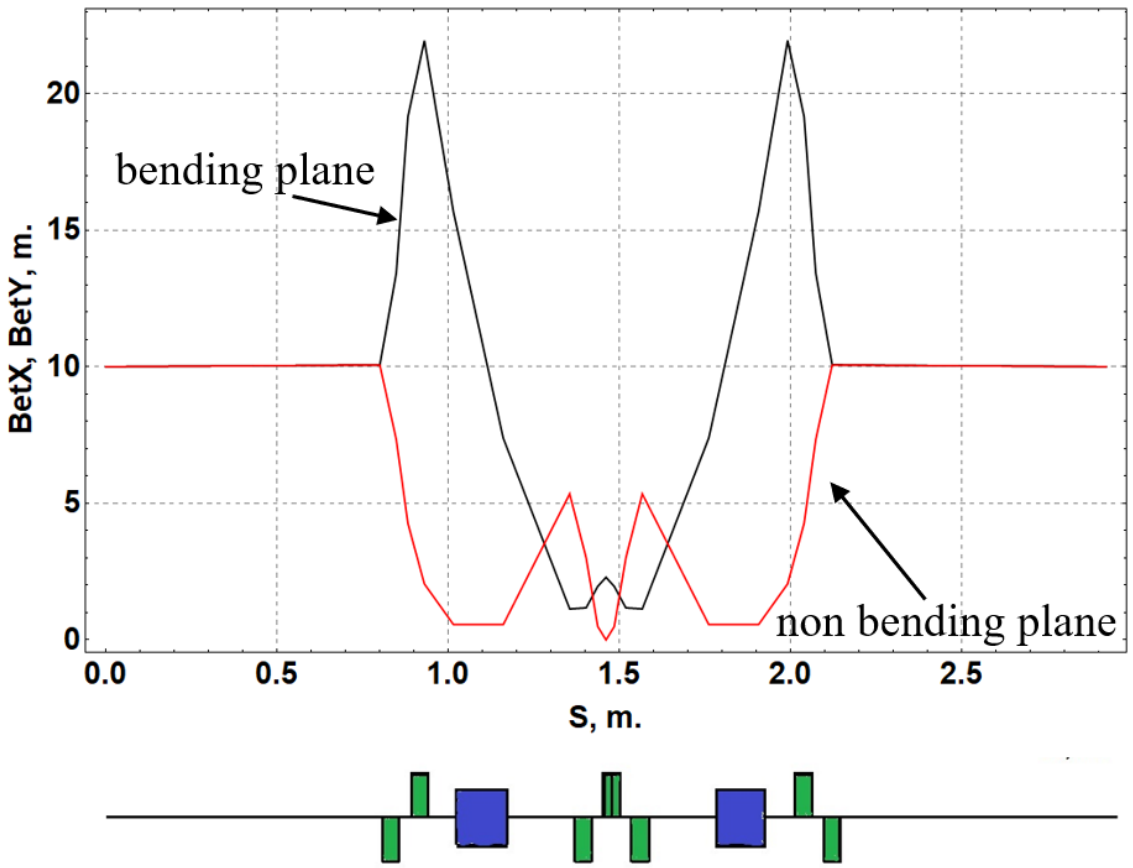

Figure 4.10: Beta functions it the separation beamline.

MAD-X (Methodical Accelerator Design - X) is a powerful and widely used software developed at CERN for designing, simulating, and analyzing particle accelerators. It is based on a matrix formalism and symplectic tracking methods, allowing for precise calculations of beam optics and dynamics. MAD-X provides tools for linear and nonlinear beam optics, Twiss parameter calculations, closed orbit analysis, and chromaticity corrections. The software supports both thick-lens and thin-lens approximations, enabling accurate modeling of complex accelerator lattices. It is commonly used for lattice design, beam transport studies, tune and stability analysis, and dynamic aperture calculations[44].

BeamOptics is a matrix-based simulation code developed at KPH [45], specifically designed for beam dynamics simulations in the linear structures.

OPAL (Object-Oriented Parallel Accelerator Library) is an advanced simulation software designed for tracking and modeling particle beams in complex accelerator environments. OPAL was developed at PSI (Paul Scherrer Institute). This code employs parallelized computing to efficiently handle large-scale simulations, making it particularly suitable for high-intensity beams. OPAL supports linear and nonlinear beam dynamics and offering symplectic particle tracking. It incorporates self-consistent space charge calculations and electromagnetic field solvers, allowing for the modeling of beam interactions with external fields. OPAL is used for designing and optimizing accelerators and beam transport simulations [11], [40].

Figure 4.12 illustrate results of simulation of the horizontal beam dimension for the given separation beamline as calculated by different codes such am Mad-X and Beamop-

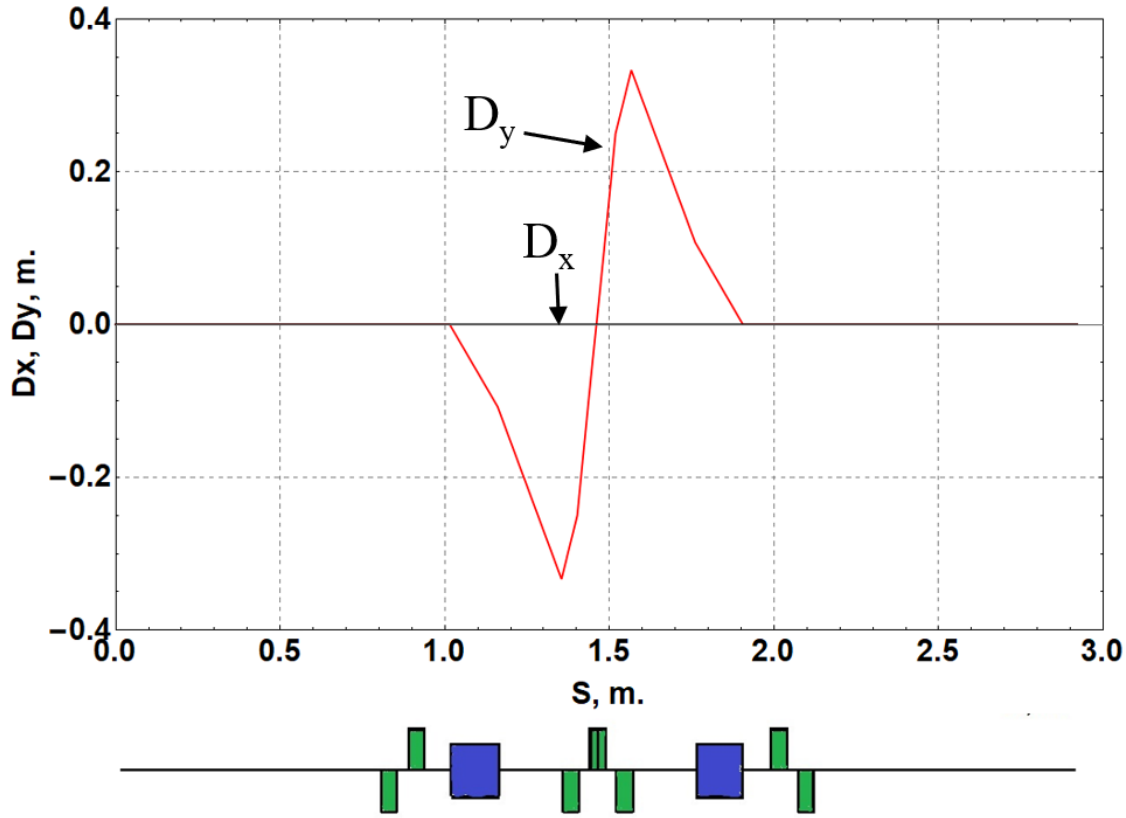

Figure 4.11: Dispersion functions it the separation beamline.

tics.

Moreover, simulations with OPAL with switched off the space charge solver give similar results to those obtained with simulation codes that use the matrix formalism (such as Beamoptics).

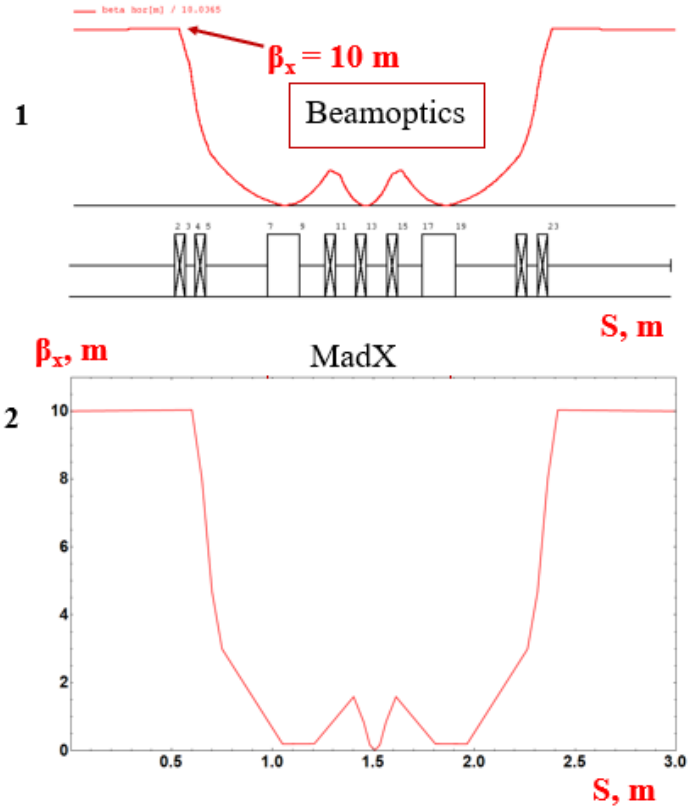

Figure 4.12: Horizontal beta-function with two different codes : MAD-X and Beamoptics.

Chapter 5

Beam dynamics with space charge

5.1 CST Studio Suite

The equations Eq. 2.62 and Eq. 2.63 require special conditions, such as a uniform space charge density, which are not satisfied in our case. Given that analytical solutions of such problems are not possible, numerical simulation remains the only viable approach. One of the possible tools for solving such problems is numerical simulations in CST Studio Suite (CST).

CST is a comprehensive simulation software suite used for modeling electromagnetic fields and particle dynamics [37]. CST is a software suite that enables the simulation of a wide range of physical phenomena related to electromagnetic fields and charged particle interactions. It integrates multiple specialized solvers, including the Time Domain Solver (for direct time-domain simulations), the Frequency Domain Solver (for frequency-domain calculations), the Eigenmode Solver (for finding resonator eigenmodes), the Particle-in-Cell (PIC) Solver (for self-consistent simulation of charged particle dynamics), and the Particle Tracking Solver (for precise tracking of particles under electromagnetic forces).

In CST Studio Suite included several types of solvers, that allow solving a wide range of physical problems. These solvers include [37], [38], [39]:

Particle-in-Cell (PIC) Solver performs self-consistent simulations of large ensembles of charged particles interacting with electromagnetic fields, updating both particles and fields together. It captures nonlinear phenomena such as space charge and secondary electron emission. It also offers a realistic representation of complex interactions between fields and particles, often requiring significant computational resources yet enabling the study of nonlinear and transient effects.

The Eigenmode Solver determines resonant modes by solving the eigenvalue problem for closed or periodic structures. It identifies the resonant frequencies and corresponding electromagnetic field distributions in microwave resonators, accelerating cavities, and related systems. This tool supports the optimization of resonator geometry to minimize losses, achieve target Q-factors, and gain a detailed understanding of the internal field configuration.

The Particle Tracking Solver (PTS) simulates the trajectories of charged particles within specified or precomputed electromagnetic fields. It enables accurate modeling of particle dynamics in accelerators, magnetic transport systems, and other setups where beam quality, emittance control, and precise focusing are essential. The solver accounts for effects such as space charge and beam loading, ensuring realistic stability analysis. It can also be coupled with results from other solvers, allowing simultaneous investigation

of field distributions and particle motion in a unified simulation framework.

One of the most important solvers for separation beamline simulation is the Eigenmode Solver, which is used for modeling the field in the first buncher of main MESA beamline. Moreover, the bunching system in MESA consists of two sequential RF cavities operating at the fundamental (1.3 GHz) and second harmonic frequencies (2.6 GHz). In this work, only the first buncher was used, therefore, further optimization with more parameters should be done.

The Magnetostatic Solver is employed to simulate magnetic fields in solenoids for the alternative-strength beamline, as well as in quadrupole lenses and other solenoid configurations. Additionally, the Particle-in-Cell (PIC) Solver is used to model the complete separation beamline. It enables particle dynamics simulations in imported field maps generated by other projects, self-consistently updating both particles and fields to account for their mutual interaction. This approach captures complex nonlinear effects, including space-charge phenomena, ensuring realistic modeling of beam behavior.

Let's take a look at the numerical methods realized in CST[39], [38].

1. The first method is finite element method, it divides the simulation domain into small elements and solves Maxwell's equations locally. It approximates the solution by minimizing the residual over the entire domain:

$$\nabla \times \left(\mu^{-1}\nabla \times \mathbf{E}\right) - \omega^2 \epsilon \mathbf{E} = 0$$

Where μ is the permeability, $\mathbf{E}$ is the electric field, ϵ is the permittivity, and ω is the angular frequency.

2. The second method is finite difference time domain, it discretizes time and space, solving Maxwell's curl equations iteratively:

$$\frac{\partial \mathbf{E}}{\partial t} = \frac{1}{\epsilon}\nabla \times \mathbf{H} - \frac{\mathbf{J}}{\epsilon}$$

$$\frac{\partial \mathbf{H}}{\partial t} = -\frac{1}{\mu}\nabla \times \mathbf{E}$$

Where $\mathbf{H}$ is the magnetic field, and $\mathbf{J}$ is the current density.

3. The third method is particle in the cell method, it couples particle motion with the field equations, updating particle positions and velocities while solving for the electromagnetic fields.:

$$m\frac{d\mathbf{v}}{dt} = q(\mathbf{E} + \mathbf{v} \times \mathbf{B})$$

Where m is the particle mass, q is the particle charge, $\mathbf{v}$ is the velocity, $\mathbf{E}$ is the electric field, and $\mathbf{B}$ is the magnetic field. The Lorentz force calculated by the PIC code is the superposition of the external fields and by the moving space charges.

5.2 Macro particles in CST

In CST Studio Suite, the so-called macro-particles approach is often used for simulating charged particle beams. Instead of calculating each electron or ion individually (which is nearly impossible at high currents or densities), the software groups a set of real particles into one "notional" particle.

Each macro-particle is characterized by a total charge and approximately the same motion parameters as the real particles combined into it. In that case, the total bunch charge will be equal to

$$q_b = \sum_{i=1}^{N} q_i.$$

Where, q_b is bunch charge, q_i is charge of macro-particle under number i, and N is number of macro-particles.

The charge of a macro-particle can be either smaller or significantly larger than the elementary charge $e = 1.602 \times 10^{-19}\,\mathrm{C}$. As an example, Figure 5.1 shows the charge for macro-particles in a 100 fC bunch, which is represented by approximately 7×10^5 macro-particles. As can be seen from the Figure 5.1, the macro-particle charges can vary by up to two orders of magnitude.

macro-charge
-3.9534835e-21
-1.4433643e-20
-8.3300703e-22
-3.7281058e-21
-1.2215332e-20
-1.2215332e-20
-1.9062608e-20
-2.4792141e-22
-2.4792141e-22
-2.4792141e-22
-5.746702e-22

Figure 5.1: Prime charges of individual macro-particles in Coulombs.

The matter is that CST calculates RMS beam envelopes and RMS emittance based on the macro-particle distribution without accounting for charge differences. Therefore, to analyze the beam profile, it is necessary to take into account the charges of the macro-particles in the bunch [3]. The simulation results must therefore be exported as ASCII file from position monitors and processed externally. These files contain the phase-space information at a given point in time for each macro-particle (posX, posY, posZ, particleID, sourceID, time, mass, charge, macro-charge, momX, momY, momZ). Where, posX, posY, posZ – spatial coordinates of the macro-particle, defining its position at a given time step, particleID – unique identifier of the particle, sourceID – identifier of the source from which the particle was emitted, time – time stamp, when the particle data was recorded, mass – particle mass, charge – particle charge, macro-charge – macro-particle charge, representing the total equivalent charge of a macro-particle, momX, momY, momZ – particle momentum along the X, Y, and Z axes.

To compute the particle RMS parameters, for instance, in the x-plane, the following formula should be used, where the ratio $\frac{q_i}{q_b}$ acts as a weight factor for the macro-particle within the bunch particle ensemble.

$$
\begin{aligned}
w_i &= \frac{q_i}{q_b}, \quad \sum_{i=1}^{N} w_i = 1, \\
\langle x \rangle &= \sum_{i=1}^{N} w_i \, x_i \\
\langle x^2 \rangle &= \sum_{i=1}^{N} w_i \left(x_i - \langle x \rangle \right)^2
\end{aligned}
\tag{5.1}
$$

This approach ensures an accurate consideration of macro-particle charges and allows for a precise description of the RMS parameters of the bunch.

5.3 Electron source MIST

Source MIST is designed to deliver high-current (up to 10 mA average, 7.7 pC per bunch) unpolarized electron beams at 100 keV [4]. It employs a robust multi-alkali K_2CsSb photocathode, which can be operated at at least one order of magnitude higher residual gas levels than the GaAs used in STEAM. Moreover, KCsSb has a much faster pulse response and no diffusive halo in time [60], [61].

MIST source will used as the second unpolarized electron source for MESA project [9]. The layout of electron source is shown in the Figure 5.2.

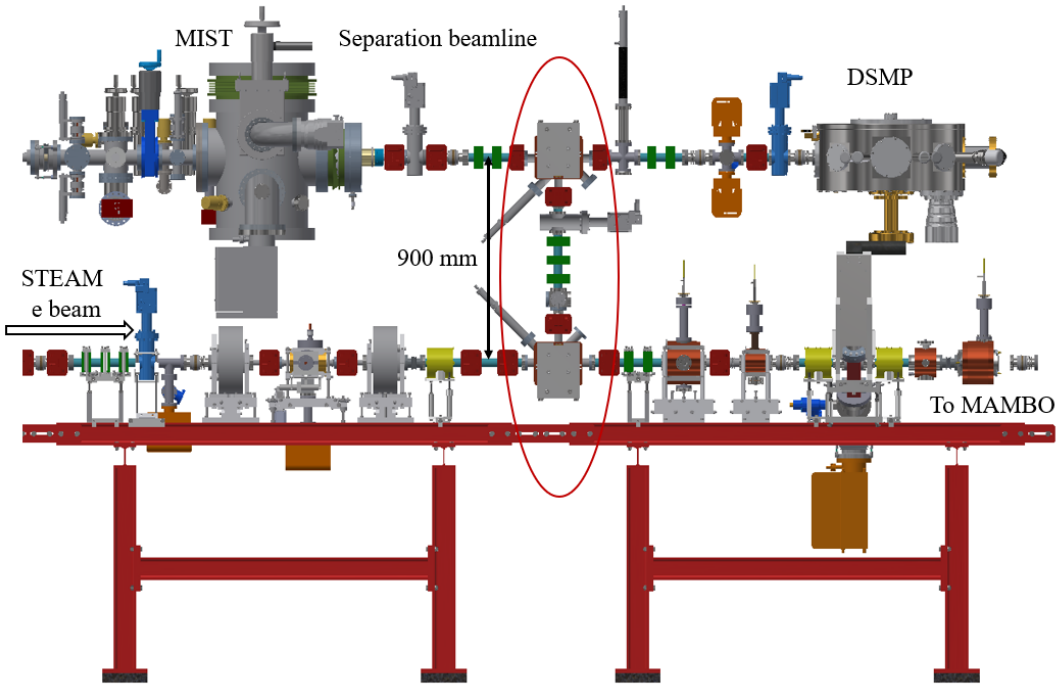

Figure 5.2: Schematic diagram of the separation beamline. The electron beam originates at the STEAM source on the left, travels through the transport channel, and is injected into the first acceleration section of MAMBO on the right. The diagram also indicates the position of the source MIST and the DSMP (Double Scattering Mott Polarimeter).

As can be seen in Figure 5.2, the electron source MIST is arranged above the main beamline of MESA. This positioning is due to the geometrical restrictions of the building, which require the beam to be injected at large-angle deflections, making the beam dynamics more complex.

The goal of the MESA project in its second stage is to increase the beam current from $1mA$ to an average of 10 mA, which corresponds to a bunch charge of 7.7 pC. Hence, operation at 100 keV with 7.7 pC per bunch is a basic design objective. Using the CST model of the MIST source ([4]), we can generate an electron beam distribution for beam dynamics simulations.

The initial RMS length of the produced electron bunch was set to 34 ps. In the experiment, this depends on the length of the laser-driven pulse, and $34ps$ is a value that has already been achieved with a compact laser diode [62]. The simulated 7.7 pC bunch at the exit of the MIST-source has an energy spread 0.8×10^{-3}.

It should be noted that the MIST source structure includes two solenoids that focus the produced beam, and before entering the transport channel, the beam travels approximately 800 mm. It is important to note that while the bunch propagates through the electron source, Coulomb forces act on particles in the bunch. Given a bunch charge of up to 7.7 pC and a particle kinetic energy of only 100 keV, these forces have a significant impact on beam quality. Fig. 5.3 shows the phase space for a 7.7 pC bunch. The transverse bunch dimensions are approximately 1 mm in both planes.

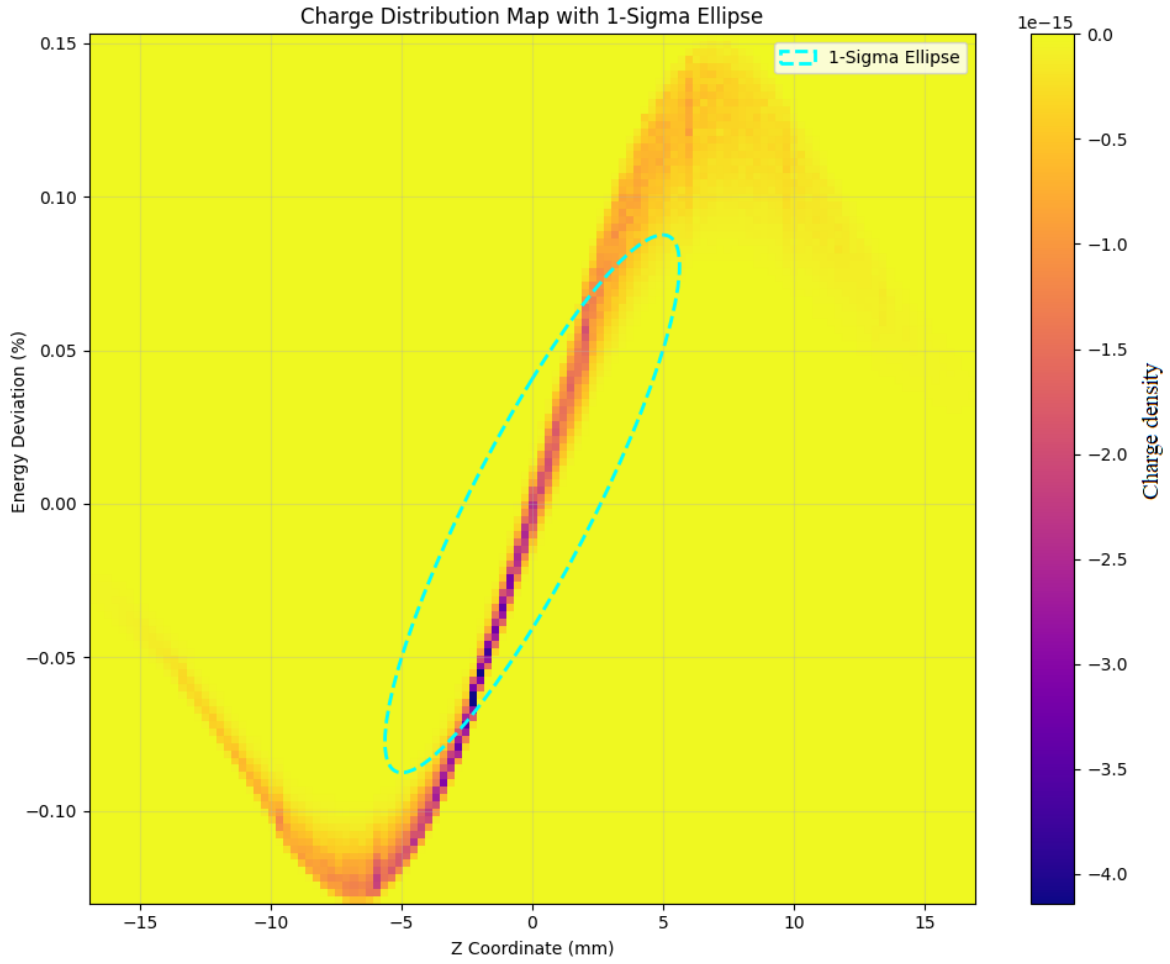

Figure 5.3: Longitudinal phase space of a 7.7 pC electron bunch at the separation beamline entrance.

5.4 CST model of separation beamline

Based on the designed separation beamline calculated using the matrix method (which does not account for space charge effects or fringe fields), the next step is to simulate beam dynamics with a tool that includes these effects. After design of lattice using the matrix method and after modeling the beam dynamics, we could build a CST model, see the presentation of results from the linear model in section 4.12.

This model allow us simulating the beam dynamics with real bunch distribution and bending magnets field.

Moreover, the linear model was symmetrical and was calculated up to the buncher. In the CST model, a buncher and two solenoids, which are installed after it, were added.

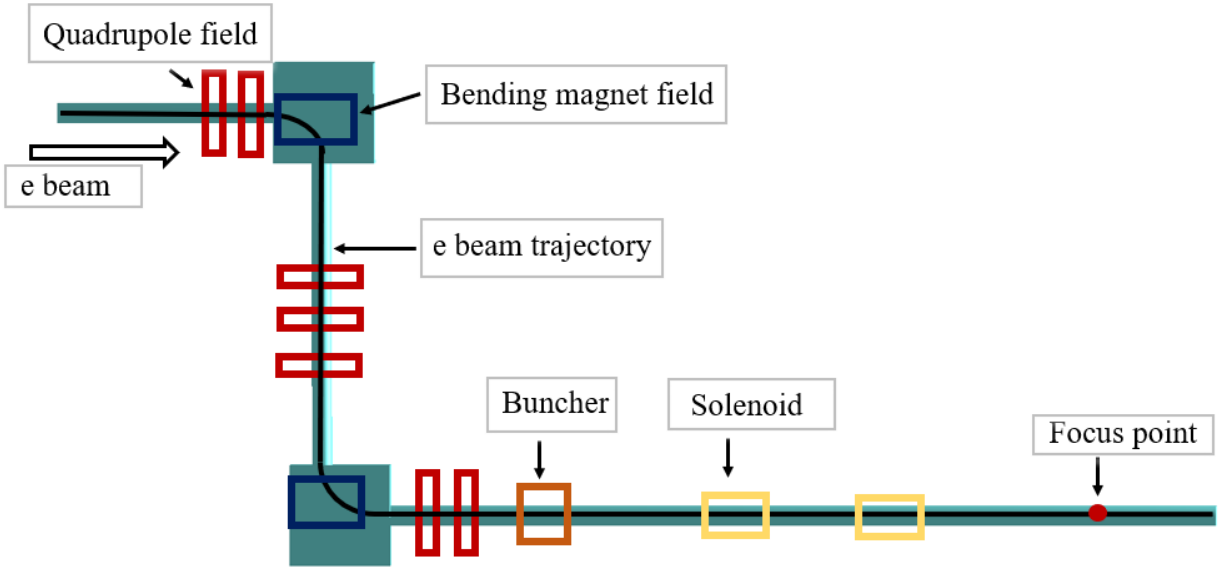

Figure 5.4: CST model of separation beamline.

Typically, calculations for such a long section with sufficient accuracy can take a significant amount of time, so the beam dynamics simulations were computed in a few steps:

1. Generating and transport the beam the beam from source MIST to the beginning of the separation beamline.
2. Transporting the beam from the start, through the quadrupole doublet, to the first magnet of the bending arc.
3. Transporting the beam through the bending arc, which consists of two bending magnets and a quadrupole triplet between them.
4. Transporting the electron beam from the exit of the bending arc to the first acceleration section of MAMBO.

To enhance computation speed, all fields for the quadrupoles, dipoles, solenoids, and the buncher were calculated separately and then imported into the CST structure.

5.5 CST model of optical elements

Let us now examine in detail the CST models of optical element were used in the simulation.

5.5.1 Quadrupole

Fig. 5.5 illustrates the appearance of the low gradient quadrupole designed for low-energy electron beam focusing [63]. This quadrupoles will be used in the construction of the separation beamline.

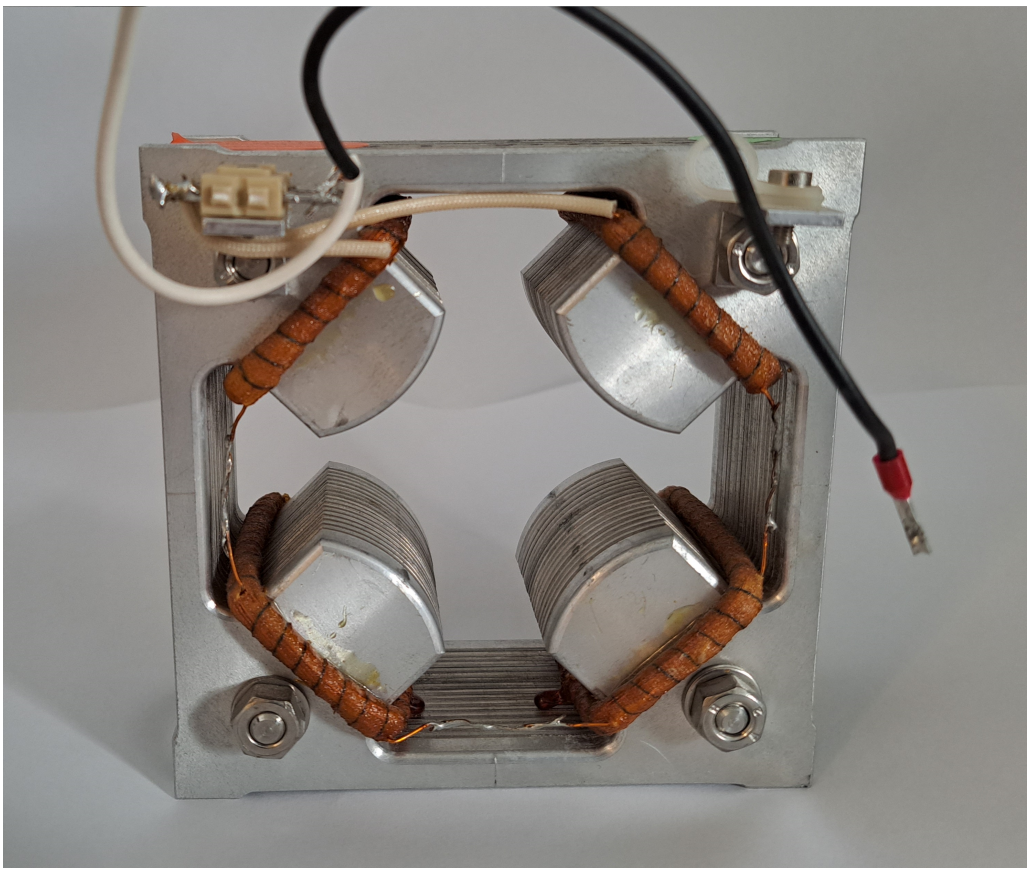

Figure 5.5: Quadrupole that will be used in the construction of the transport channel.

The actual length of this quadrupole is 40 mm, with an effective length of 48 mm and an aperture size of 42 mm. The maximum current, which can be set using the available power supply, is $1.4A$. Figure 5.6 presents the CST model of this quadrupole.

Figure 5.7 shows the magnetic field gradient along the quadrupole for a current of 0.3 A in a coil, with position 0 corresponding to the quadrupole's center.

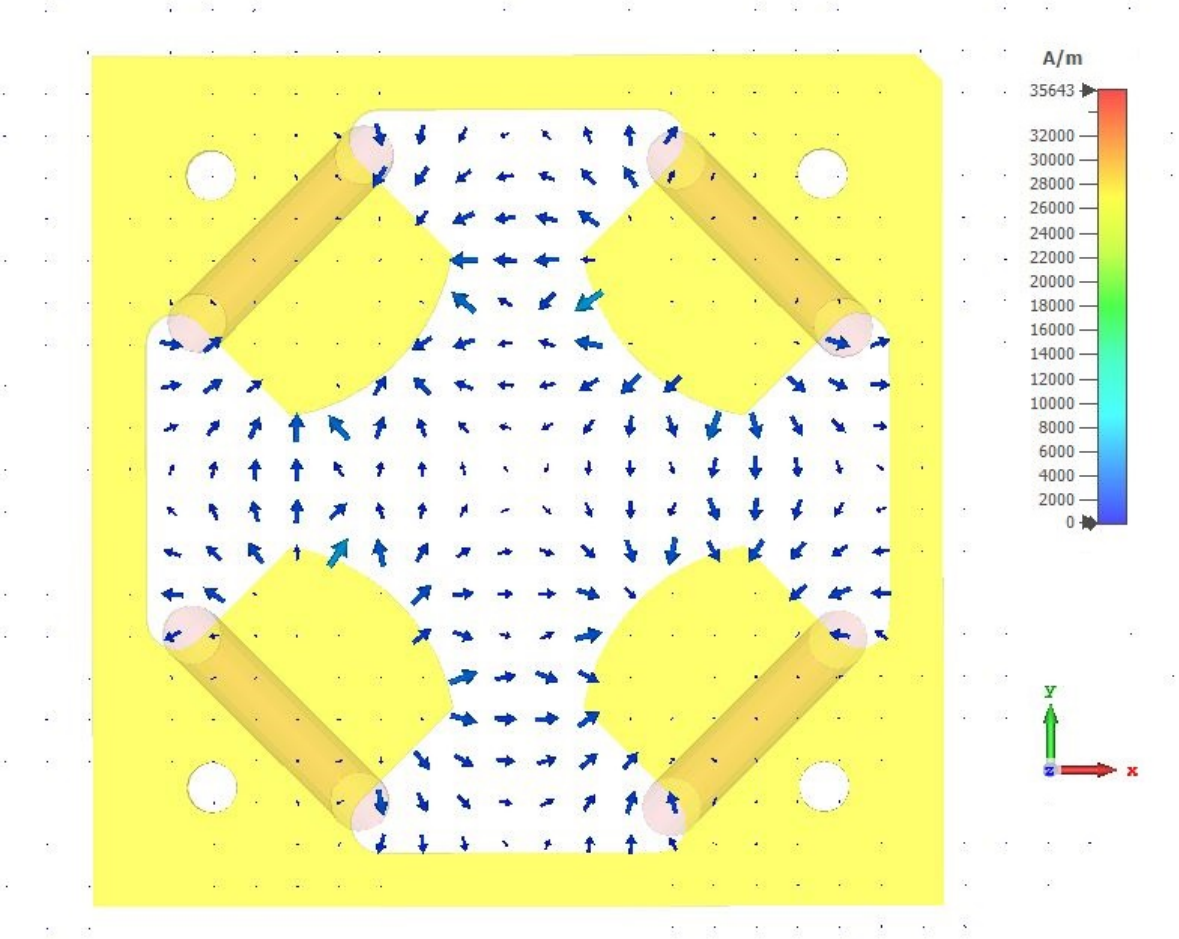

Figure 5.6: CST model of quadrupole for the transport channel.

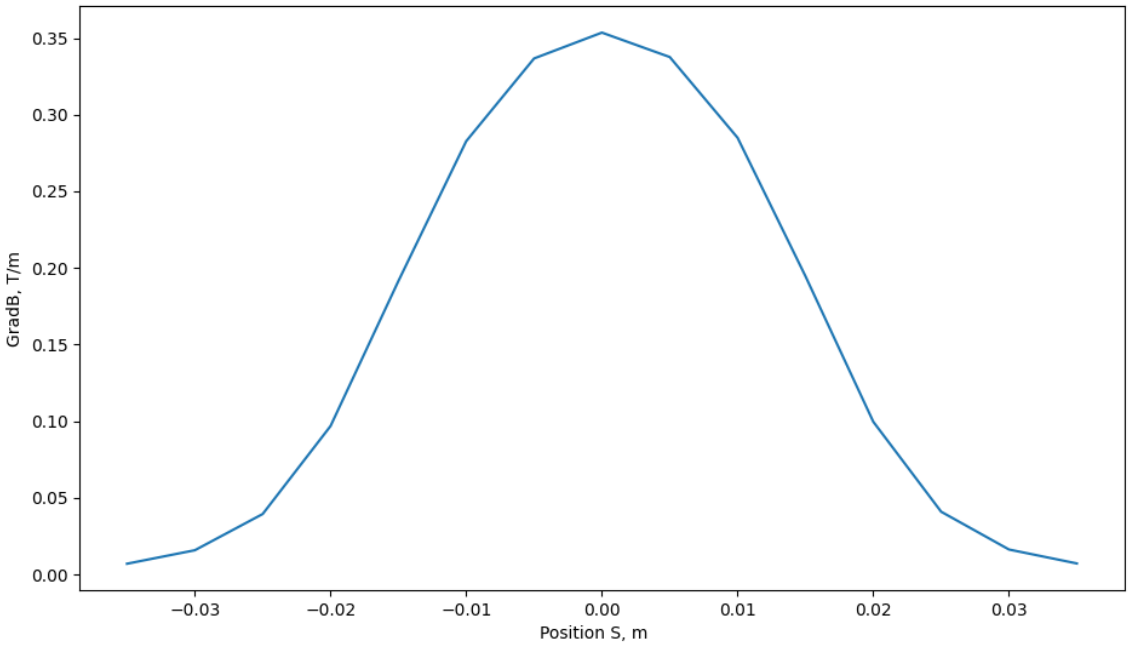

Figure 5.7: Magnetic field gradient along the quadrupole for a current of $0.3A$.

5.5.2 Solenoid

Solenoids consist of cylindrical coils of wire through which an electric current flows, generating a uniform magnetic field along their axis. This field exerts a Lorentz force on charged particles, causing them to spiral and focus in both transverse planes, making solenoids effective for beam focusing in low-energy accelerators. Figure 5.8 illustrate the CST model of two solenoids, these solenoids will be installed after the buncher to focus the beam and guide it towards the first acceleration section of MAMBO. For a beam at these energy levels, solenoids are the most effective choice for focusing.

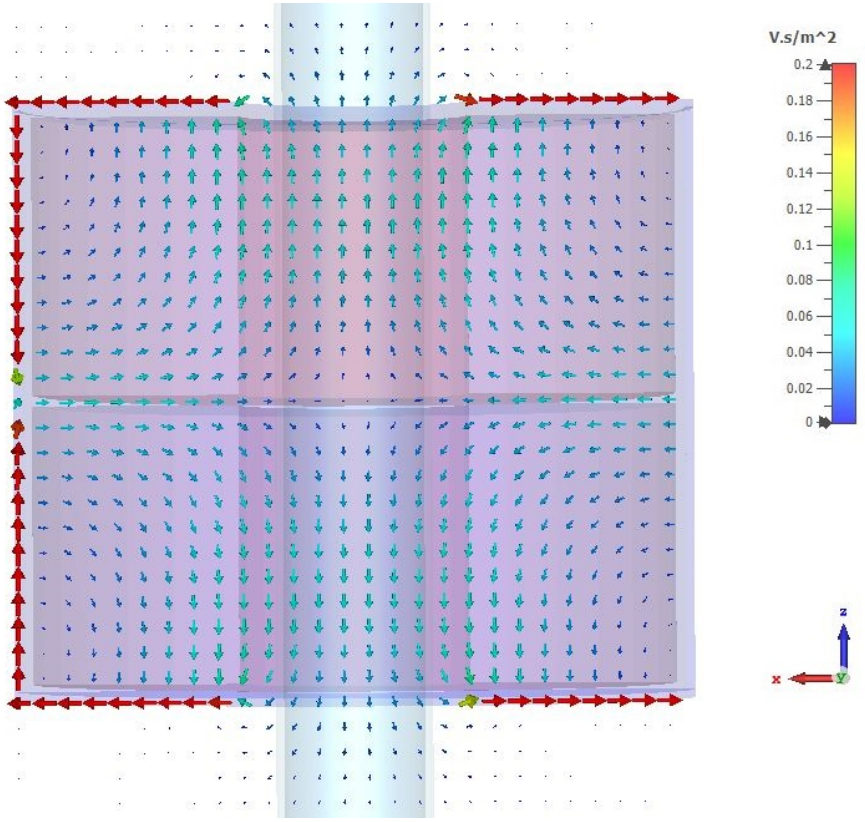

Figure 5.8: Solenoid that will be used in the construction of the transport channel.

5.6 100 keV beamline with C-shaped dipole

5.6.1 Transversal bunch sizes

Simulation results showed that it is possible to deliver a beam with the following horizontal (See Figure 5.9) and vertical phase space (See Figure 5.10) at the entrance to the first acceleration section of MAMBO for bunch charge 100 fC and 7.7 pC.

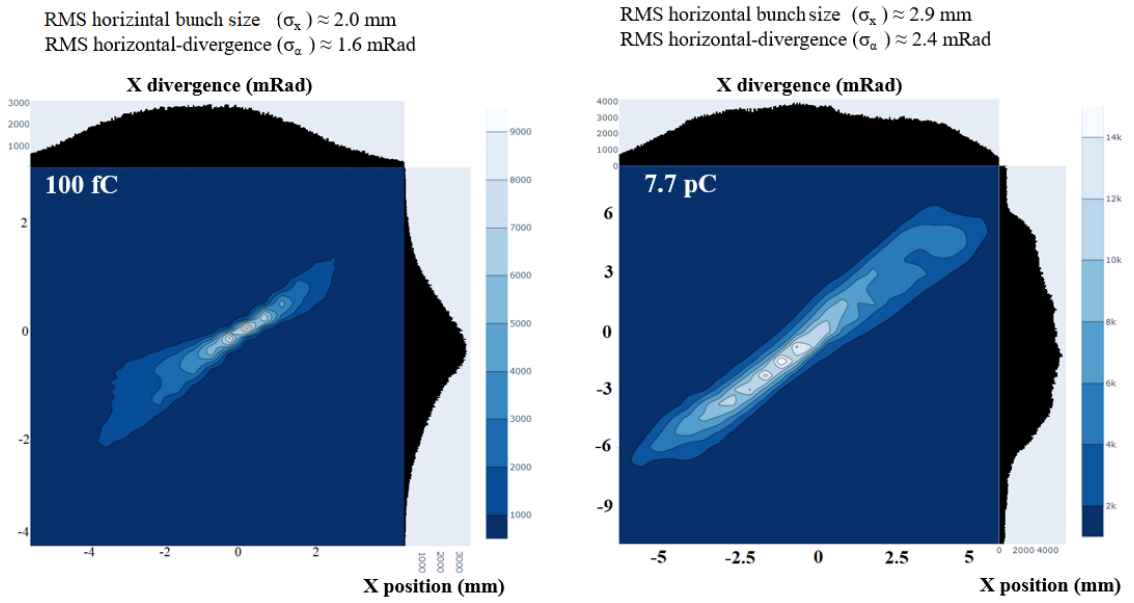

Figure 5.9: CST results of simulation for the horizontal phase space at the entrance to the first acceleration section of MAMBO for 100 fC and 7.7 pC bunch charge.

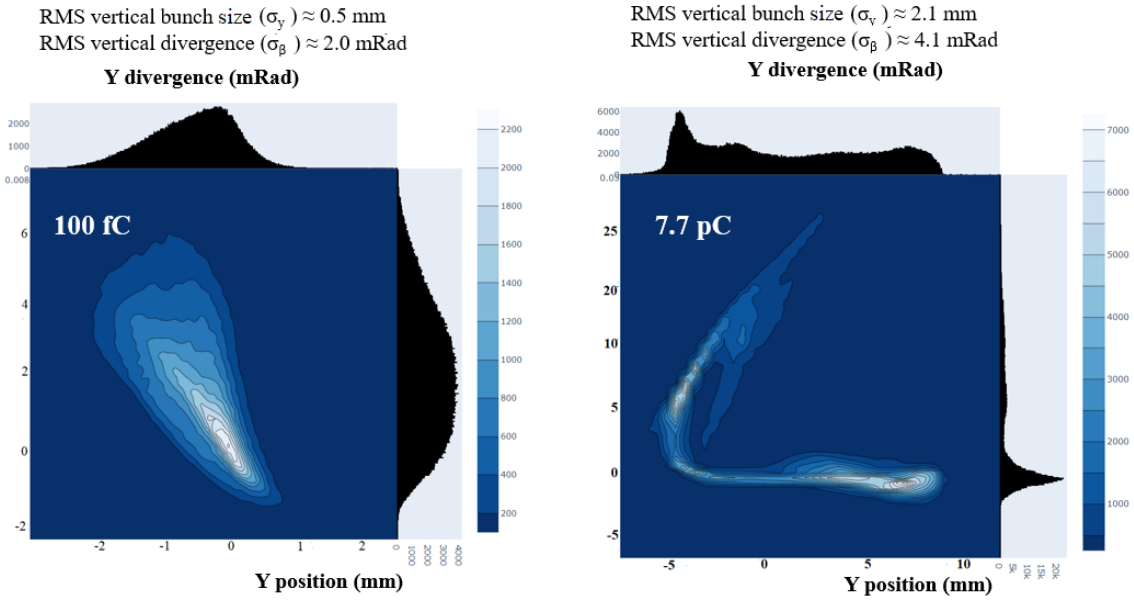

Figure 5.10: CST results of simulation for the vertical phase space at the entrance to the first acceleration section of MAMBO for 100 fC and 7.7 pC bunch charge.

At figure 5.11 is presented simulated transverse emittance at the entrance to the first acceleration section of MAMBO as a function of bunch charge.

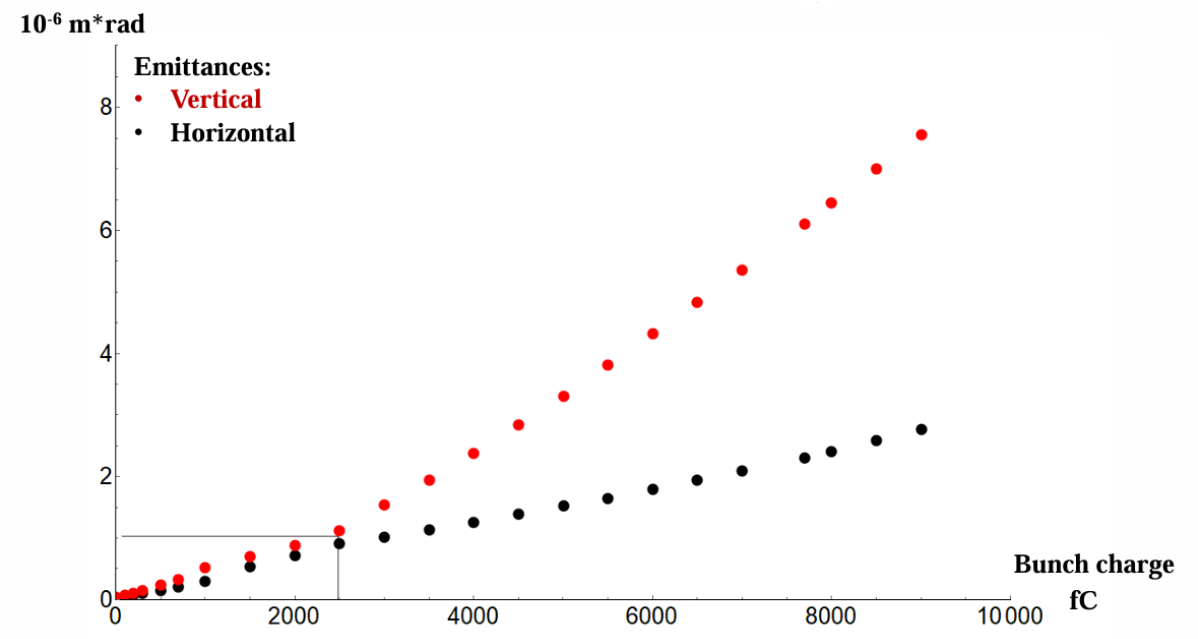

Figure 5.11: Simulated transverse normalized emittance at the entrance to the first acceleration section as a function of bunch charge.

5.6.2 longitudinal bunch sizes

The given figures illustrate the longitudinal phase space at the entrance to the first acceleration section of MAMBO: Fig. 5.12 corresponds to a bunch charge of $0.77\,pC$, while Fig. 5.13 represents a bunch charge of $7.7\,pC$.

The maximum electric field ($E_{\max}$) in the buncher for a charge of $0.77\,pC$ was $252.7\,kV/m$, whereas for $7.7\,pC$, it reached $321.5\,kV/m$.

The RMS phase space volume for $0.77\,pC$ is 4.48 keV$\cdot°$, while for $7.7\,pC$, it increases to 15.53 keV$\cdot°$. The RMS energy spread for $0.77\,pC$ is 1.34%, with an RMS bunch length of $0.64\,mm$. For $7.7\,pC$, the RMS energy spread is 1.05%, and the RMS bunch length extends to $1.83\,mm$.

The designed separation beamline efficiently transports the electron bunch from STEAM to the first acceleration section of MAMBO while compressing it to an RMS length of $1.78\,mm$ with an energy spread of 1.6% in the optimal configuration. This setup enables the achievement of a $10\,mA$ beam current.

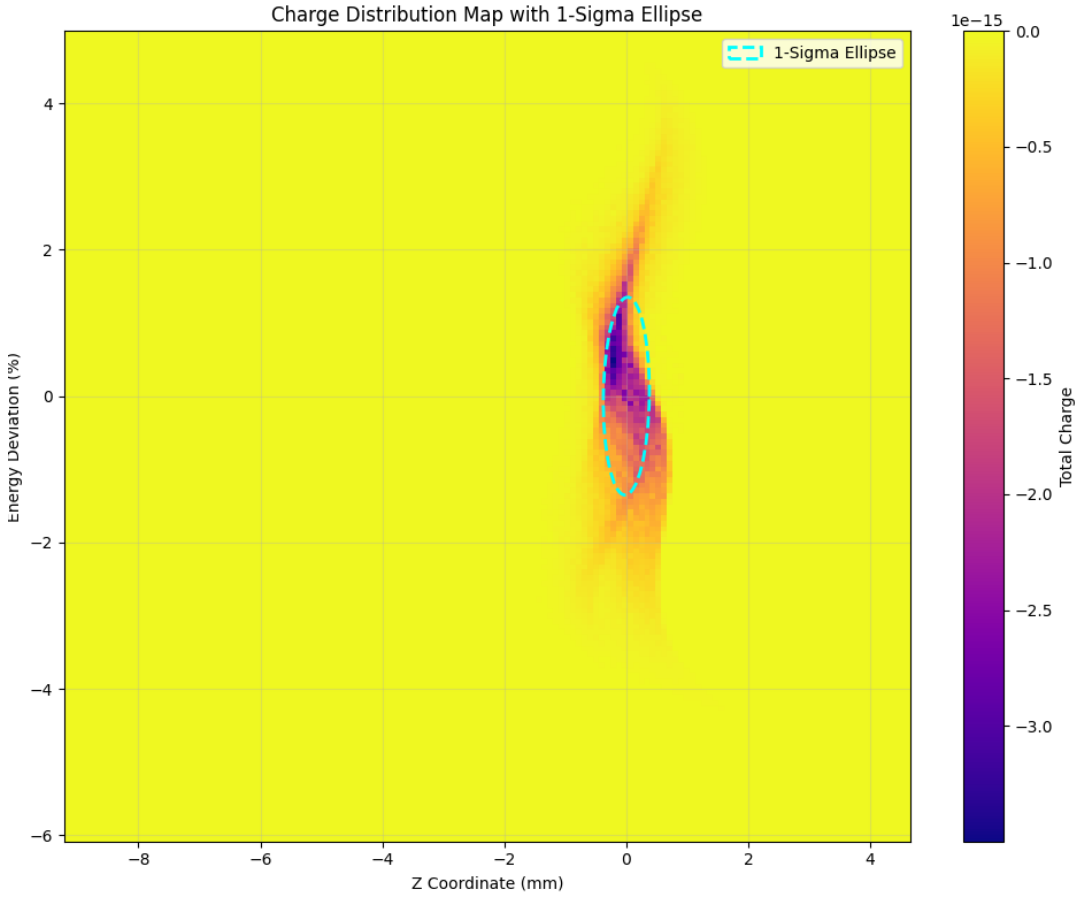

Figure 5.12: longitudinal phase space at the entrance to the first acceleration section of MAMBO for $0.77pC$ in a bunch.

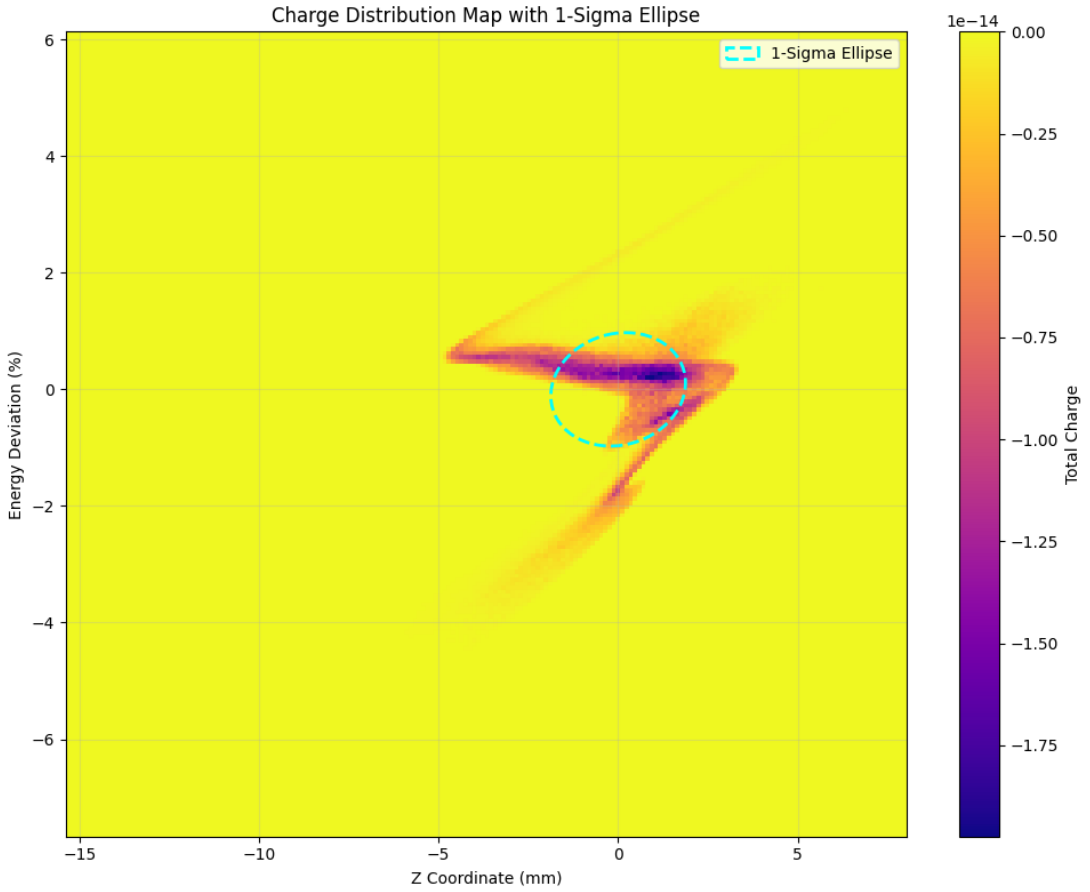

Figure 5.13: longitudinal phase space at the entrance to the first acceleration section of MAMBO for $7.7pC$ in a bunch.

5.7 Alternative beamlines

During our recent studies, we investigated whether other arrangements could yield better performance. The two alternative scenarios considered are:

1. An injection with two dispersion-free alpha magnets replacing the dipoles, with correspondingly adapted quadrupole focusing.

2. A straight injection beamline.

5.7.1 A straight injection beamline

A straight injection beamline appears to be the most promising, as it allows the electron source MIST to be positioned as close as possible to the first acceleration section of MAMBO. Consequently, the beam travels the shortest possible distance, minimizing emittance growth due to space charge effects. Additionally, this configuration eliminates the need for bending magnets, and therefore, there is no need to manage the dispersion function.

The straight beamline is only a theoretical option since it would require to disassemble a fraction of the MELBA system needed for STEAM. This would make spin-polarized beam impossible for a very long time-period.

The example of such structure with quadrupole doublet is present in Figure 5.14.

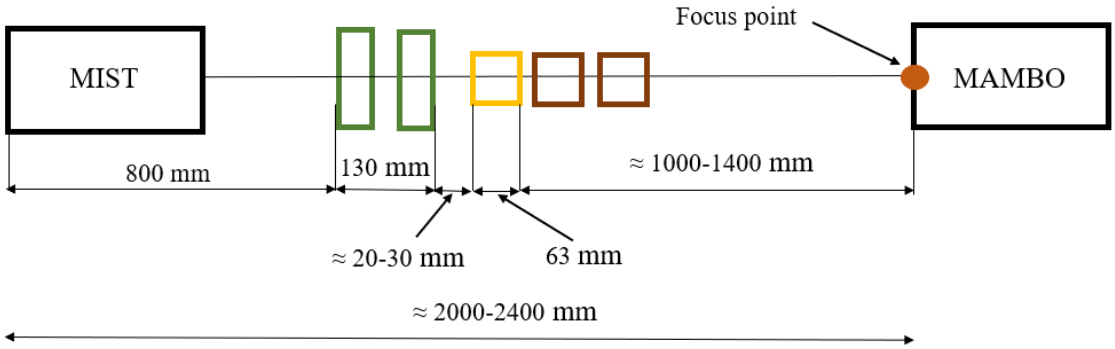

Figure 5.14: Layout of the straight beamline with 2 quadrupoles magnets for 7.7 pC.

Beta functions of such a structure calculated with MAD-X and OPAL are shown in Figure 5.15. And phase space at the entrance to the first acceleration section of MAMBO for 7.7 pC bunch charge are shown in Figure 5.16

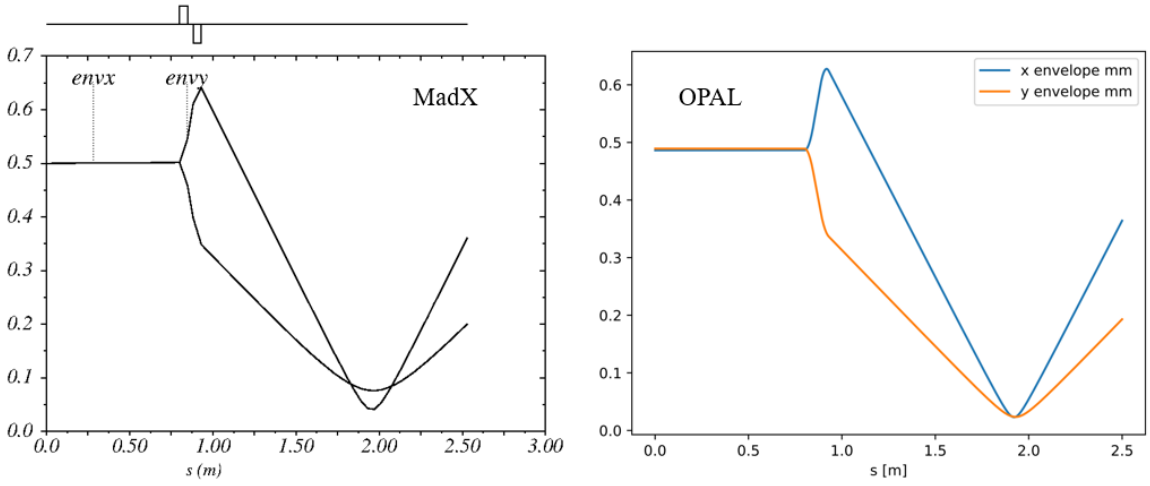

Figure 5.15: Layout of the straight beamline with 2 quadrupoles magnets for 7.7 pC.

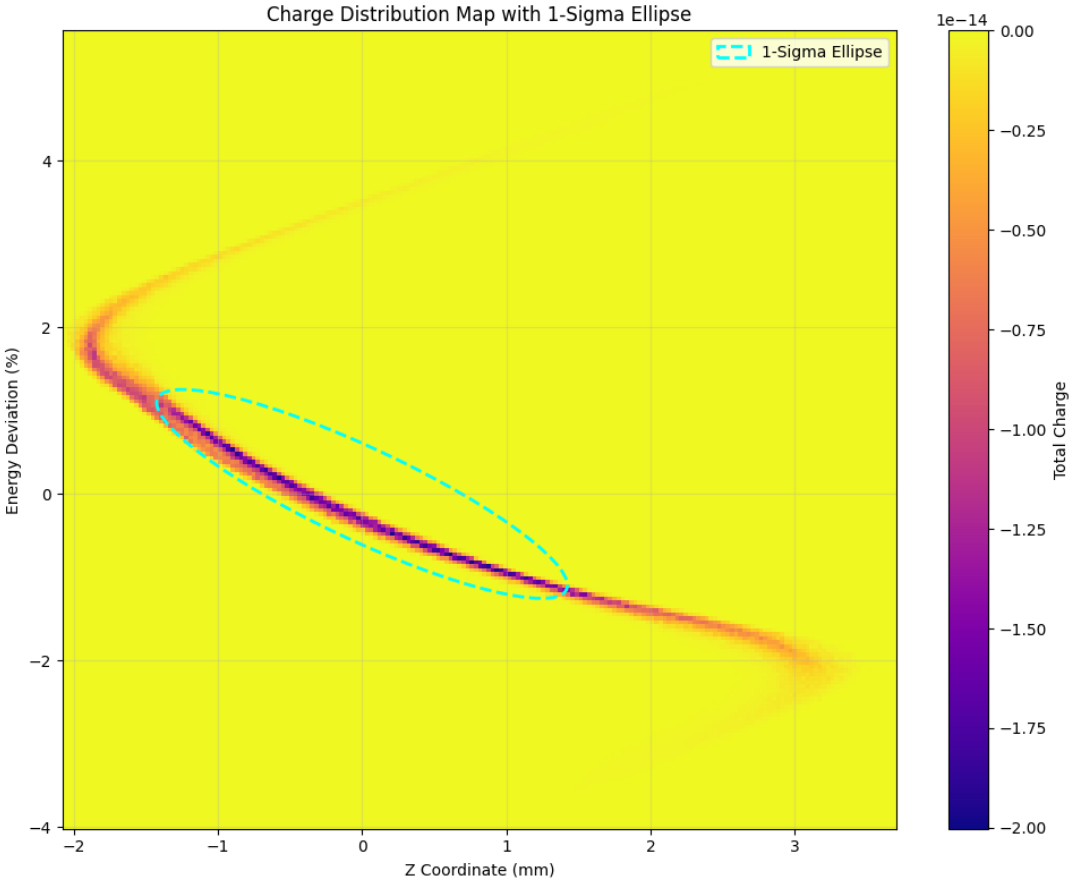

Figure 5.16: The RMS phase space of the straight beamline with 2 quadrupoles magnets for 7.7 pC.

The RMS phase space volume for 7.7 pC is 2.73 $\% * mm$. The lattice with C-shaped bending magnets for a bunch charge of 7.7 pC, the RMS phase space volume is almost twice as large. However, it is important to note that in the straight beamline, the bunch travels a shorter distance, making the straight beamline theoretically the better option.

5.7.2 Separation beamline with 2 alpha magnets

Since four alpha magnets occupy a significant amount of space, implementing such a transport system in reality is impractical due to spatial constraints. However, alpha magnets offer a key advantage over conventional bending magnets—they do not generate dispersion. As a result, a quadrupole triplet is not required in the deflection arc of such a channel; a single quadrupole in the center is sufficient to shape the beam. This unique property makes it particularly interesting to compare simulation results for a transport channel utilizing two alpha magnets.

For the CST simulation, the same channel geometry was used as in the C-shaped bending magnet lattice. The only modifications were replacing the bending magnets with alpha magnets and substituting the quadrupole triplet in the center with a single quadrupole lens. The CST model of this channel is shown in Figure 5.17.

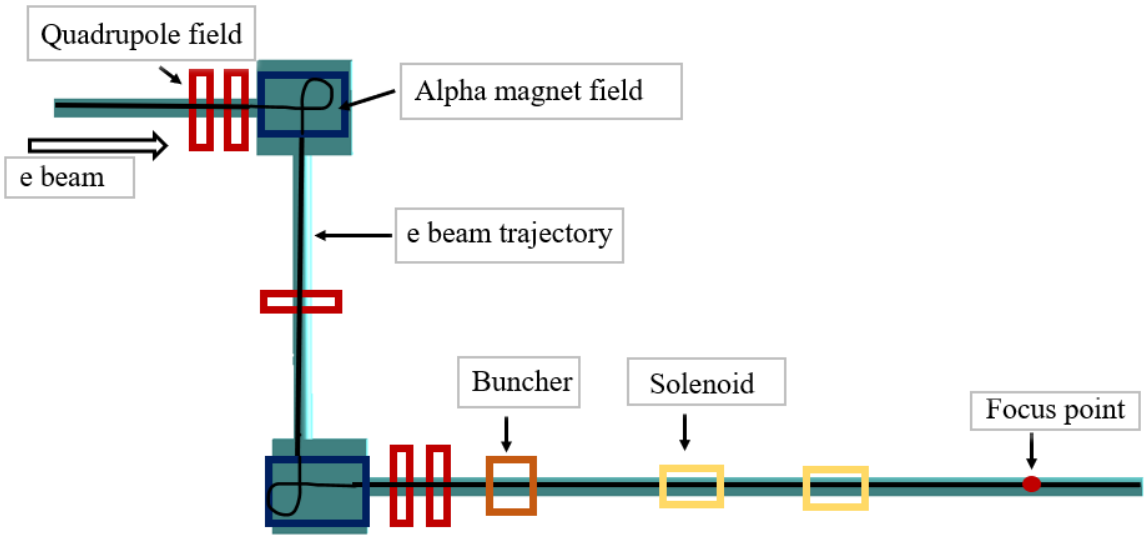

Figure 5.17: Layout of the beamline with 2 alpha magnets for 7.7 pC.

5.7.3 Comparison of transportation systems

To summarize the CST simulation results for the longitudinal size and energy distribution of the beam in different transport systems, all data is presented in a single figure (see Fig. 5.18) at the entrance to the first acceleration section. Additionally, Table 5.1 provides a comprehensive overview of these parameters.

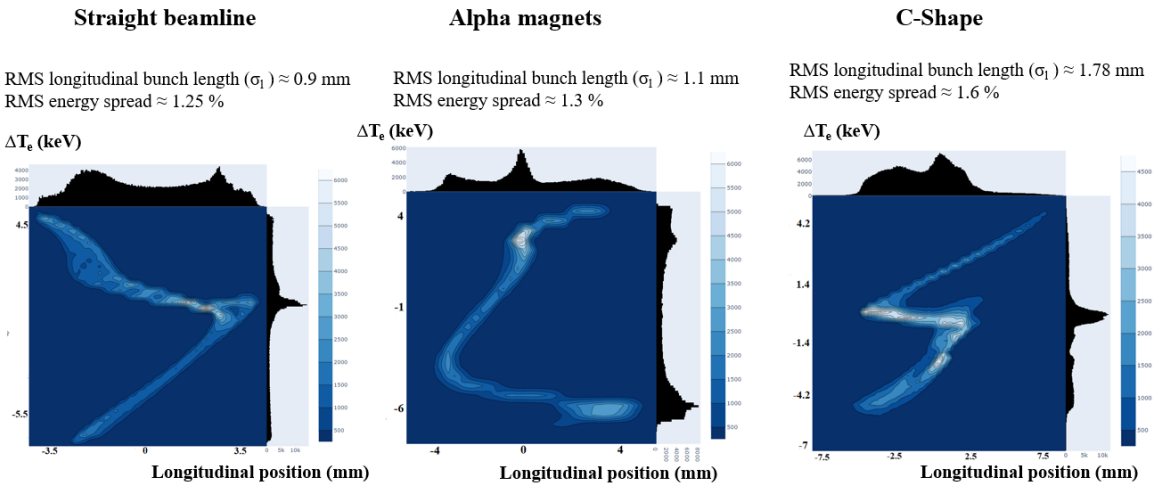

Figure 5.18: Longitudinal phase space for different transport systems with a bunch charge of 7.7 pC. (See Tab5.1)

As expected, the short straight beamline proves to be the most optimal structure for this type of beam. While a beamline with bending magnets results in slightly less effective beam compression, the difference is not as significant as one might have anticipated.

Based on the beam dynamics studies, we conclude that the simple dogleg injection remains the most reasonable choice, despite the small advantages observed in other options. The alpha-magnet solution does not allow for beam extraction from STEAM to

Table 5.1: Best longitudinal phase space parameters for the different scenarios.

Scenario	Bunch charge [pC]	$(\Delta E/E)_{\mathrm{rms}}$ [%]	Δs_{rms} [mm]	$\varepsilon_{\mathrm{long}}^{\mathrm{rms}}$ [keV·°]
dogleg	7.7	1.6	1.78	15.5
α-dogleg	7.7	1.3	1.1	7.79
straight	7.7	1.25	0.9	6.13
200 keV dogleg	39	1.0	3.45	29.25

the Mott polarimeter, while the straight beamline would require major installation work to operate both sources simultaneously.

5.8 Separation beamline for 200 keV

Moreover, as previously mentioned, with a minor upgrade, the electron source MIST could generate electron beams with energies up to 200 keV and significantly higher bunch currents. Implementing this upgrade would also require modifications to the MAMBO acceleration system and the bending magnets, but it remains a feasible future development.

To assess the maximum achievable beam current and its quality at the entrance to the first MAMBO acceleration section, a simulation was performed for a 200 keV beam. The transport channel geometry remained the same as that of the beamline with C-shaped magnets, with corresponding optimization of the magnetic element strengths. The results of the CST simulation for this configuration are shown in Figure 5.19.

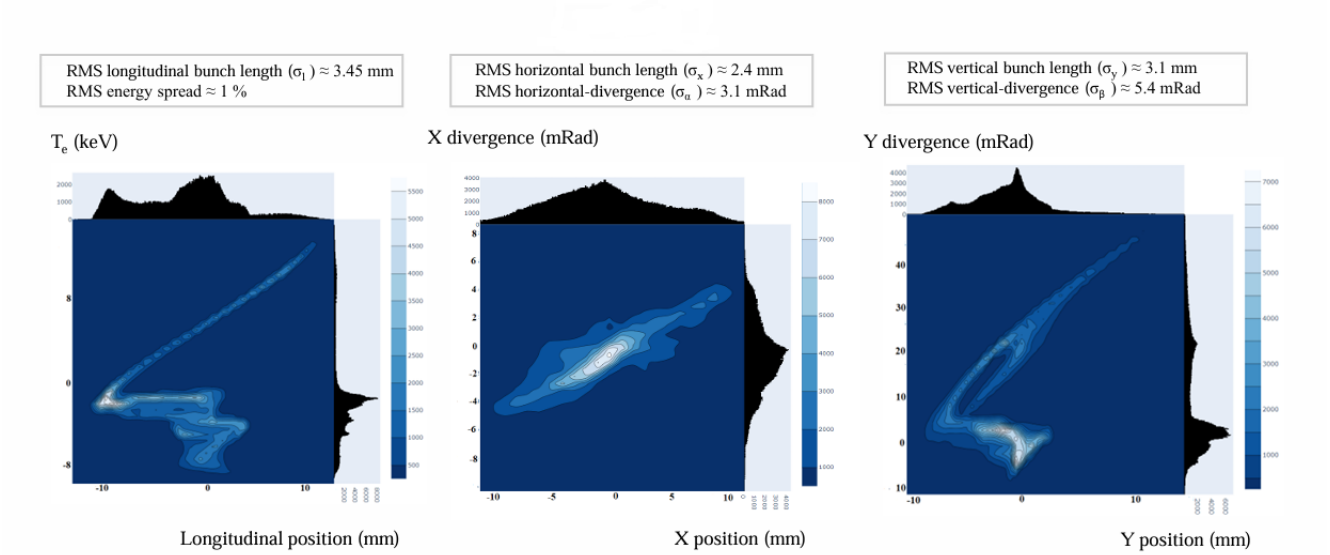

Figure 5.19: Phase space of a 39 pC, 200 keV electron beam at the entrance to the first acceleration section of MAMBO.

The simulation confirmed that, as expected, the maximum transportable bunch charge significantly increased, reaching at least 39 pC, which corresponds to a 50 mA beam current at 1.3 GHz. This improvement is primarily due to the higher beam energy, which substantially reduces the influence of space charge effects on beam dynamics.

Chapter 6

Experimental test of bending magnet

Since the designed separation beamline will be built only in a few years, it was decided to conduct a test of the bending magnet by building a temporary setup for this experiment. The idea of experiment is the following - the electron beam generated by the STEAM source was transported approximately 5 meters to the bending magnet test assembly. The dipole magnet was temporarily placed downstream of the quadrupole triplet $Q60$, the scheme of experiment is shown on fig. 6.1.

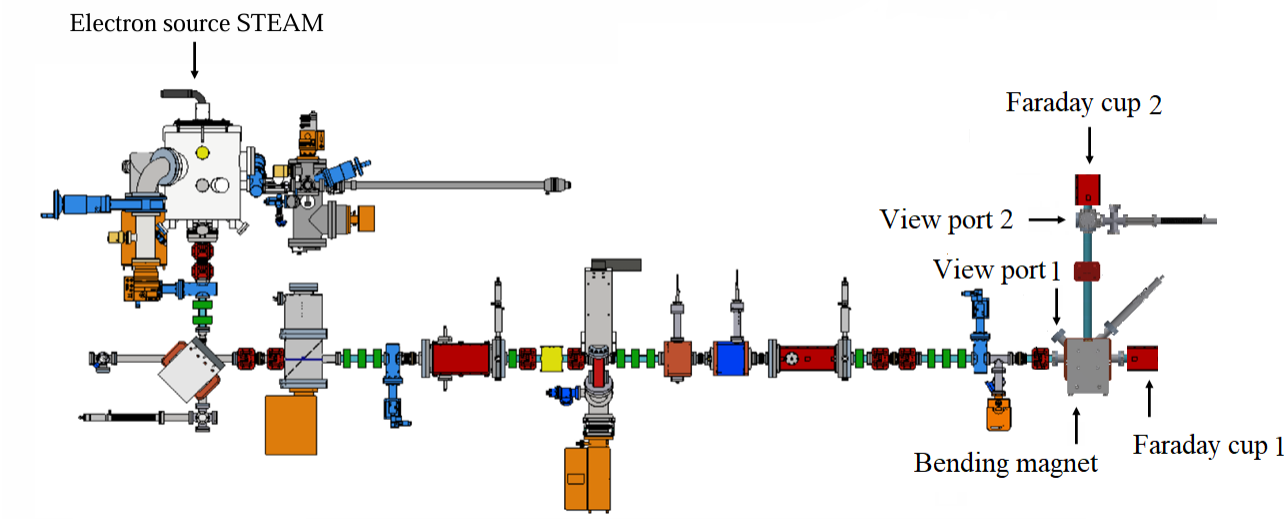

Figure 6.1: Temporary experimental setup used for testing of dipole magnet.

The experiment was conducted in four stages

1. In the first stage, the bending magnet was turned off, and the electron beam was focused onto a scintillation screen located inside the bending magnet. This allowed us to test the beam position diagnostic system and visually observe the beam using a video surveillance system on a scintillation screen via view port 1.

2. In the second stage, the scintillation screen was removed, and the beam was directed to the Faraday cup (Faraday cup 1) located at the end of the straight beamline, allowing the beam current to be measured.

3. In the third stage of the experiment, the bending magnet was turned on, and the beam was deflected by 90 degrees and transported to a second scintillation screen, which is located 51 centimeters from the main beamline (view port 2).

4. Once the beam position was confirmed using the scintillation screen, the screen was removed, and the beam was directed to the second Faraday cup (Faraday cup 2), where the current was also measured.

This approach made it possible to measure the beam current before and after the deflection and determine the beam transport efficiency.

The appearance of the experimental setup is shown in fig. 6.2.

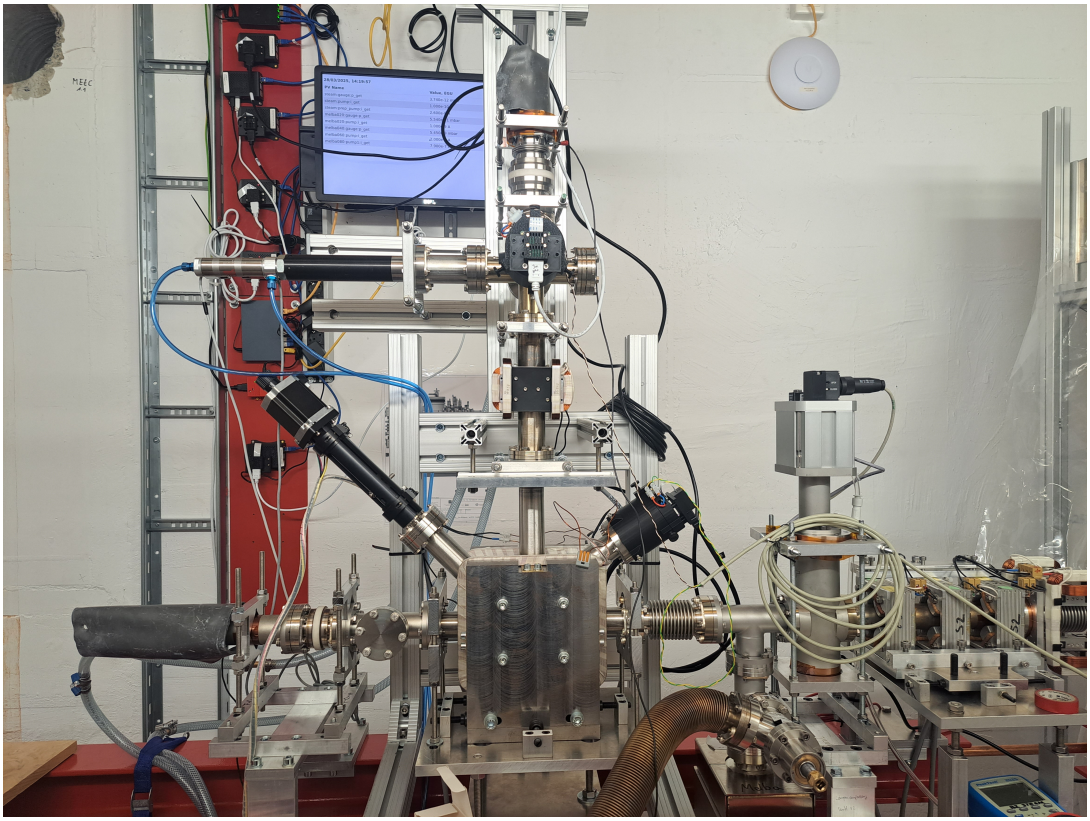

Figure 6.2: Temporary experimental setup used for testing of dipole magnet.

Fig. 6.3 shows the beam spot on the first scintillation screen (observed through view port 1) when the magnet is turned off, at the end of the straight section. The image includes a photograph taken with the lights on and another taken with the lights off. The electron beam is in the center. The round halo in the photograph is reflected light.

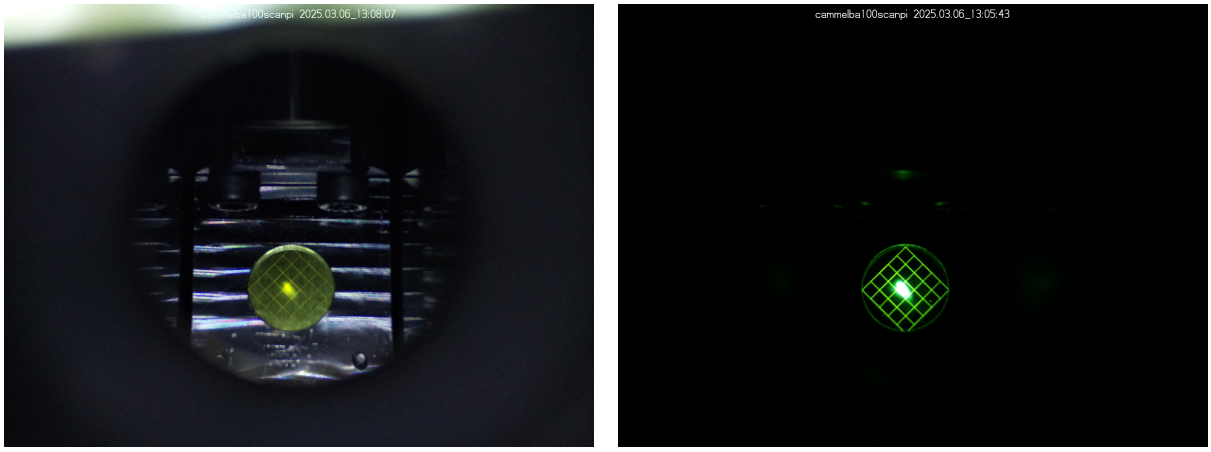

(a) Illumination on (b) Illumination off

Figure 6.3: Beam spot on the scintillator screen inside the bending magnet (view port 1), with illumination switched off (a) and on (b).

It should be noted that the size of one grid division on the scintillation monitor is 2 mm, and the center of the scintillation screen does not correspond to the design beam orbit due to alignment issues. The current measured in the Faraday cup (Faraday cup 1) was 4.19×10^{-9} A.

At the next stage, the bending magnet was switched on. During the experiment, the nominal operating current of the bending magnet magnet of $2.07A$ was used, which corresponds to a 90-degree beam deflection. A beam corrector was also installed downstream of the bending magnet to adjust the beam position on the scintillation screen (view port 2) after deflection.

Fig. 6.4 shows the beam spot after a 90-degree bend, with the light both on and off. A steerer was used to center the beam on the screen.

The electron beam is in the center. The round halo in the photograph is reflected light.

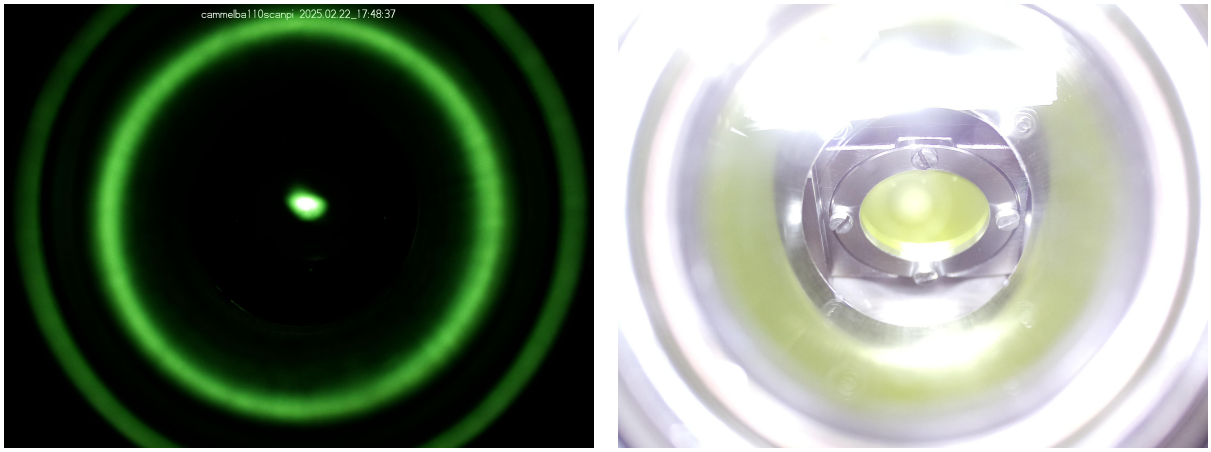

(a) Illumination off (b) Illumination on

Figure 6.4: Beam spot on the scintillator screen (view port 2) after a 90-degree bend, with illumination switched off (a) and on (b).

The experiment confirmed the proper functioning of the dipole magnet and demon-

strated successful beam transport after deflection. The observed beam spot on the scintillator indicates that beam quality was maintained during the 90-degree bend.

At the next step, the screen was removed with linear mover, and the beam was directed to the second Faraday cup (Faraday cup 2), where the current was also measured. The current measured in the Faraday cup (Faraday cup 2) was 4.09×10^{-9} A. This accounted for approximately 98% of the initial beam current before the bend. The discrepancy can be explained by the low current and, consequently, measurement uncertainties.

To check how the residual magnetization in the rotating magnet affects the beam position, the following experiment was conducted. The bending magnet was degaussed. Then, the beam was bent by 90 degrees without the dipole steerer, which had previously centered the beam on the scintillation monitor (view port 2) (see fig. 6.5).

After that, the bending magnet was turned off and then turned on again without performing the degaussing procedure. Fig. 6.5 shows the new beam position, allowing evaluation of the influence of the residual magnetization on the beam position. The beam displacement on the scintillation monitor was approximately 5 mm.

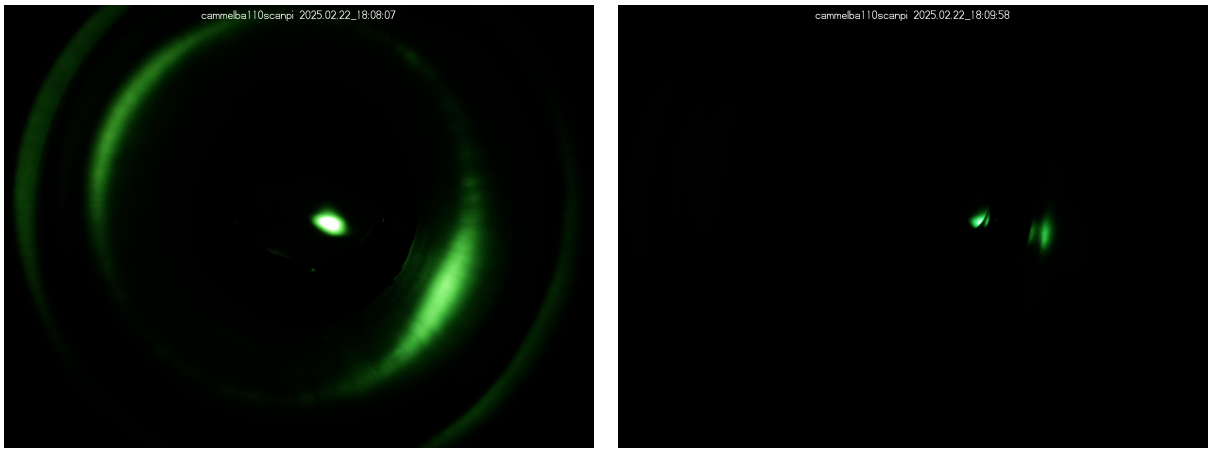

Figure 6.5: Beam spot on the scintillator screen (view port 2) after a 90-degree bend, with degaussing procedure (a) and without (b).

Additionally, the effectiveness of the degaussing procedure was tested. Several measurements of the beam position were performed with and without degaussing. The results showed that when degaussing was applied and the magnet was subsequently energized with the same current, the beam returned to its original position with high accuracy.

In contrast, omitting the degaussing procedure resulted in beam displacement due to remanence. The observed displacement was approximately 5 mm, consistent with a measured residual field of bending magnet.

As shown in Chapter 3, the average remanence in bending magnet is approximately 80 μT. Let us estimate the beam displacement on the scintillation monitor caused by such an additional field in the bending magnet.

For small changes in the magnetic field, we can assume that the angle of rotation θ is approximately proportional to the field strength B:

$$\theta \propto B\,.$$

Initial conditions:

$$\theta_{\text{old}} = 90^\circ, \quad B_{\text{old}} = 11.7\,\text{mT}, \quad \Delta B = 0.08\,\text{mT}\,,$$

Consequently, the change in angle is approximately:

$$\Delta\theta \approx 0.615^\circ \approx 5.4 \text{ mm}$$

Assuming the residual magnetization acts as an additional magnetic field, the calculated beam displacement matches the observed 5 mm, confirming the validity of the experimental observations.

Chapter 7

Conclusions

The main objective of this thesis was to design the additional injection beamline that will provide transport and compression of 100 keV electron bunches to the first accelerator section of MAMBO with a maximum bunch charge of up to 7.7 pC.

Moreover, this beamline allows transport of the electron beam from the electron source STEAM to the Double Scattering Mott Polarimeter.

The design process began with the development of a linear lattice of the transport channel, followed by beam dynamics simulations that accounted for space-charge effects using CST.

As part of this thesis, I have designed and manufactured special bending magnets, and their 3D magnetic field maps were measured. Additionally, vacuum chambers for the bending magnets were developed, featuring a scintillation monitors for additional beam position diagnostics within the separation beamline.

The sector magnet and its diagnostics have been tested already successfully at MESA.

Chapter 8

Outlook

After successful testing, the magnet will be shifted downstream to its final position, where it will be fully integrated into the beamline setup. This relocation marks a key step toward operational readiness and alignment with the overall experimental geometry.

The magnet support will be modified to make it movable, which will allow flexible positioning during various experimental phases. This adjustment is aimed at reducing unwanted magnetic field contributions during MESA/P2 operation to negligible levels.

Further optimization of the simulation is planned, for instance with respect to operating two bunchers simultaneously. This dual-buncher scheme is expected to improve the longitudinal emittance at the focal point.

In the future, such a "double beamline" configuration—with beams traveling in antiparallel directions through the same magnet—may be employed for an extremely accurate polarimeter, the Colliding beam Möller polarimeter [64].

Bibliography

[1] P. Heil *et al.*, *Phys. Rev. Accel. Beams* **24**, 042803 (2021). doi:10.1103/PhysRevAccelBeams.24.042803.

[2] R. Heine, et al. *IPAC 2012, New Orleans, USA, TUPPR073, (2012). http://accelconf.web.cern.ch/AccelConf/IPAC2012/papers/tuppr073.pdf.*

[3] S. Friederich *Development of a highly brilliant photoemission source for spin-polarized beams", Doctoral thesis, Johannes Gutenberg-Universität Mainz, 2019.*

[4] M. A. Dehn, K. Aulenbacher, P. S. Plattner *"MIST - The MESA-Injector Source Two", in Proc. IPAC'22, Bangkok, Thailand, Jun. 2022, pp. 2624-2626. doi:10.18429/JACoW-IPAC2022-THPOPT024.*

[5] F. Hug, K. Aulenbacher, R. Heine, B. Ledroit, D. Simon *"MESA - an ERL project for particle physics experiments", presented at the LINAC'16, East Lansing, MI, UAS, 2017, paper: MOP106012, this conference. DOI:10.18429/JACoW-LINAC2016-MOP106012.*

[6] H. Merkel, P. Achenbach, C. Ayerbe Gayoso, et al. *Search for light gauge bosons of the dark sector at MAMI, PACS numbers: 14.70.Pw, 25.30.Rw, 95.35.+d .*

[7] L. Mermiga et al. *"High-Current Energy-Recovering Linacs", Annu. Rev. Nuclear Particle Science (2003) 53:387–429, doi:10.1146/annurev.nucl.53.041002.110456 (2013).*

[8] Anatolii Kalamaiko, Kurt Aulenbacher, Monika Dehn, Simon Friederich *Status and extended beam dynamics scenarios for the second injection beam line at MESA, JACoW IPAC2023 (2023), WEPL040, DOI: 10.18429/JACoW-IPAC2023-WEPL040* .

[9] Anatolii Kalamaiko, Kurt Aulenbacher, Monika Dehn, Simon Friederich, Christian Stoll *High Bunch Charges in the Second Injection Beamline of MESA, JACoW IPAC2022 (2022) THPOPT007, DOI: 10.18429/JACoW-IPAC2022-THPOPT007* .

[10] H. Wiedemann: *Particle Accelerator Physics, Springer Verlag, 1993.*

[11] A. Adelmann, A. Gsell, C. Kraus, Y. Ineichen, S. Russell, Y. Bi, C. Wang, J. Yang, H. Zha, S. Sheehy, C. Rogers, and C. Mayes, *The OPAL Framework. Version 1.1.9 User's Reference Manual*, PSI Report, PSIPR-08-02, 2013.

[12] H5Part: High-Performance Parallel IO for Particle-Based Simulations. Available at: `http://h5part.web.psi.ch/`

[13] J.J. Yang, A. Adelmann, M. Humbel, M. Seidel, and T.J. Zhang, *Beam Dynamics in High Intensity Cyclotrons Including Neighboring Bunch Effects: Model, Implementation and Application*, Phys. Rev. ST Accel. Beams **13**, 064201, 2010.

[14] K. Wille, *The Physics of Particle Accelerators*, Oxford University Press, 2005.

[15] J. Rossbach and P. Schmüser, "Basic course on accelerator optics," in *CERN Accelerator School 94-01 Vol. 1*, CERN, 1994.

[16] H. Goldstein et al., *Klassische Mechanik*, vol. 1. Auflage, WILEY VCH, 2006.

[17] S. Schlimme, K. Aulenbacher, S. Baunack, N. Berger, A. Denig, L. Doria, A. Khoukaz, F. Maas, H. Merkel, C. Sfienti, and M. Thiel, The MESA physics program, *EPJ Web Conf.*, vol. 303, 06002, 2024. doi:10.1051/epjconf/202430306002, arXiv:2402.01027 [nucl-ex]

[18] K. Aulenbacher *et al.*, "The MESA accelerator project at Mainz University," *Journal of Physics: Conference Series*, vol. 507, no. 3, p. 032037, 2014.

[19] European Organization for Nuclear Research (CERN), *The Importance of Modern Particle Accelerators in Scientific Research*, Journal of Advanced Physics, vol. 15, no. 4, pp. 123–456, 2020.

[20] L. Doria, P. Achenbach, M. Christmann, A. Denig, H. Merkel, *Search for light dark matter with the MESA accelerator*, arXiv:1809.07168, 2018.

[21] MAGIX Collaboration, "MAGIX @ MESA," Institute for Nuclear Physics, Johannes Gutenberg University Mainz. `https://magix.uni-mainz.de/`

[22] PRISMA+ Cluster of Excellence, "MESA – Mainz Energy-Recovering Superconducting Accelerator," Johannes Gutenberg University Mainz. `https://www.prisma.uni-mainz.de/facilities/mesa-mainz-energy-recovering-superconducting-accelerator/`

[23] S. Grieser, D. Bonaventura, P. Brand, C. Hargens, B. Hetz, L. Leßmann, C. Westphälinger, and A. Khoukaz, "A Cryogenic Supersonic Jet Target for Electron Scattering Experiments at MAGIX@MESA and MAMI," arXiv:1806.05409 [physics.ins-det], 2018.

[24] D. Becker et al., *The P2 Experiment - A future high-precision measurement of the electroweak mixing angle at low momentum transfer*, Eur. Phys. J. A (2018) 54:208,

[25] F. Hinterberger, *Physik der Teilchenbeschleuniger und Ionenoptik, Springer, 2008*

[26] Dassault Systemes, *CST Studio Suite - 3D Electromagnetic Simulation Software*,

[27] S. A. Manego, Y. A. Bumai, and V. V. Cherny, "The Hall Effect," Educational and methodological manual for students of the specialties "Information and Measuring Equipment" and "Technical Safety Support," Belarusian National Technical University, Minsk, 2016. `https://rep.bntu.by/bitstream/handle/data/25969/EHffekt_Holla.pdf`

[28] G. F. Knoll, *Radiation Detection and Measurement*, 3rd ed., John Wiley and Sons, 2000.

[29] Kurt J. Lesker Company, *Multi-Pin Mil-Spec Feedthroughs (MS)*, Feedthroughs and Viewports section, Kurt J. Lesker Company. https://www.lesker.com/feedthroughs-viewports.cfm?section=multi-pin-mil-spec-feedthroughs-ms

[30] P. F. Baranov, S. V. Muravyov, V. E. Ogay, and S. V. Uchaikin, *Fluxgate Magnetometer for Measuring Magnetic Induction up to 1 nT*, Educational and methodological manual for students of the specialties "Information and Measuring Equipment" and "Technical Safety Support," Belarusian National Technical University, Minsk, 2016. https://rep.bntu.by/bitstream/handle/data/25969/EHffekt_Holla.pdf

[31] I. C. Alexander, *Experimental Investigation of the Beam Dynamics of the MESA Photoinjector*, PhD thesis, Johannes Gutenberg-Universität Mainz, 2018.

[32] F. F. Chen, *Introduction to Plasma Physics and Controlled Fusion*, Springer, 2nd edition, 1984.

[33] T. P. Wangler, *RF Linear Accelerators*, 2nd ed., Wiley-VCH, Weinheim, 2008.

[34] K. Floettmann, *Note on the thermal emittance of electrons emitted by Cesium Telluride photocathodes*, TESLA FEL-Report 1997-01, DESY, Hamburg, 1997.

[35] K. Aulenbacher, *Das MESA Projekt*, in Proceedings of the DPG-Frühjahrstagung (DPG Spring Meeting), Dresden, Germany, 2013.

[36] D. Alesini, *Power Coupling*, CERN Yellow Report CERN-2011-007, Contribution to the CAS-CERN Accelerator School, Specialised Course on RF for Accelerators, 8–17 June 2010, Ebeltoft, Denmark, pp. 155–183.

[37] Dassault Systèmes, *CST Studio Suite – Official Documentation*, https://www.3ds.com/products-services/simulia/products/cst-studio-suite/documentation/, accessed August 13, 2025.

[38] Dassault Systèmes, *Electromagnetic Simulation Solvers*, https://www.3ds.com/products/simulia/cst-studio-suite/electromagnetic-simulation-solvers, accessed August 13, 2025.

[39] C. K. Birdsall, Particle-in-Cell Charged-Particle Simulations, Plus Monte Carlo Collisions With Neutral Atoms (PIC-MCC), *IEEE Transactions on Plasma Science*, vol. 19, no. 2, pp. 65–85, April 1991.

[40] A. Adelmann, P. Calvo, M. Frey, A. Gsell, U. Locans, C. Metzger-Kraus, N. Neveu, C. Rogers, S. Russell, S. Sheehy, et al., *OPAL: A Versatile Tool for Charged Particle Accelerator Simulations*, arXiv preprint arXiv:1905.06654, 2019.

[41] R. Hajima, *Energy Recovery Linacs for Light Sources*, Review of Accelerator Science and Technology, vol. 3, pp. 121–146, 2010. doi:10.1142/S1793626810000324

[42] M. Tigner, A possible apparatus for electron clashing-beam experiments, *Il Nuovo Cimento*, vol. 37, pp. 1228–1231, 1965. doi:10.1007/BF02750006

[43] K. G. Steffen, *High Energy Beam Optics*, Wiley, New York, 1965, p. 117.

[44] CERN Accelerator Beam Physics Group, *MAD-X: Methodical Accelerator Design*, CERN, Geneva, Switzerland. Available at: `http://mad.web.cern.ch/mad/`, accessed August 13, 2025.

[45] D. Simon, K. Aulenbacher, R. Heine, and F. Schlander, Lattice and Beam Dynamics of the Energy Recovery Mode of the Mainz Energy-Recovering Superconducting Accelerator MESA, *Proceedings of the 6th International Particle Accelerator Conference (IPAC'15)*, Richmond, VA, USA, 3–8 May 2015, pp. 220–222. doi:10.18429/JACoW-IPAC2015-MOPWA025

[46] P. Heil, *Kohärente Smith-Purcell-Strahlung zur minimal invasiven Bunchlängenmessung im Subpikosekundenbereich*, Ph.D. thesis, Johannes Gutenberg-Universität Mainz, 2020.

[47] P. Agostini *et al.*, The Large Hadron–Electron Collider at the HL-LHC, *Journal of Physics G: Nuclear and Particle Physics*, vol. 48, no. 11, 110501, 2021. doi:10.1088/1361-6471/ac0d4d

[48] A. Gellrich, K. Jost, and J. Kessler, Elimination of instrumental asymmetries in electron polarization analysis, *Review of Scientific Instruments*, vol. 61, no. 11, pp. 3399–3401, 1990. doi:10.1063/1.1141872

[49] M. Molitor and K. Aulenbacher, "A Double-Scattering Polarimeter for the P2 Experiment at MESA," in *Proceedings of the XVIth International Workshop on Polarized Sources, Targets, and Polarimetry (PSTP 2015)*, doi:10.22323/1.324.0029

[50] G. H. Hoffstaetter et al., *CBETA Design Report, Cornell-BNL ERL Test Accelerator*, Cornell University and Brookhaven National Laboratory, 2017. Available at: `https://arxiv.org/abs/1706.04245`.

[51] R. Heine, Preaccelerator concepts for an energy-recovering superconducting accelerator, *Phys. Rev. Accel. Beams*, vol. 24, no. 1, 011602, 2021. doi:10.1103/PhysRevAccelBeams.24.011602

[52] M. Arnold, C. Burandt, C. Eschelbach, R. Grewe, F. Hug, L. Jürgensen, N. Pietralla, F. Schließmann, M. Steinhorst,
First operation of the superconducting Darmstadt linear electron accelerator as an energy recovery linac,
Phys. Rev. Accel. Beams **23**, 020101 (2020).
DOI: `https://doi.org/10.1103/PhysRevAccelBeams.23.020101`

[53] C. P. Stoll, *Beam Dynamical Behaviour of the MESA SRF Structures under Recirculating Operation*, Ph.D. thesis, Johannes Gutenberg-Universität Mainz, Mainz, Germany, 2020.

[54] V. Bechthold, *Untersuchung von Multi-Alkali-Verbindungen im Hinblick auf ihre Eignung zur Erzeugung hochbrillanter Elektronenpulse*, Ph.D. thesis, Johannes Gutenberg-Universität Mainz, Mainz, Germany, 2018.

[55] H. Merkel *et al.*, Search for light massive gauge bosons as an explanation of the $(g-2)_\mu$ anomaly at MAMI, arXiv:1404.5502 [hep-ex], 2014. Available at: `https://arxiv.org/abs/1404.5502`.

[56] B. Ledroit, *Target Induced Halo Formation and Collimation Following MAGIX at MESA*, Ph.D. thesis, Johannes Gutenberg-Universität Mainz, 2021.

[57] MAGIX Collaboration, *MAGIX Project at MESA*, Available at: `https://magix.uni-mainz.de/magix.php`, accessed August 13, 2025.

[58] H. A. Enge, Deflecting magnets with curved pole faces, *Review of Scientific Instruments*, vol. 34, no. 4, pp. 385–389, 1963. doi:10.1063/1.1718473

[59] I. V. Bazarov, B. M. Dunham, Y. Li, X. Xie, and C. K. Sinclair, Thermal emittance and response time of a cesium potassium antimonide photocathode, *Journal of Applied Physics*, vol. 103, no. 5, 054901, 2008. doi:10.1063/1.2884330

[60] N. Scahill and K. Aulenbacher, Pulse response of the GaAs/GaAsP superlattice photocathode, *Journal of Applied Physics*, vol. 132, no. 18, 185702 (2022). doi:10.1063/5.0108675

[61] M. Dehn, K. Aulenbacher, V. Bechthold, and F. Fichtner, Reducing the contribution of the photoemission process to the unwanted beam in photoelectron sources at accelerators, *Applied Physics Letters*, vol. 111, no. 13, 132105, 2017. doi:10.1063/1.4993934

[62] R. Thapa, *RF Synchronised Semiconductor Laser System for MESA*, Master's thesis, Johannes Gutenberg University Mainz, Mainz, Germany, 2021.

[63] K.-H. Steffens, *Konzeption und Optimierung eines 100 keV Injektionssystems zur Erzeugung eines longitudinal polarisierten Elektronenstrahles an MAMI*, Ph.D. thesis, Johannes Gutenberg-Universität Mainz, Mainz, Germany, 1993.

[64] K. Aulenbacher, The Colliding Beam Møller Polarimeter, in *Proceedings of the 2024 International Workshop on Polarized Sources, Targets, and Polarimetry (PSTP 2024)*, to be published.

[65] V. I. Shvedunov, M. O. Ihm, H. Euteneuer, K.-H. Kaiser, and Th. Weis, Design of a Prebuncher for Increased Longitudinal Capture Efficiency of MAMI, in *Proceedings of the 7th European Particle Accelerator Conference (EPAC 1996)*, Sitges, Spain, 10–14 June 1996, pp. 1001–1003.

[66] R. Pohl, R. Gilman, G. A. Miller, and K. Pachucki, "Muonic hydrogen and the proton radius puzzle," *Ann. Rev. Nucl. Part. Sci.* 63 (2013), 175–204, doi:10.1146/annurev-nucl-102212-170627, arXiv:1301.0905 [physics.atom-ph].

[67] D. Simon, "Images provided via personal communication," KPH, 2020. Unpublished.

Acknowledgements

Statement

I hereby confirm that the presented work was completed by me independently, without the unauthorized assistance of third parties. In the preparation of this work, artificial intelligence-based tools (ChatGPT by OpenAI, Google Translate) were used to a limited extent, solely for the purpose of improving grammar, style, and clarity of presentation. All suggestions received with their help were critically assessed, revised, and integrated into the text in accordance with the requirements of scientific integrity. The content, structure, and scientific arguments are the result of my own intellectual work.

Anatolii Kalamaiko
04.09.2025

Associated Publications

[**Kalamaiko & Aulenbacher 2022**]
Kalamaiko, A. A., Aulenbacher, K., Dehn, M. A., Friederich, S., and Stoll, C. P.
High Bunch Charges in the Second Injection Beamline of MESA.
in Proc. IPAC'22: 13th International Particle Accelerator Conference
(Bangkok, Thailand, June 2022), pp. 2574–2576. JACoW Publishing, Geneva, Switzerland.
doi:10.18429/JACoW-IPAC2022-THPOPT007

[**Kalamaiko & Aulenbacher 2023**]
Kalamaiko, A., Aulenbacher, K., Dehn, M., and Friederich, S.
Status and Extended Beam Dynamics Scenarios for the Second Injection Beam Line at MESA.
in Proc. IPAC'23: 14th International Particle Accelerator Conference
(Venice, Italy, May 2023), pp. 3212–3214. JACoW Publishing, Geneva, Switzerland.
doi:10.18429/JACoW-IPAC2023-WEPL040

8.1 Appendix 1

8.2 Appendix 2

8.3 Appendix 3

Table 8.1: Quadrupole Parameters

Beamline configuration	Bunch charge	Q1	Q2	Q3	Q4	Q5	Q6	Q7
Straight beamline	100 fC	X	X	–	–	–	–	–
	1 pC	X	X	–	–	–	–	–
	7 pC	X	X	–	–	–	–	–
Alpha-magnet	100 fC	X	X	X	X	X	–	–
	1 pC	X	X	X	X	X	–	–
	7 pC	X	X	X	X	X	–	–
Dogleg	100 fC	X	X	X	X	X	X	X
	1 pC	X	X	X	X	X	X	X
	7 pC	X	X	X	X	X	X	X

8.4 CV Anatolii Kalamaiko